

Mathematical Problems in Engineering

Theory, Methods, and Applications

Special Issue

Drying Modeling and Simulation

Guest Editors: Zhijun Zhang, Ireneusz Zbicinski, Lixin Huang,
Tsutomu Nozaki, and Zhonghua Wu



Drying Modeling and Simulation

Mathematical Problems in Engineering

Drying Modeling and Simulation

Guest Editors: Zhijun Zhang, Ireneusz Zbicinski,
Lixin Huang, Tsutomu Nozaki, and Zhonghua Wu



Copyright © 2012 Hindawi Publishing Corporation. All rights reserved.

This is a special issue published in "Mathematical Problems in Engineering." All articles are open access articles distributed under the Creative Commons Attribution License, which permits unrestricted use, distribution, and reproduction in any medium, provided the original work is properly cited.

Editorial Board

- E. M. Abdel-Rahman, Canada
R. K. Abu Al-Rub, USA
Salvatore Alfonzetti, Italy
Igor Andrianov, Germany
Sebastian Anita, Romania
W. Assawinchaichote, Thailand
Erwei Bai, USA
Ezzat G. Bakhoum, USA
Jos Manoel Balthazar, Brazil
Rasajit K. Bera, India
Jonathan N. Blakely, USA
Stefano Boccaletti, Spain
Daniela Boso, Italy
M. Boutayeb, France
Michael J. Brennan, UK
John Burns, USA
Salvatore Caddemi, Italy
Piermarco Cannarsa, Italy
Jose E. Capilla, Spain
Carlo Cattani, Italy
M. M. Cavalcanti, Brazil
Diego J. Celentano, Chile
Mohammed Chadli, France
Arindam Chakraborty, USA
Yong-Kui Chang, China
Michael J. Chappell, UK
Kue-Hong Chen, Taiwan
Kui Fu Chen, China
Xinkai Chen, Japan
Jyh Horng Chou, Taiwan
Slim Choura, Tunisia
Cesar Cruz-Hernandez, Mexico
Swagatam Das, India
Filippo de Monte, Italy
M. do R. de Pinho, Portugal
Antonio Desimone, Italy
Yannis Dimakopoulos, Greece
Baocang Ding, China
Joao B. R. Do Val, Brazil
Daoyi Dong, Australia
Balram Dubey, India
Horst Ecker, Austria
M. Onder Efe, Turkey
Elmetwally Elabbasy, Egypt
Alex Elias-Zuniga, Mexico
Anders Eriksson, Sweden
Vedat S. Erturk, Turkey
Qi Fan, USA
Moez Feki, Tunisia
Ricardo Femat, Mexico
Rolf Findeisen, Germany
Robertt A. F. Valente, Portugal
C. R. Fuerte-Esquivel, Mexico
Zoran Gajic, USA
Ugo Galvanetto, Italy
Furong Gao, Hong Kong
Xin-Lin Gao, USA
Behrouz Gatmiri, Iran
Oleg V. Gendelman, Israel
Didier Georges, France
Paulo Batista Goncalves, Brazil
Oded Gottlieb, Israel
Quang Phuc Ha, Australia
Muhammad R. Hajj, USA
Thomas Hanne, Switzerland
Katica R. Hedrih, Serbia
M.I. Herreros, Spain
Wei-Chiang Hong, Taiwan
J. Horacek, Czech Republic
Chuangxia Huang, China
Gordon Huang, Canada
Yi Feng Hung, Taiwan
Hai-Feng Huo, China
Asier Ibeas, Spain
Anuar Ishak, Malaysia
Reza Jazar, Australia
Zhijian Ji, China
J. Jiang, China
J. J. Judice, Portugal
Tadeusz Kaczorek, Poland
Tamas Kalmar-Nagy, USA
Tomasz Kapitaniak, Poland
Hamid Reza Karimi, Norway
Metin O. Kaya, Turkey
Nikolaos Kazantzis, USA
Farzad Khani, Iran
Kristian Krabbenhoft, Australia
Jurgen Kurths, Germany
Claude Lamarque, France
F. Lamnabhi-Lagarrigue, France
Marek Lefik, Poland
Stefano Lenci, Italy
Roman Lewandowski, Poland
Shanling Li, Canada
Jian Li, China
Ming Li, China
Tao Li, China
Shihua Li, China
Teh-Lu Liao, Taiwan
P. Liatsis, UK
Shueei M. Lin, Taiwan
Jui-Sheng Lin, Taiwan
Bin Liu, Australia
Wanquan Liu, Australia
Yuji Liu, China
Fernando Lobo Pereira, Portugal
Paolo Lonetti, Italy
Vassilios C. Loukopoulos, Greece
Junguo Lu, China
Chien-Yu Lu, Taiwan
Alexei Mailybaev, Brazil
Manoranjan Maiti, India
Oluwole D. Makinde, South Africa
Rafael Martinez-Guerra, Mexico
Driss Mehdi, France
Roderick Melnik, Canada
Xinzhu Meng, China
Yuri V. Mikhlin, Ukraine
Gradimir Milovanovic, Serbia
Ebrahim Momoniat, South Africa
Trung Nguyen Thoi, Vietnam
Hung Nguyen-Xuan, Vietnam
Ben T. Nohara, Japan
Anthony Nouy, France
Sotiris K Ntouyas, Greece
Gerard Olivar, Colombia

Claudio Padra, Argentina
Francesco Pellicano, Italy
Vu Ngoc Phat, Vietnam
A. Pogromsky, The Netherlands
Seppo Pohjolainen, Finland
Stanislav Potapenko, Canada
Sergio Preidikman, USA
Carsten Proppe, Germany
Hector Puebla, Mexico
Justo Puerto, Spain
Dane Quinn, USA
Rubén R. García, Spain
K. R. Rajagopal, USA
Gianluca Ranzi, Australia
Sivaguru Ravindran, USA
G. Rega, Italy
Pedro Ribeiro, Portugal
J. Rodellar, Spain
R. Rodriguez-Lopez, Spain
A. J. Rodriguez-Luis, Spain
Ignacio Romero, Spain
Hamid Ronagh, Australia
Carla Roque, Portugal
Manouchehr Salehi, Iran
Miguel A. F. Sanjuán, Spain
Ilmar Ferreira Santos, Denmark
Nickolas S. Sapidis, Greece
Bozidar Sarler, Slovenia
Andrey V. Savkin, Australia
Massimo Scalia, Italy
Mohamed A. Seddeek, Egypt
Alexander P. Seyranian, Russia
Leonid Shaikhet, Ukraine
Cheng Shao, China
Daichao Sheng, Australia
Tony Sheu, Taiwan
Zhan Shu, UK
Jian-Jun Shu, Singapore
Dan Simon, USA
Luciano Simoni, Italy
Grigori M. Sisoev, UK
Christos H. Skiadas, Greece
Davide Spinello, Canada
Sri Sridharan, USA
Rolf Stenberg, Finland
Xi-Ming Sun, China
Jitao Sun, China
Changyin Sun, China
Andrzej Swierniak, Poland
Allen Tannenbaum, USA
Cristian Toma, Romania
Irina N. Trendafilova, UK
Alberto Trevisani, Italy
Jung-Fa Tsai, Taiwan
Kuppalapalle Vajravelu, USA
Victoria Vampa, Argentina
Josep Vehi, Spain
Stefano Vidoli, Italy
Cheng C. Wang, Taiwan
Youqing Wang, China
Yijing Wang, China
Xiaojun Wang, China
Dan Wang, China
Moran Wang, USA
Yongqi Wang, Germany
Gerhard-Wilhelm Weber, Turkey
Jeroen A.S. Witteveen, USA
Kwok-Wo Wong, Hong Kong
Ligang Wu, China
Zheng-Guang Wu, China
Wang Xing-yuan, China
X. Frank XU, USA
Xuping Xu, USA
Jun-Juh Yan, Taiwan
Xing-Gang Yan, UK
Suh-Yuh Yang, Taiwan
Mahmoud T. Yassen, Egypt
Mohammad I. Younis, USA
Huang Yuan, Germany
S.P. Yung, Hong Kong
Ion Zaballa, Spain
Arturo Zavala-Rio, Mexico
Ashraf M. Zenkour, Saudi Arabia
Yingwei Zhang, USA
Xu Zhang, China
Liancun Zheng, China
Jian Guo Zhou, UK
Zexuan Zhu, China
Mustapha Zidi, France

Contents

Drying Modeling and Simulation, Zhijun Zhang, Ireneusz Zbicinski, Lixin Huang, Tsutomu Nozaki, and Zhonghua Wu
Volume 2012, Article ID 398130, 3 pages

Model Predictive Control of the Grain Drying Process, Feng Han, Chuncheng Zuo, Wenfu Wu, Junxing Li, and Zhe Liu
Volume 2012, Article ID 584376, 12 pages

Model of Mass and Heat Transfer during Vacuum Freeze-Drying for Cornea, Zou Huifen, Ye Sheng, Wang Dexi, Li Huixing, Cao Xiaozhen, and Yan Lijun
Volume 2012, Article ID 941609, 16 pages

Nonequilibrium Thermal Dynamic Modeling of Porous Medium Vacuum Drying Process, Zhijun Zhang and Ninghua Kong
Volume 2012, Article ID 347598, 22 pages

Distribution of Vapor Pressure in the Vacuum Freeze-Drying Equipment, Shiwei Zhang and Jun Liu
Volume 2012, Article ID 921254, 10 pages

SDSim: A Novel Simulator for Solar Drying Processes, Yolanda Bolea, Antoni Grau, and Alexandre Miranda
Volume 2012, Article ID 976452, 25 pages

Municipal Sewage Sludge Drying Treatment by an Composite Modifier, Na Wei
Volume 2012, Article ID 979764, 10 pages

Thin-Layer Drying Characteristics and Modeling of Chinese Jujubes, Xiao-Kang Yi, Wen-Fu Wu, Ya-Qiu Zhang, Jun-Xing Li, and Hua-Ping Luo
Volume 2012, Article ID 386214, 18 pages

Simulation for Sludge Flocculation I: Brownian Dynamic Simulation for Perikinetic Flocculation of Charged Particle, Linshuang Liu, Guolu Yang, and Minghui Yu
Volume 2012, Article ID 527384, 17 pages

Experimental Study on Forecasting Mathematical Model of Drying Shrinkage of Recycled Aggregate Concrete, Yuanchen Guo and Xue Wang
Volume 2012, Article ID 567812, 14 pages

Editorial

Drying Modeling and Simulation

**Zhijun Zhang,¹ Ireneusz Zbicinski,² Lixin Huang,³
Tsutomu Nozaki,⁴ and Zhonghua Wu⁵**

¹ School of Mechanical Engineering and Automation, Northeastern University, Shenyang 110004, China

² Faculty of Process and Environmental Engineering, Technical University of Lodz, 90-924 Lodz, Poland

³ Institute of Chemical Industry of Forest Products, Chinese Academy of Forestry, No. 16 Suojin 5th Village, Nanjin 210042, China

⁴ Department of Environment Engineering, Kagoshima University, Korimoto 1-21-24, Kagoshima 890-8580, Japan

⁵ Institute of Drying and Dewatering, College of Mechanical Engineering, Tianjin University of Science and Technology, 1038 Dagan Road, Hexi District, Tianjin 300222, China

Correspondence should be addressed to Zhijun Zhang, zhjzhang@mail.neu.edu.cn

Received 19 June 2012; Accepted 19 June 2012

Copyright © 2012 Zhijun Zhang et al. This is an open access article distributed under the Creative Commons Attribution License, which permits unrestricted use, distribution, and reproduction in any medium, provided the original work is properly cited.

The idea behind this special issue of *Mathematical Problems in Engineering* is to consider the study and applications of modeling and simulation in drying technology. Drying science has a long history and is not only related to the food processing industry but also to a broad range of sectors such as chemistry, biochemistry, pharmaceuticals, and agriculture. The drying of various materials at different conditions in a wide variety of industrial and technological applications is a necessary step to obtain products that serve people's daily needs, to facilitate and enhance certain chemical reactions in engineering processes, or to make these processes environmentally safe.

As drying processes consume large amounts of energy, any improvement in the existing dryer design and any reduction in cost will be beneficial to the industry. Drying is inherently a cross-disciplinary and multidisciplinary process because it requires the optimal fusion of transport phenomena and materials science to supply heat, remove moisture from the material, and to generate a dehydrated product of specific quality.

The modeling and simulation of the drying process is a significant topic. This special issue contains nine papers, the contents of which are summarized as follows.

"Municipal sewage sludge drying treatment by a composite modifier" by N. Wei. Drying experiments of municipal sewage sludge were carried out to decrease the moisture content of sewage sludge. The effect of SCM components on sludge moisture content was analyzed using uniform design, and the optimum composition of SCM was determined through computer-aided modeling and optimization.

“Thin-layer drying characteristics and modeling of Chinese jujubes” by X. Yi et al. A mathematical modeling of the thin-layer drying of jujubes in a convective dryer was established under controlled temperature and velocity conditions. The data from the experimental drying of jujubes were used to fit ten different thin-layer models. Then, the drying rate constants and the coefficients of the models tested were determined via nonlinear regression analysis using a statistical computer program.

“Simulation for sludge flocculation I: Brownian dynamic simulation for Perikinetic flocculation of charged particles” by L. Liu et al. To investigate the sludge drying process, a numerical simulation based on Brownian dynamic for the floc with uncharged and charged particles was conducted. The Langevin equation was used as a dynamical equation for tracking each particle in a floc. An initial condition and periodic boundary condition that conformed well to reality was used in calculating the floc growth process.

“Experimental study on forecasting mathematical model of drying shrinkage of recycled aggregate concrete” by Y. Guo and X. Wang. Based on the basic law in the AASHTO2007 model, the forecasting mathematical model for the drying shrinkage of recycled aggregate concrete was established through regression analysis and experimental study.

“SDSim: a novel simulator for solar drying processes” by Y. Bolea et al. SDSim is a novel solar dryer simulator based on a multicrop, inclined multipass solar air heater with in-built thermal storage mathematical model. SDSim has been developed as a design and development tool used to study and forecast the behavior of the system model to improve its drying efficiency and achieve a return on investment.

“Model of mass and heat transfer during vacuum freeze-drying for cornea” by H. Zou et al. A theoretical analysis of corneal freeze-drying was presented, and a mathematical model for describing heat and mass transfer during corneal vacuum freeze-drying was established. The analogy computation for the freeze drying of cornea was done using finite-element computational software.

“Distribution of vapor pressure in the vacuum freeze drying equipment” by S. Zhang and J. Liu. A mathematical model was developed to describe the vapor flow in the passageways either between material plates or in the channel between plate groups. The distribution of vapor pressure along the flow passageway was described. Two characteristic factors of passageways were defined to express the effects of structural and process parameters on vapor pressure distribution.

“Nonequilibrium thermal dynamic modeling of porous medium vacuum drying process” by Z. Zhang and N. Kong. Based on the theory of heat and mass transfer, a coupled model for vacuum drying of a porous medium was constructed. The model was implemented and solved with COMSOL software. The water evaporation rate was determined via the nonequilibrium method using the rate constant parameter.

“Model predictive control of the gain drying process” by F. Han et al. Using mathematical models and the quality model of the corn drying process, a digital simulation of the corn drying machine system based on a virtual instrument was established for the 5HSZ dryer. The device could automatically control the air temperature and predict the discharge speed of grain.

Acknowledgments

The authors are grateful to the authors of the special issue for their contributions. They thank the reviewers for their valuable comments on the submissions. They highly appreciate

the support from the editorial members of *Mathematical Problems in Engineering*, as well as the editorial staff of Hindawi Publishing Corporation. Dr. Zhang acknowledges the support from the National Natural Science Foundation of China (Grant nos. 31000665 and 51176027).

Zhijun Zhang
Ireneusz Zbicinski
Lixin Huang
Tsutomu Nozaki
Zhonghua Wu

Research Article

Model Predictive Control of the Grain Drying Process

**Feng Han,¹ Chuncheng Zuo,¹ Wenfu Wu,²
Junxing Li,³ and Zhe Liu⁴**

¹ College of Mechanical Science and Engineering, Jilin University, Changchun 130022, China

² College of Biological & Agricultural Engineering, Jilin University, Changchun 130022, China

³ Institute of Grain Machinery Research, Jilin Academy of Agricultural Machinery,
Changchun 130022, China

⁴ The College of Engineering and Technology, Jilin Agricultural University, Changchun 130118, China

Correspondence should be addressed to Chuncheng Zuo, lshxhf@126.com
and Wenfu Wu, wwfzlb@163.com

Received 15 March 2012; Revised 10 June 2012; Accepted 10 June 2012

Academic Editor: Zhonghua Wu

Copyright © 2012 Feng Han et al. This is an open access article distributed under the Creative Commons Attribution License, which permits unrestricted use, distribution, and reproduction in any medium, provided the original work is properly cited.

Drying plays an important role in the postharvesting process of grain. To ensure the quality of the dried grain and improve the intelligent level in drying process, a digital simulation of corn drying machine system based on a virtual instrument was established for 5HSZ dryer, automatically control the air temperature, and predict the discharging speed of grain and so forth. Finally, an online measurement and automated control software of grain parameters were developed to provide the changes of moisture, temperature, humidity, and germination rate in the process of drying. The study carried out in the actual processing showed that it can meet the requirements of the actual drying operation, effectively control the stability of the grain moisture, and keep the dry food quality.

1. Introduction

The final purpose of grain drying is to keep grains quality and to make them reach safe moisture content so that they can storage safely and process further. In the drying process, grain moisture content and grain quality are related to the selection of parameters such as initial moisture content, hot air temperature and grain discharge rate. In grain storage of China, especially some small grain storage, grain drying still adopts manual control method; that is, the grain moisture is obtained through the oven-drying method, and then depends on the measurement values to adjust the speed of the discharge grain manually. The control

process has long-time delay and poor stability, so the quality of the grain cannot be ensured. The research of the mathematical model of drying process has become an important means of studying grain drying process control at home and abroad [1–3]. In this paper, a simulation and control system, using LabVIEW, a graphical programming language, was built for a small modular crossflow dryer to predict the parameter changes in drying process and to control the parameters. The system adjusts control parameters by predicted results. Its objective is to achieve automatic control during the drying process, ensure the accuracy and uniformity of the grain moisture content, improve the relative germination rate after drying, and improve the poor stability of corn moisture and low quality during the manual control process in grain storage.

2. Drying Processing Technology

Drying experiment was carried out on two small 5HSZ-30-type crossflow grains dryers, which is the base of the predictive model. Figure 1 is 5HSZ-30-type dryer process flow diagram. It is very important to establish an accurate mathematical model for predicting the grain germination rate and moisture content in the grain-drying process.

The structure of drying section composed of eight mountain-shaped mesh plates, which is shown in Figure 2. Corn can flow top-down between the mesh plates. Hot air passes through the grain layer vertically and takes the water away.

The controller of the dryer includes the temperature sensor ($T_1 \sim T_4$), online grain moisture content sensor ($M_0 \sim M_4$), the data acquisition system, and a industrial control computer, the sensors location shown in Figure 1. The drying system uses distributed control system which is made up of the control unit (computer), temperature measurement and control instruments, moisture measuring instruments, control actuators, and other components. Data exchanges between control unit and the temperature measurement and control instruments (T_{01}, T_{02}), moisture measuring instruments and control actuators ($C_1 \sim C_4$) to achieve via RS485 data bus. The control unit can obtain the data from the temperature measurement and control instruments and moisture measuring instruments and send the data to the PLC. The achievement is using real-time measured data from sensors to provide a large number of measured data for the simulation system, and adjusting the prediction for the further production process.

3. Drying Simulation System

3.1. Drying Mathematical Model

In the paper, in the partial differential equation model which is designed by Professor Bakker-Arkema as the drying process model, this model can be used in crossflow, downstream, and upstream dryer simulation. According to the characteristics of corn, the equation of drying rate adopts Li Huizhen equations [4, 5]. Model is as follows:

(1) the equation of drying rate

$$\frac{M - M_e}{M_0 - M_e} = \exp(-kt^N), \quad (3.1)$$

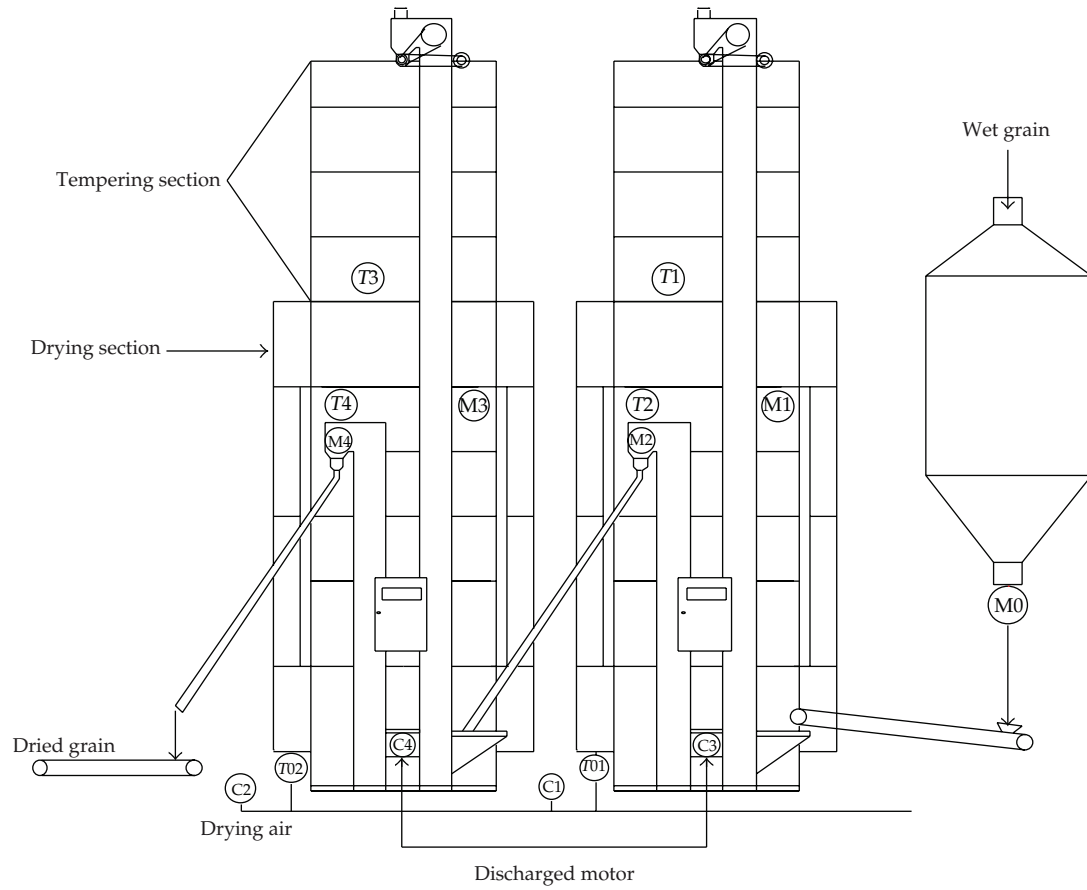


Figure 1: 5HSZ-30-type dryer.

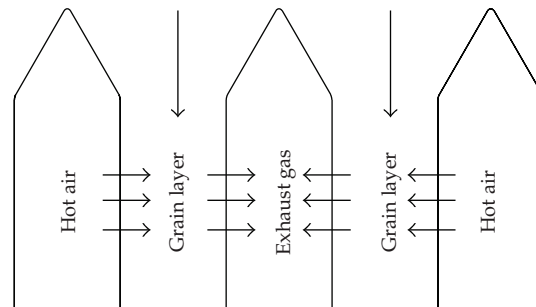


Figure 2: Schematic diagram of drying section.

(2) the equation of mass balance

$$\frac{\partial H}{\partial x} = -\frac{\rho_g}{G_a} \cdot \frac{\partial M}{\partial t}, \quad (3.2)$$

(3) the equation of heat balance

$$\frac{\partial \theta}{\partial t} = \frac{ha(T - \theta)}{\rho_g c_g + \rho_g c_w M} + \frac{h_{fg} + c_v(T - \theta)}{\rho_g c_g + \rho_g c_w M} G_a \frac{\partial H}{\partial x}, \quad (3.3)$$

(4) the equation of heat transfer

$$\frac{\partial T}{\partial x} = -\frac{ha(T - \theta)}{G_a(c_a + c_v H)}, \quad (3.4)$$

where k is drying constant ($k = 1.091 \times 10^2 + 2.767 \times 10^{-6} T^2 + 7.286 \times 10^{-6} T M_0$); N is drying constant ($N = 0.5357 + 1.141 \times 10^{-5} M_0^2 + 5.183 \times 10^{-5} T^2$); M is the average moisture content of grain (decimal, dry basis); M_e is equilibrium moisture content (decimal, dry basis); t is drying time (min); T is air temperature ($^{\circ}\text{C}$); H is air moisture content (kg/kg); h is convective heat transfer coefficient [$\text{J}/(\text{m}^2 \cdot \text{h} \cdot ^{\circ}\text{C})$]; C_a is specific heat of dry air [$\text{J}/(\text{kg} \cdot ^{\circ}\text{C})$]; C_g is specific heat of dry grain [$\text{J}/(\text{kg} \cdot ^{\circ}\text{C})$, $C_g = 1.47 + 0.036M$]; C_w is specific heat of water [$\text{J}/(\text{kg} \cdot ^{\circ}\text{C})$]; C_v is specific heat of steam heat [$\text{J}/(\text{kg} \cdot ^{\circ}\text{C})$]; G_a is air flow [$\text{kg}/(\text{m}^2/\text{h})$]; a is valley-bed unit volume of grain surface area (m^2 , $a = 784 \text{ m}^2/\text{m}^3$); ρ_g is Grain density (kg/m^3 , $\rho_g = a_1 - a_2 M + a_3 M^2$, $a_1 = 1086.3$; $a_2 = 2971$; $a_3 = 4810$); h_{fg} is vaporization enthalpy variable of grain moisture (KJ/kg); $h_{fg} = (1094 - 0.57\theta)(1 + 4.35e^{-28.25M})$ θ is grain temperature ($^{\circ}\text{C}$).

3.2. Mathematical Models for the Prediction of Grain Germination Rate

The artificial neural network (ANN) is a well-known tool for solving complex, nonlinear biological systems, and it can give reasonable solutions even in extreme cases or in the event of technological faults. In 2003, Wenfu et al. presented a optimizing the neural network topology for predicting the seed vigor [6]. The model form is as follows:

$$Q = 1 - \frac{1}{[1 + \exp(-z)]}, \quad (3.5)$$

when $z = A + BT^\alpha + Ct^\beta + DM^\gamma$, Q is germination rate, t is drying time min, T is drying temperature $^{\circ}\text{C}$, M is moisture content of grain %, z is variable, $A, B, C, D, \alpha, \beta, \gamma$ is content through the experiment parameters estimation methods to determine [7], respectively, $A = 80.5$, $B = -8.8$, $C = -1.3$, $D = -6.48$, $\alpha = 0.5$, $\beta = 0.5$, $\gamma = 1$.

3.3. Design Structural of Simulation System

A deep bed drying model is made up of equations from (3.1) to (3.5), which has five parameters needed to be solved, namely, the average grain moisture content M , corn temperature θ , hot air temperature T after grain layer, moisture content of hot air H , and germination rate Q . The grain moisture content M can be obtained from (3.1). If we get $\partial M/\partial t$, corn temperature θ , hot air temperature T after grain layer, moisture content of hot air H , and germination rate Q can be solved accordingly. In this paper, finite difference method was used to solve these five equations. In order to reduce the prediction error, the parameters can be collected from the sensor real-time to correct the prediction model.

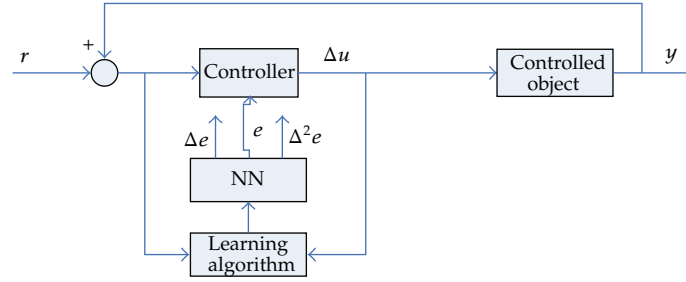


Figure 3: Neural network controller structure.

4. Control of the Controlled Parameters

4.1. Design Neural Network Controller

This paper combines the traditional PID controller with neural network technology to build neural network PID controller for controlling technological parameters. Neural network adopts three-layer feed-forward network structure; the forward numeration of network is used for the control law of PID controller, while adaptive adjustment of parameters PID controller is achieved by back propagation network algorithm [7, 8]. This neural network PID controller not only has the advantages of the traditional one, but also has parallel structure of the neural network and memory of nature learning, the ability of multilevel network to approximate any function. Control structure is shown in Figure 3.

Allowing for the control rule of incremental PID, the difference equation is that

$$\begin{aligned} \Delta u(k) &= K_P(e(k) - e(k-1)) + K_I e(k) + K_D(e(k) - 2e(k-1) + e(k-2)), \\ e(k) &= r(k) - y(k), \end{aligned} \quad (4.1)$$

where, $r(k)$ is the set value, $y(k)$ is the output value, $\Delta u(k)$ is the control increase output, and K_P , K_I , K_D are proportional, integral, and differential factors, respectively.

Therefore, we can build a neural network model for the system of single variable, the input of the network is

$$\begin{aligned} I(k) &= [v_1(k), v_2(k), v_3(k)]^T, \\ v_1(k) &= \Delta e(k) = e(k) - e(k-1), \\ v_2(k) &= e(k), \\ v_3(k) &= \Delta^2 e(k) = e(k) - 2e(k-1) + e(k-2), \\ e(k) &= r(k) - y(k), \end{aligned} \quad (4.2)$$

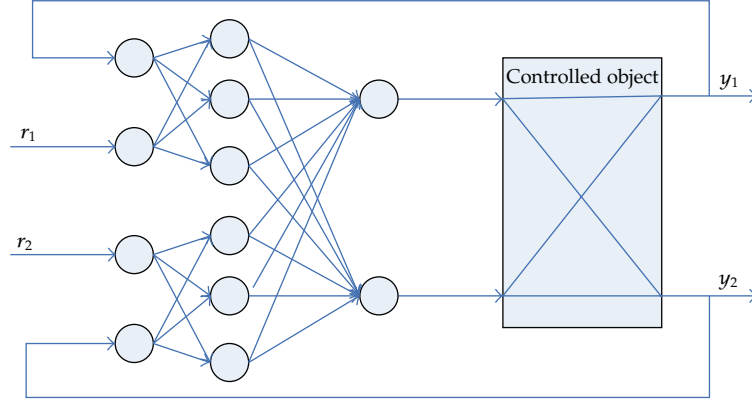


Figure 4: Biobjective control system.

where, $r(k)$ is the expectation of the system output, $y(k)$ is the actual system output, the output of neural network is the control element $u(k)$, and K_i is the weight matrix of neural network, that is, the network model is

$$u(k) = g_{NN} [e(k), \Delta e(k), \Delta^2 e(k), K_i]. \quad (4.3)$$

The network can be regarded as a nonlinear PID controller, which realizes adaptive control through automatically adjusting parameters of the PID controller by real-time correction of weighting factor K_i when parameters of the controlled object change. If the neural network is two-layer structure, and the output layer activation function is a linear, namely, $h(x) = x$, then this network can degenerate into a conventional linear PID controller. For n variables controlled system, using the n subnetworks in parallel, each subnetwork structure is aforementioned nonlinear PID network. In this system, to ensure the quality characteristics of the dried grain, predictive control over the grain discharge rate and air temperature is necessary, so a two-variable system was established; that is, two nonlinear PID networks in parallel, mutual coupling between the two variables constitute a biobjective controller. Controller structure is shown in Figure 4.

4.2. Multistep Predictive Control Algorithm for Drying Process

The system controller is a decoupling controller which is composed by the two previous nonlinear PID controllers, with control elements of air temperature and grain discharge rate, respectively [9]. Provided the i -th network input $I_i(k) = [e_i(k), \Delta e_i(k), \Delta^2 e_i(k)]^T$, where $e_i(k) = r_i(k) - y_i(k)$, variable definitions are the same as the earlier. Network output is corresponding to the i -th control element $u_i(k)$. The objective function used to modify the network weights is

$$J_i = \frac{1}{2} \sum_{j=0}^N [Y_r(k+j) - Y(k+j)]^T [Y_r(k+j) - Y(k+j)] + \frac{\lambda_i}{2} \sum_{j=0}^N [\Delta u_i(k+j)]^2, \quad (4.4)$$

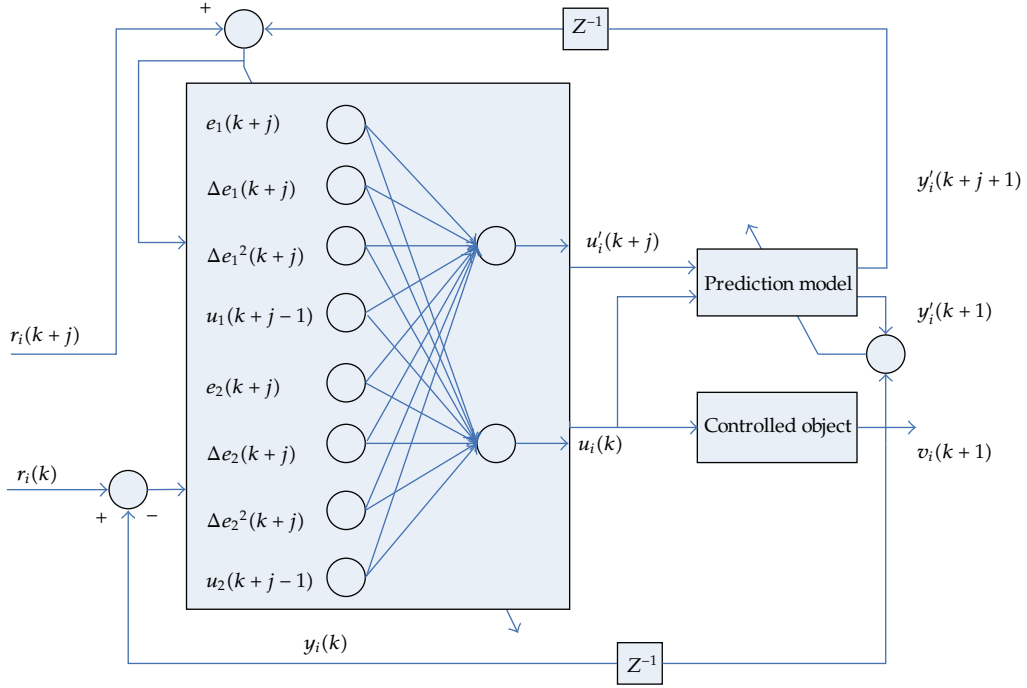


Figure 5: Neural network control system.

where $Y_r(k+j)$ is the settings soften array, and $Y_r(k+j) = [y_{r1}(k+j), \dots, y_{ri}(k+j)]^T$, N is the prediction horizon, and λ_i is control weighting factor. Block diagram of predictive control system is shown as Figure 5.

Here, we use iterative methods to evaluate the predicted system output, provided weight matrix maintained unchanged in iterative process. The detailed calculation steps are as follows.

Step 1. At present time k , let $S = 1$.

Step 2. Calculate the step forward predictive value, obtain the error signal $E(k) + [e_1(k), \dots, e_n(k)]^T$, and apply it in the decoupling controller, generating the control element $U(k) = [u_1(k), \dots, u_n(k)]^T$:

Step 3. Update the following variables:

$$\begin{aligned} U(k - n_u - 1) &= U(k - n_u), \dots, U(k - 1), \dots, U(k), \\ Y(k - n_y - 1) &= Y(k - n), \dots, Y(k - 1) = Y(k). \end{aligned} \quad (4.5)$$

Apply the above variables to the prediction model to calculate the predicted output. As the above step, obtain the corresponding error signal, and apply it in the decoupling controller, to calculate the control element $U(k+1)$ at the next moment.

Step 4. By this rule, repeat Step 2, and in turn get $Y'(k+1), \dots, Y'(k+j)$, computing multistep forward predicted output and the future time control signal.

Step 5. Correct weighting value of each control network according to objective function (4.4). Consider the following:

$$\Delta V_i(k) = V_i(k+1) - V_i(k) = -\eta_i \frac{\partial J_i}{\partial V_i(k)}. \quad (4.6)$$

From (4.4) it shows that

$$\frac{\partial J_i}{\partial V_i(k)} = \sum_{j=0}^N \left\{ \frac{\partial [\Upsilon_r(k+j) - Y(k+j)]^T}{\partial V_i(k)} \cdot \frac{\partial J_i}{\partial [\Upsilon_r(k+j) - Y(k+j)]} + \frac{\partial J_i}{\partial u_i(k+j)} \frac{\partial u_i(k+j)}{\partial V_i(k)} \right\}, \quad (4.7)$$

while

$$\frac{\partial [\Upsilon_r(k+j) - Y(k+j)]^T}{\partial V_i(k)} = \frac{\partial [\Upsilon_r(k+j) - Y(k+j)]^T}{\partial u_i(k+j)} \frac{\partial u_i(k+j)}{\partial V_i(k)}, \quad (4.8)$$

so

$$\frac{\partial J_i}{\partial V_i(k)} = \sum_{j=0}^N \left\{ -\frac{\partial Y^T(k+j)}{\partial u_i(k+j)} [\Upsilon_r(k+j) - Y(k+j)] + \lambda_i \cdot \Delta u_i(k+j-1) \right\} \frac{\partial u_i(k+j)}{\partial V_i(k)}, \quad (4.9)$$

taking it into (4.6), we get

$$\Delta V_i(k) = -\eta_i \cdot \sum_{j=0}^N \left\{ -\frac{\partial Y^T(k+j)}{\partial u_i(k+j)} [\Upsilon_r(k+j) - Y(k+j)] + \lambda_i \cdot \Delta u_i(k+j-1) \right\} \frac{\partial u_i(k+j)}{\partial V_i(k)}. \quad (4.10)$$

4.3. Control System Establishment

Figure 6 shown is the main interface of control system; this interface mainly includes information such as the drying process online collection of digital information, digital and graphical display, control process parameters display, file save path, communication ports choice, and moisture sensor calibration parameters.

5. System Application and Testing

To verify the actual operation effect of the controller, it was tested on two drying machines in series connection, the drying machine is model 5HSZ-30 small crossflow continuous dryer, and the test site is in Gongzhuling Jilin Grain trading company depots. Test material is the horse tooth corn provided by the company grain depots. During the test, corn moisture

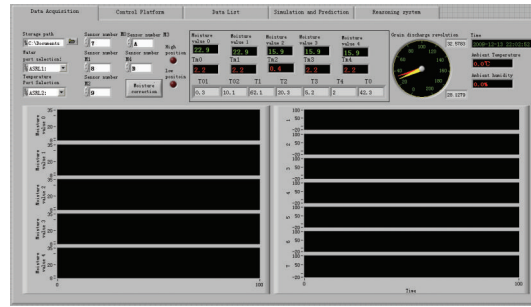


Figure 6: The main interface of control system.

Table 1: Test conditions and measurement results (average value).

Test conditions	Dryer I	Dryer II
Capacity/kg	10000	10000
Initial moisture content (wet basis)/%	27.31	18.26
Unprocessed grain temperature/°C	-0.7	32
Ambient temperature/°C	-1.0	-1.0
Relative humidity of ambient/%	45	45
Fan flow/m ³ /min	150	150
Hot air temperature/°C	85.8	109.4
Relative humidity of exhaust gas/%	65	58
Feed rate/kg/h	1773	1716

content, grain discharge rate, hot air temperature and humidity at intake and exit, ambient air temperature, and humidity, sampling, and so forth are recorded. Data at a relative stable test phases was selected as the actual measured results and compared these results with data in manual control process to verify whether the control system meets with application requirements. Table 1 shows the test condition parameters.

The requirements of the control system are as follows.

- (1) The corn moisture content after drying remains stable and uniform ($\pm 0.5\%$) and close to the requirements of the moisture (14%).
- (2) Improve the relative germination rate of the corn after drying.

The production test was made in January 2008. The test site is shown in Figures 7, 8, and 9 which are the temperature change curves of each measurement point under the manual control and the automatic control condition. Figures 10 and 11 are the change curves of the corn moisture and the relative germination rate after drying under the manual control and the automatic control condition. In manual and automatic control processes, corn initial moisture fluctuations were 23.5%–27.4% and 23.7%–27.6%, mean square error was 0.84 and 0.96, respectively, which shows that they were basically in the same initial conditions. Exit moisture (oven method) fluctuations were 13.5%–14.6% and 13.6%–14.3%, variances were 0.98 and 0.58, which can be seen in the automatic control process, the exit dried grain has a smaller moisture fluctuation, and the control accuracy was higher than manual control. For the relative germination rate, as model prediction was adopted in the automatic process, air temperature and discharge rates were adjusted timely, which had a relative germination rate of 80.16%, higher than 70.05% in manual control process, and significantly improved



Figure 7: Test site.

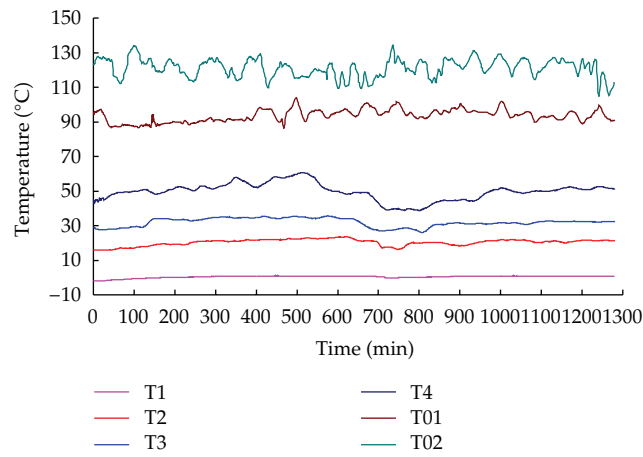


Figure 8: Air temperature and food temperature curve of manual control process.

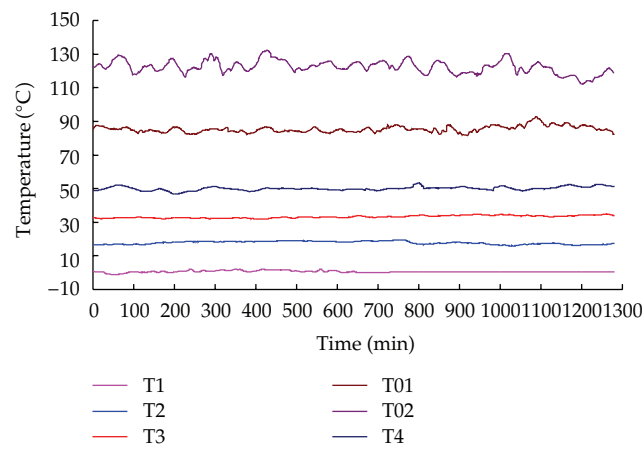


Figure 9: Air temperature and food temperature curve of Automatic control process.

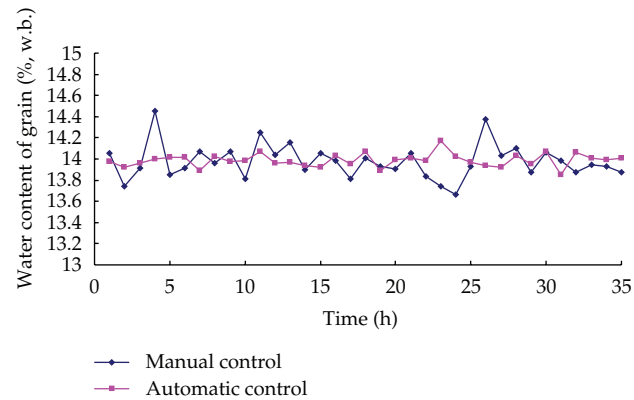


Figure 10: The water content of grain in manual and automatic mode.

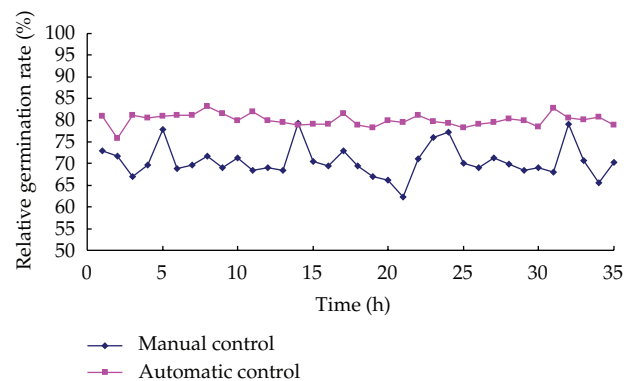


Figure 11: The relative germination rate of grain in manual and automatic mode.

the quality of dried corn. Relative germination rate fluctuations for manual and automatic controls were 61.3%–78.4% and 75.9%–83.1%, deviations were 13.67 and 1.98, respectively, and stabilities of dried grain after automatic control were higher than that of manual control. From the above analysis it can be seen, the system greatly enhanced the accuracy and stability of exit corn moisture content and quality, and suitable for production application.

6. Conclusions

A model predictive control system based on neural network was designed and tested on two 5HSZ-30 model corn dryers. The test showed that the control method of the system can be used in drying process control and intelligent control, and it can provide a considerable reference for the precise control of drying process. The stability and robust of the system are better than before. The specific conclusions are as follows.

- (1) In the automatic control system, the fluctuation of corn moisture and relative germination rate after drying is small, and the system improves the uniformity of moisture content and relative germination rate.

- (2) In the automatic control system, it increased the control of the temperature, so the thermal denaturation of corn and the influence of temperature to the quality of corn are decreased, and relative germination rate of drying machine export corn is increased.
- (3) In the automatic control process, the interferences of human are reduced, the quality of the corn is ensured, so the labor costs can be reduced, and the economic value of the corn can be increased.

Acknowledgment

This work is supported by the High-Tech Research and Development Program of China (863 Program) (2006AA10Z256).

References

- [1] L. Xueqiang, *Complexity Analysis and Process Control for Grain Drying*, Jilin University, Changchun, China, 2006.
- [2] Q. Liu and F. W. Bakker-Arkema, "A model-predictive controller for grain drying," *Journal of Food Engineering*, vol. 49, no. 4, pp. 321–326, 2001.
- [3] Q. Liu and F. W. Bakker-Arkema, "Automatic control of crossflow grain dryers, Part 1: development of a process model," *Journal of Agricultural Engineering Research*, vol. 80, no. 1, pp. 81–86, 2001.
- [4] C. Chongwen and Z. Wenxue, *Computer Simulation of Agricultural Drying Process [M]*, China Agriculture Press, Beijing, China, 2001.
- [5] Q. Liu, *Stochastic Modeling and Automatic Control of Grain Dryers: Optimizing Grain Quality*, Michigan State University, 1998.
- [6] W. Wenfu, X. Yanhui, and Z. Xuedu, "Predictive Model for Post-dried Seed Viability by Its Super-weak Bioluminescence," *Transactions of the Chinese Society of Agricultural Machinery*, vol. 34, pp. 43–46, 2003.
- [7] W. Yi, H. Weiping, and D. Huiwen, "A self-adaptive PID controller based on neural network identification," *Journal of Southwest China Normal University*, vol. 29, pp. 41–44, 2004.
- [8] W. Zhimin and L. Shuchen, "Adaptive PID control based on dynamic recurrent neural network," *Control Engineering*, vol. 3, pp. 216–219, 2004.
- [9] Z. Yan, W. Fanzhen, and C. Zengqiang, "Recurrent neural networks-based multivariable system predictive control," *Acta Scientiarum Naturalium Universitatis Nankaiensis*, vol. 39, pp. 49–54, 2006.

Research Article

Model of Mass and Heat Transfer during Vacuum Freeze-Drying for Cornea

**Zou Huifen,¹ Ye Sheng,² Wang Dexi,³ Li Huixing,¹
Cao Xiaozhen,¹ and Yan Lijun¹**

¹ School of Municipal and Environment Engineering, Shenyang Jianzhu University, Shenyang 110168, China

² Management School, Shenyang Jianzhu University, Shenyang 110168, China

³ School of Chemical Engineering Equipment, Shenyang University of Technology, Liaoyang 111003, China

Correspondence should be addressed to Zou Huifen, jerry_zou@163.com

Received 22 March 2012; Accepted 3 May 2012

Academic Editor: Zhijun Zhang

Copyright © 2012 Zou Huifen et al. This is an open access article distributed under the Creative Commons Attribution License, which permits unrestricted use, distribution, and reproduction in any medium, provided the original work is properly cited.

Cornea is the important apparatus of organism, which has complex cell structure. Heat and mass transfer and thermal parameters during vacuum freeze-drying of keeping corneal activity are studied. The freeze-drying cornea experiments were operated in the homemade vacuum freeze dryer. Pressure of the freeze-drying box was about 50 Pa and temperature was about -10°C by controlled, and operating like this could guarantee survival ratio of the corneal endothelium over the grafting normal. Theory analyzing of corneal freeze-drying, mathematical model of describing heat and mass transfer during vacuum freeze-drying of cornea was established. The analogy computation for the freeze-drying of cornea was made by using finite-element computational software. When pressure of the freeze-drying box was about 50 Pa and temperature was about -10°C , time of double-side drying was 170 min. In this paper, a moving-grid finite-element method was used. The sublimation interface was tracked continuously. The finite-element mesh is moved continuously such that the interface position always coincides with an element node. Computational precision was guaranteed. The computational results were agreed with the experimental results. It proved that the mathematical model was reasonable. The finite-element software is adapted for calculating the heat and mass transfer of corneal freeze-drying.

1. Introduction

The storage of isolated freeze-drying biological tissue is a significant field in the application of vacuum freeze-drying technology and studies for its mass and heat transfer theory under low-temperature, low-pressure conditions which have already become a hot frontal topic in theoretical researches. The vacuum freeze-drying of cornea (freeze-dry) is the freeze-drying for isolated biological tissue which has to remain active afterwards.

The first step during a freeze-drying process is prefreeze, which could affect the activity and the drying rate of cornea. Drying process is to remove the moisture inside cornea, while heat and mass transfer is progressing on a much harder and more complex level. In a drying process of medicine or food, ambient temperature could be increased moderately to provide sufficient heat or heating the material directly in the second step and the resolution process of adsorbed moisture could hence been accelerated which results in a more cost-effective way of freeze-drying. Time and cost is not a critical factor during a freeze-drying process, it is all about to reduce the risk of cornea being spoiled throughout the drill. Therefore, the time should be minimized in freeze-drying of cornea in order to obtain higher survival chance for corneal endothelial cells. But due to the limitation of corneal cell's configuration, underneath the external surface (endothelial cell and epidermal cell), there is an elastic layer that resists the diffusion of the moisture within the matrix (moisture in the matrix count for 90% of the overall water content). If the temperature of sublimation front is too high, as higher level of vapor in sublimation, the internal pressure in the cornea will rise correspondingly, which leads to two circumstances as follow. (1) If the vacuum degree inside the freeze-drying chamber is high and the pressure is low at the meantime, the inner and outer pressure of cornea would achieve a relatively high level that leads to the exposure of moisture inside the cornea through the external surface. Epidermal cell and endothelial cell might drop off, leading to the whole process become meaningless. (2) If the pressure within the drying chamber is at an appropriate rate with the pressure of the cornea, but the temperature of sublimation interface is swelling up which leads to vapor increase and melting of the freeze-layer, resulting in death or injury of cells and loss of the freeze-drying condition. By calculating the theoretical model, seeking for the appropriate temperature and pressure for the will of freeze-drying experiment results could be insured as being optimized and stabilized.

A number of models on freeze-drying have been mentioned in many researches [1–11] aiming to describe the process. The sorption-sublimation model presented by Liapis and Litchfield is the most widely used one and character as the synch of sorption and sublimation of moisture, also, the removal of bounded water is considered in the equation. The result of this modeling agrees with Moffert's research. However, the model is of one dimension, in the process of freeze-drying, the sublimate interface arises with the drying procedure. Liapis and Litchfield employ a one-dimensional moving interface [12], thus the prerequisite of material applied have to be one-dimension with no bent at any angle. Tang et al. [13] have modified this model into two dimensions to describe the freeze-drying of drugs in the penicillin vial, this 2D model could accurately reflect the position and shape of the sublimation interface, ergo; it can simulate the actual progress. Millman et al. have further the model that presented by Tang [14], in which the new model could allow the material form in arbitrary shape. The characteristics of this model is to involve more factors with less limitation, therefore, it has been widely used. But due to the complexity of the model, and the numerous parameters that have to be considered, the application of this model run encounters difficulties.

Models mentioned above were solved by program which developed by themselves, and studied material is at least more than 5 mm, and the cornea is only 0.6 mm thick. The use of the material has certain degree of difficult as the heat and mass transfer have their own characteristics. This article combine the advancement of Millman's model and finite element analysis software, constructing the 2D model of freeze-drying process of cornea that allow the sublimation and desorption happen simultaneously, taking into account of the removal of bounded moisture. Also, 2D approach has been applied to fix the mobile interface. Small-scale changes base on the present software have been done to simulate the heat and mass transfer

of freeze-drying cornea. The calculated results are basically consistent with the experimental data and more details have described as follows.

2. Establishment of Mathematical Model

2.1. Hypothesis

The establishment of mathematical model is referred to the coupled equation of heat and mass transfer which is developed by Millman. In this article, assumptions have been made as follows, relating to the establishment of finite element model.

- (1) The 2D dimensional heat and mass transfer is considered.
- (2) The interface thickness was thought to be infinitely small (the assumption has been confirmed in many researches [15]).
- (3) The mixture of water vapor and permanent gases flow passes the drying layer.
- (4) The concentration of vapor and ice phase equilibrium is at the interface.
- (5) The semidry layer is a porous region due to the back of sublimation interface, dry-material, and adsorbed-water (solid phase) were inside the region. The gas consists of vapor and permanent gases, which were considered to maintain thermal equilibrium with the solid phase.
- (6) Surface and interface temperature stay unchanged.
- (7) The frozen zone is assumed to be uniform and has uniform thermal conductivity, density and specific heat, also it contains small amount of dissolved gases.
- (8) Changes of the overall size of cornea are out of question.
- (9) The total pressure of the drying chamber was controlled by appropriate-size vacuum pump and required devices (most of the permanent gases in the chamber was considered leak in).

2.2. Mass Transfer Equation

Continuity equations of dry-layer can be expressed as follows:

$$\varepsilon \frac{DC_{gw}}{Dt} + \rho_1 \frac{DC_{sw}}{Dt} + \nabla \cdot N_w = 0, \quad (2.1)$$

$$\varepsilon \frac{DC_{gin}}{Dt} + \nabla \cdot N_{in} = 0, \quad (2.2)$$

in which

$$\frac{DC_{sw}}{Dt} = k_g(C_{sw}^* - C_{sw}), \quad (2.3)$$

$$N_w = -k_1 \nabla C_{gw} - k_2 C_{gw} \nabla P, \quad (2.4)$$

$$N_{in} = -k_3 \nabla C_{gin} - k_4 C_{gin} \nabla P, \quad (2.5)$$

$$P = P_w + P_{in}, \quad (2.6)$$

$$C_{sw}^* = f(P_w, T_1), \quad (2.7)$$

C_{sw}^* is the density of water in solid phase when water-gas equilibrium was achieved.

Equations (2.4) and (2.5) are the mass-trans rate formula of binary mixture pass through the dry zone, based on diffusion equation (Evans et al. [16]) and viscous flow formula (D'Arcy). In the formula, the main vapor diffusion is passing through the dry layer, and escaping by way of Knudsen diffusion and the corresponding total pressure gradient; also with no consideration of surface diffusion and thermal diffusion model as such diffusion is not significant [17]. It has been proved that the role of viscous flow is not that important for N_w and N_{in} [18]. Knudsen diffusion is the most important one in the case of low/permanent gas nonexistent. However, main diffusion controls the rate when they do exist. Therefore, (2.4) and (2.5) can be simplified as

$$N_w = -k_1 \nabla C_{gw}, \quad (2.8)$$

$$N_{in} = -k_3 \nabla C_{gin}.$$

By (2.1) and (2.4), we obtain:

$$\varepsilon \frac{DC_{gw}}{Dt} + \rho_1 \frac{DC_{sw}}{Dt} = \nabla \cdot (k_1 \nabla C_{gw}). \quad (2.9)$$

By (2.2) and (2.5), we obtain

$$\varepsilon \frac{DC_{gin}}{Dt} = \nabla \cdot (k_3 \nabla C_{gin}). \quad (2.10)$$

The work in [17] has proved that permanent gas got a very small change rate; (2.9) could hence be solved without (2.10). Therefore, the following manipulating only includes finite element formulation for (2.9).

In the 2D symmetric space, (2.9) can be expressed as

$$\varepsilon \frac{DC_{gw}}{Dt} + \rho_1 \frac{DC_{sw}}{Dt} = k_1 \left[\frac{\partial}{\partial x} \frac{\partial C_{gw}}{\partial x} + \frac{1}{r} \frac{\partial}{\partial y} \left(r \frac{\partial C_{gw}}{\partial y} \right) \right]. \quad (2.11)$$

Under low pressure, the concentration of water vapor and permanent gases can be expressed by using the ideal gas law:

$$M_i P_i = C_{gi} RT. \quad (2.12)$$

So, (2.11) can be described by the following equation:

$$\frac{\varepsilon M_w}{RT_1} \frac{DP_w}{Dt} + \rho_1 \frac{DC_{sw}}{Dt} = \frac{k_1 M_w}{RT_1} \left[\frac{\partial}{\partial x} \frac{\partial P_w}{\partial x} + \frac{1}{r} \frac{\partial}{\partial y} \left(r \frac{\partial P_w}{\partial y} \right) \right], \quad (2.13)$$

and assuming that

$$A_1 = \frac{\varepsilon M_w}{RT_1}, \quad A_2 = \frac{k_1 M_w}{RT_1}, \quad F_1 = \frac{\partial P_w}{\partial x}, \quad F_2 = \frac{\partial P_w}{\partial y}, \quad (2.14)$$

by (2.13) and (2.14), we obtain

$$A_1 \frac{DP_w}{Dt} + \rho_1 \frac{DC_{sw}}{Dt} = A_2 \left[\frac{\partial F_1}{\partial x} + \frac{1}{r} \frac{\partial}{\partial y} (r F_2) \right]. \quad (2.15)$$

2.3. Heat Transfer Equation

In a 2D symmetric space, energy equation for dry-layer is

$$\rho_{1e} C_{P1e} \frac{DT_1}{Dt} - k_{1e} \left[\frac{\partial}{\partial x} \frac{\partial T_1}{\partial x} + \frac{1}{r} \frac{\partial}{\partial y} \left(r \frac{\partial T_1}{\partial y} \right) \right] + C_{Pg} \left[\frac{\partial (N_{tx} T_1)}{\partial x} + \frac{1}{r} \frac{\partial (N_{ty} T_1)}{\partial y} \right] - \Delta H_v \rho_1 \frac{\partial C_{sw}}{\partial t} = 0. \quad (2.16)$$

Frozen layer energy equation is

$$\rho_{II} C_{PII} \frac{DT_{II}}{Dt} - k_{II} \left[\frac{\partial}{\partial x} \frac{\partial T_{II}}{\partial x} + \frac{1}{r} \frac{\partial}{\partial y} \left(r \frac{\partial T_{II}}{\partial y} \right) \right] = 0. \quad (2.17)$$

2.4. Concentration Equation

Moisture concentration change in the dry layer versus time can be described as

$$\frac{DC_{sw}}{Dt} = k_g (C_{sw}^* - C_{sw}). \quad (2.18)$$

2.5. Initial and Boundary Condition

When $t = 0$,

$$\begin{aligned} P &= P^0, \\ T_I &= T_{II} = T^0, \\ C_{sw} &= C_{sw}^0. \end{aligned} \quad (2.19)$$

When $t > 0$,

$$\begin{aligned} P &= \hat{P}, \\ T &= \hat{T}. \end{aligned} \quad (2.20)$$

Equation (2.20) specified the boundary value of pressure and temperature. The concentration equation is an issue relating to initial value, with no consideration of any boundary conditions.

3. The Trajectory of the Sublimation Interface

During the process of drying, the sublimation latent heat was released at the sublimation interface, and the sublimation heat was added as boundary condition when solving a series of control equation. It, hence, becomes necessary to track the location of the interface and impose boundary conditions on the interface spot. The movement of the interface is affirmed by exam the equilibrium of heat at the interface. In the case of noninternal heat source, the heat originates from the dried layer equals to the total heat both from the absorption and the heat flowed to the frozen layer. The heat balance equation can be expressed as follows:

$$k_{II} \frac{\partial T_{II}}{\partial n} - k_{1e} \frac{\partial T_1}{\partial n} + N_{tn} C_{Pg} T_1 = -v_n (\rho_{II} C_{P_{II}} T_{II} - \rho_1 C_{P_1} T_1) - \Delta H_s N_{tn}, \quad (3.1)$$

in which

$$v_n = -\frac{N_{wn}}{\rho_{II} - \rho_1}. \quad (3.2)$$

The velocity of interface v_n perpendicular to the interface itself, and v_n could conclude from (3.2) in order to obtain the new interface location. Numerous numerical calculation techniques were used to solve the problem of moving interface, in the paper, however, the finite-grid-element method has been used [13], where the sublimation interface was tracked consecutively and the interface was assumed to be boundary condition of the move. The finite grid would be redivided when changes occur in the sublimation interface, by doing this, to fix the interface location always at the unit node. In other words, instead of stay in the unit, the interface location would always be on the outline or node of the unit, and so the boundary conditions would be added on the contour line. Therefore, the equation of both

dry and frozen layers can be solved together with the combination of interface boundary conditions.

4. Finite-Element Formulations

Variational equation within the finite element defines the formulation (2.15) and (2.18) as

$$\int_{\Omega^e} \left[w A_1 \left(\frac{\partial P_w}{\partial t} - g_x \frac{\partial P_w}{\partial x} - g_y \frac{\partial P_w}{\partial y} \right) + A_2 \frac{\partial w}{\partial x} F_1 + A_2 \frac{\partial w}{\partial y} F_2 + \rho_1 \frac{DC_{sw}}{Dt} w \right] r dx dy$$

$$- \oint_{\Gamma^e} w [A_2 F_1 n_x + A_2 F_2 n_y] dS = 0, \quad (4.1)$$

$$\int_{\Omega^e} \left\{ w \rho_{1e} \left(\frac{\partial T_1}{\partial t} - g_x \frac{\partial T_1}{\partial x} - g_y \frac{\partial T_1}{\partial y} \right) + k_{1e} \left[\frac{\partial w}{\partial x} \frac{\partial T_1}{\partial x} + \frac{\partial w}{\partial y} \frac{\partial T_1}{\partial y} \right] \right.$$

$$\left. - C_{Pg} \left[\frac{\partial w}{\partial x} (N_{tx} T_1) + \frac{\partial w}{\partial y} (N_{ty} T_1) \right] - \Delta H_v \rho_1 \frac{DC_{sw}}{Dt} w \right\} r dx dy \quad (4.2)$$

$$- \oint_{\Gamma^e} \left(k_{1e} \frac{\partial T_1}{\partial x} n_x + k_{1e} \frac{\partial T_1}{\partial y} n_y \right) w dS$$

$$+ \oint_{\Gamma^e} C_{Pg} [w (N_{tx} T_1) n_x + w (N_{ty} T_1) n_y] dS = 0,$$

$$\int_{\Omega^e} \left[w \rho_{II} C_{PII} \left(\frac{\partial T_{II}}{\partial t} - g_x \frac{\partial T_{II}}{\partial x} - g_y \frac{\partial T_{II}}{\partial y} \right) + k_{II} \left(\frac{\partial w}{\partial x} \frac{\partial T_{II}}{\partial x} + \frac{\partial w}{\partial y} \frac{\partial T_{II}}{\partial y} \right) \right] r dx dy \quad (4.3)$$

$$- \oint_{\Gamma^e} \left(k_{II} \frac{\partial T_{II}}{\partial x} n_x + k_{II} \frac{\partial T_{II}}{\partial y} n_y \right) w dS = 0,$$

$$\int_{\Omega^e} w \left[\left(\frac{\partial C_{sw}}{\partial t} - g_x \frac{\partial C_{sw}}{\partial x} - g_y \frac{\partial C_{sw}}{\partial y} \right) - k_g (C_{sw}^* - C_{sw}) \right] r dx dy = 0, \quad (4.4)$$

in which w represents the finite element weight equation, Γ^e is the sum of the computational domain Ω^e 's boundary, while n_x and n_y are the direction cosine of n . Boundary term in (4.1)–(4.3) can be defined as follows:

water vapor flow

$$N_{wn} = N_{wx} n_x + N_{wy} n_y = A_2 F_1 n_x + A_2 F_2 n_y, \quad (4.5)$$

heat flow:

$$q_n = q_x n_x + q_y n_y = -k_{1e} \frac{\partial T_1}{\partial x} n_x - k_{1e} \frac{\partial T_1}{\partial y} n_y \quad (\text{dry area})$$

$$= -k_{II} \frac{\partial T_{II}}{\partial x} n_x - k_{II} \frac{\partial T_{II}}{\partial y} n_y \quad (\text{frozen region}), \quad (4.6)$$

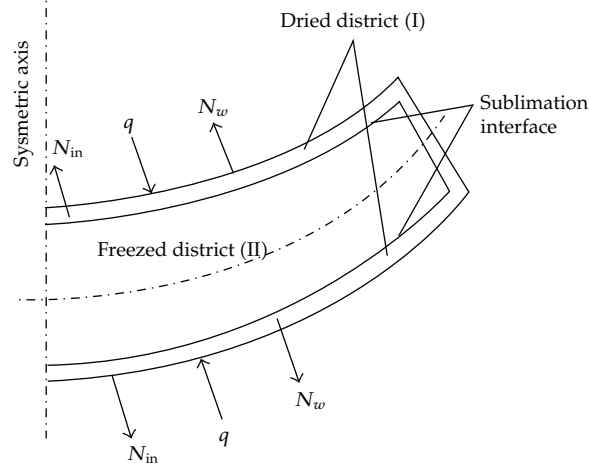


Figure 1: Schematic of cornea freeze drying.

the total flow:

$$N_{tn} = N_{tx}n_x + N_{ty}n_y. \quad (4.7)$$

5. Results and Discussion of the Frozen Model

Figure 1 is an illustration of a sided schematic lyophilized. At the beginning of calculation, the initial dry layer thickness needs to be determined, and the equation would be unsolved when the freeze starts and the thickness of dried layer is zero. Similarly, it is required to determine the residual value of the frozen layer when the frozen layer thickness trends to be zero [19]. As the test results tell, the initial thickness of frozen layer would be 6×10^{-6} m, and for residual layer thickness, the value should be 1×10^{-6} m as shown in Table 1.

5.1. The Relationship between Lyophilized Chamber Pressure and Drying Time

In the process of freeze the cornea, radiation heat is the dominating way of heating. During the radiation heating, sublimation starts at the frozen material surface, which gradually forms an interface between the dried layer and frozen layer (as shown in Figure 1). The heat passes through the porous dried layer by thermal conductivity and spreads to the sublimation interface, adsorbed by the ice sublimation process simultaneously. The vapor emerged from the diffusion spread along the opposite direction of heat from the sublimation interface to the dry layer. Also, the sublimation interface moves inwards gradually until the frozen water disappears and the sublimation come to an end. So, the moving rate of the interface could stand for the lyophilized rate.

The speed of the freeze-dry process depends on the sublimation of ice and the diffusion rate of vapor, the former indicator is also determined by the intensity of heat transfer to the sublimation interface, hence, the drying process is controlled by tow mechanisms. Filled with vapor and small amount of air, the gas thermal conductivity rate inside the dried

Table 1: Parameter values during computing [14, 20, 21].

Nomenclature	Unit	Value
C_{sw}^*	kg water/kg solid	$0.01 \exp(2.3(1.36 - 0.036(T - T^0)))$
C_2	—	0.4428
C_{p1}	kg/kg·K	2.595
C_{pII}	kg/kg·K	1.9678
C_{Pg}	kg/kg·K	1.6747
ρ_1	kg/m ³	209.3
ρ_{II}	kg/m ³	910
ε	—	0.706
ΔH_s	KJ/Kg	2834.6
ΔH_V	KJ/Kg	2499.6
$P_w _{intf}$	Pa	$133.32[\exp(23.9936 - 2.19\Delta H_s/T_{intf})]$
$D_{w,in}^0$	kg·m/s ³	$8.729 \times 10^{-7}(T_0 + T_{intf})^{2.334}$
k_{1e}	W/m·K	$0.68(12.98 \times 10^{-8}P + 39.806 \times 10^{-6})$
k_{II}	W/m·K	0.146
k_g	1/s	1.108×10^{-4}
K_w	m ² /s	$1.429 \times 10^{-4}(T_0 + T_{intf})^{0.5}$

layer arises with the pressure increase. Therefore, when the pressure rises in the freeze-dry chamber, the effective thermal conductivity of the dried layer would arise and provide heat to the sublimation interface which accelerates the process. The driving force of vapor is the differential pressure of the sublimation and dried layer. The vapor pressure on the sublimation interface can be assumed equal to the saturation pressure under the interface temperature. When the temperature of the lyophilized chamber arises, the partial pressure of the dried layer increases which slows down the vapor diffusion rate control by the dried layer differential pressure of mass transfer. Clearly, the pressure of lyophilized chamber impact oppositely to the ice crystal simulation rate and water vapor diffusion rate, that is, to double impact the lyophilize process both boost and retard the process. Apparently, there should be a certain pressure that optimizes the freeze-drying rate [22, 23]. During the cornea lyophilized process, there also exists an optimum value for the chamber, which can both ensure the endothelial cell survival chance and taking into account the lyophilized rate.

Figure 2 shows the lyophilized cornea freeze time under the condition of the pressure 20 Pa, 50 Pa, 80 Pa, 110 Pa. As can be concluded from the figure, the time for freeze dry the cornea basically equals to the pressure when it is below 50 Pa, then as the pressure increases, the time needed increases accordingly. The simulation results and the experimental test afterwards conclude that the chamber pressure should be over 50 Pa if more than 80% of the survival rate is required.

5.2. The Relationship between Temperature of Sublimation Interface and Time of Drying

In the process of freeze-drying, as the ice is sublimating, the interface between the porous dried layer and the frozen layer will be continuously moving backward, inducing the increase

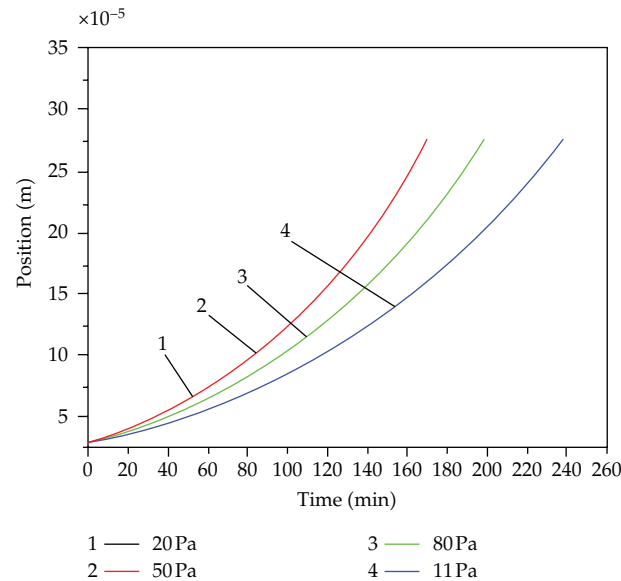


Figure 2: The calculated sublimation interface positions versus time at various chamber pressures.

of water vapor diffusion resistance at the sublimation interface and the rise of interface temperature [24–27], as shown in Figure 3. When the temperature of condenser's surface is constant, the interface temperature would be the main parameter to determine water vapor diffusion intensity. In previous studies, the interface temperature was assumed to be a constant value [28, 29], some experts believe that the assumption will decrease the simulation analysis precision, and they assume the sublimation interface temperature in the process of freeze-drying is gradually rising. They replace the constant interface temperature in the previous studies with the linear expression between the sublimation interface temperature and the location, thereby improving the mass transfer model in freeze-drying process. Figure 3 shows that when the sublimation interface of freeze-dried material moves 30 cm, its temperature just increases by 6°C, and corneal thickness is around 0.6 mm, so in this simulation, it is viable to assume the interface temperature is constant.

The temperature of sublimation interface, the temperature of condenser surface, and the pressure of freeze-drying chamber are correlated. If the temperature of sublimation interface is lower, the sublimation interface saturation pressure is lower accordingly, which requires the lower freeze-drying chamber pressure and lower condenser surface temperature. The relationship among them indicates that the saturation pressure of sublimation interface > the pressure of freeze-drying chamber > the saturation pressure of condenser surface. During the stages of a freeze-drying process, when the condenser surface temperature is -40°C, it affects little on shortening the time of freeze-drying. When the condenser surface temperature declines from -40°C to -100°C, the time of freeze-drying reduces just by 4%. The influence tends to be similar to the results of Millman's study on skim milk freeze-drying [30]. Too low temperature of the condenser surface does not greatly improve the differential pressure of water vapor diffusion, which is determined by the exponential function between the saturation pressure and temperature. Instead, if the sublimation interface temperature would be increased dramatically, which increases the differential pressure of water vapor

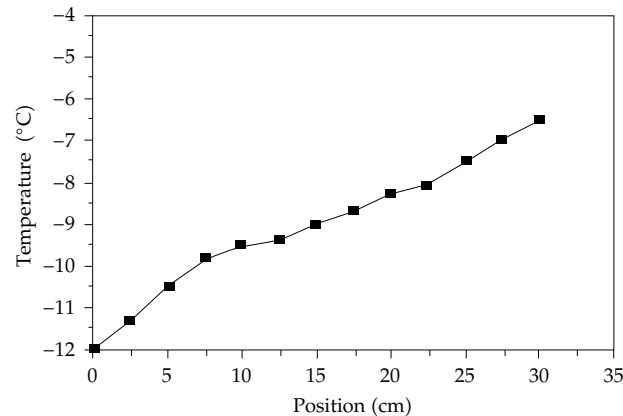


Figure 3: Relationship between temperature and position of sublimation interface.

diffusion (the saturated pressure is 260 Pa, when it is -10°C), the time of freezing can be reduced distinctly.

During the process of corneal freeze-drying, sublimation interface temperature cannot be in -30°C to -60°C , within which biological cells are at risk. If the temperature of the sublimation interface is below -60°C , it will not only reduce the temperature of the condenser surface, but also can make the time of freeze-drying much longer causing the increase of the damaged cornea chance. The experiment indicates that the corneal endothelial survival chance can achieve the standard value if the sublimation temperature is fixed around -10°C .

5.3. The Relationship between Differential Surface Temperature and the Time of Drying

Figure 4 shows the computational results of double-sided freeze-dried model of Figure 1. In Figure 4, the pressure in the freeze-drying chamber is 50 Pa, and the surface temperatures are -10°C , 0°C , and 10°C , respectively. Three curves are basic coincident, confirming that the variation of surface temperature is from -10°C to 10°C , it has little a influence on the corneal freeze-drying process.

5.4. Simulative Calculation Performed when the Pressure of Freeze-Drying Chamber Is 50 Pa and Corneal Surface Temperature Is 10°C

- (1) The computational results illustrated in Figure 5 include two-sided freeze-dried model simulation and the change of sublimation interface with the freeze-drying process. As can be seen in the figure, in the initial stage of corneal freeze-drying, the position of sublimation interface moves quite smoothly. And at the end of drying, the slope of curve increases, which illustrates that the speed of the mobile sublimation interface increases. As the positive relationship between interface mobile rate and freeze-dried rate, the freeze-dried rate can be observed from the interface moving speed. Time of double-side freeze-drying was 170 mins.
- (2) Figure 6 shows the results of the unit applying temperature and pressure load.

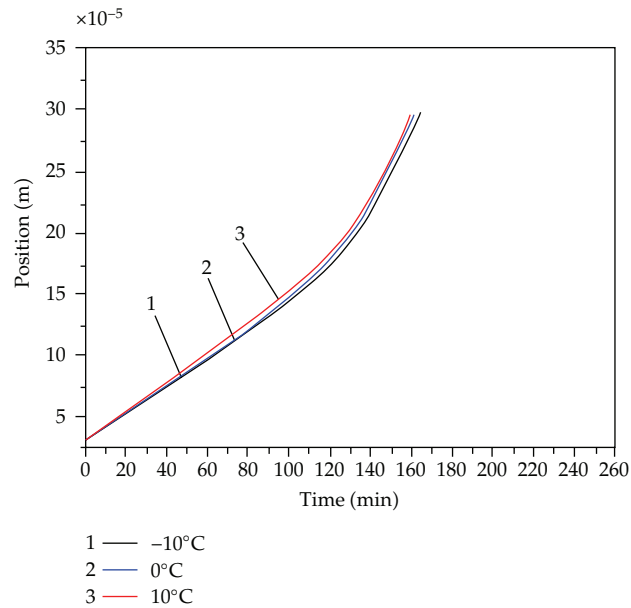


Figure 4: The calculated sublimation interface positions versus time at various surface temperatures.

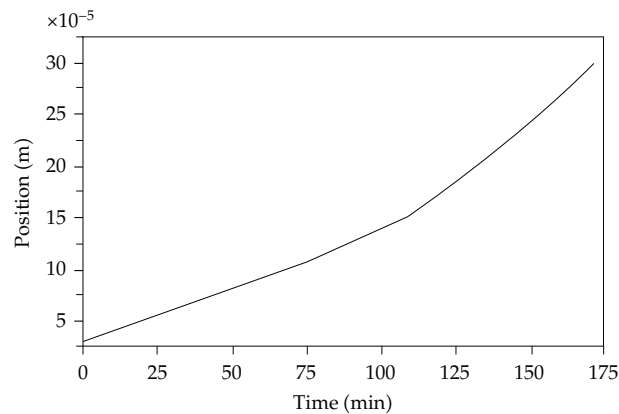


Figure 5: Relationship between position of sublimation interface and time.

6. Conclusions

- (1) Mathematical model describing heat and mass transfer during vacuum freeze-drying of cornea is established through theory analysis of corneal freeze-drying. The analogy computation for the freeze-drying of cornea was made by using the finite-element computational software. When the pressure of the freeze-drying box is around 50 Pa and temperature is around -10°C , Time of double-side drying was 170 mins.
- (2) In this paper, a moving-grid finite-element method is used to track the parameters node continuously to increase the experiment accuracy, also, the results are evident with clear physical significance.

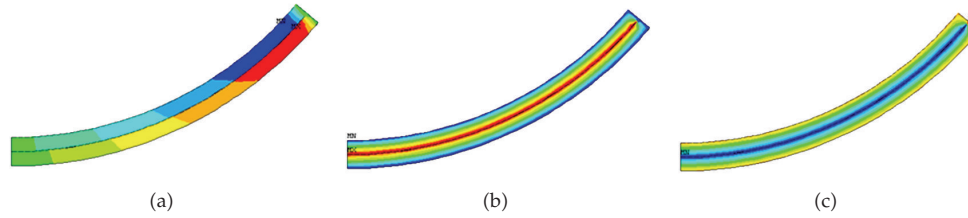


Figure 6: The flux pressure and temperature nephogram of cornea at the end.

Nomenclature

- C_{sw} : Concentration of the water in the adsorption phase (or solid phase), the number of moles (or mass) per unit volume of frozen phase (kg water/kg solid)
- C_{pi} : Specific heat of the component i (kJ/kg·K)
- C_{gi} : Concentration of the component i in gas phase, the number of moles (or mass) per space unit volume of frozen phase
- N_i : The flow rate of the component i (kg/m²s)
- N_w : The flow rate of water vapor in the already dried layer (kg/m²s)
- N_{in} : The flow of permanent gas in the already dried layer (kg/m²s)
- N_t : Full flow in the already dried layer (kg/m²s)
- k : Coefficient of thermal conductivity (kW/m·K)
- k_g : Coefficient of internal mass transfer with analytical function (s⁻¹)
- k_1 : Diffusion rate constant of the main body ($C_2 D_{w,in}^0 K_w / (C_2 D_{w,in}^0 + K_{mx} P)$)
- k_2 : Self-diffusion rate constant ($K_w K_{in} / (C_2 D_{w,in}^0 + K_{mx} P) + (C_{01} / \mu_{mx})$)
- k_3 : Diffusion rate constant of the main body ($C_2 D_{w,in}^0 K_{in} / (C_2 D_{w,in}^0 + K_{mx} P)$)
- k_4 : Self-diffusion rate constant ($K_w K_{in} / (C_2 D_{w,in}^0 + K_{mx} P) + (C_{01} / \mu_{mx})$)
- C_{01} : Constant only related to the structure of the porous media, which produce relative D'Arcy air permeability
- C_1 : Constant only related to the structure of the porous media, which can produce relative Knudsen air permeability
- C_2 : Constant only related to the structure of the porous media, which is the ratio of the main body diffusion rate to free gas diffusion rate, no dimension
- K_w : Knudsen diffusion coefficient, $K_w = C_1 \sqrt{RT/M_w}$, where M_w is molecular weight of water
- K_{in} : Knudsen diffusion coefficient, $K_{in} = C_1 \sqrt{RT/M_{in}}$, where M_{in} is molecular weight of permanent gas
- K_{mx} : The average Knudsen diffusion coefficient of binary gas mixture, ($y_w K_{in} + y_{in} K_w$)
- $D_{w,in}$: Diffusion coefficient of free gas in binary gas mixture with water vapor and permanent gas
- R : Gas constant (kJ/mole·K)
- M : Molecular weight (kg/kg mole)
- P : Total pressure in the already dried layer (Pa)
- P_w : Partial vapor pressure (Pa)
- P_w^0 : Initial partial vapor pressure (Pa)
- P_{in} : Partial pressure of permanent gas (Pa)
- P_{in}^0 : Initial partial pressure of permanent gas (Pa)
- q : Rate of heat flow (kW/m²)

r : Radius (m)
 t : Time (s)
 T : Temperature (K)
 T^0 : Initial temperature (K)
 T_∞ : Outside temperature (K)
 $T_{int f}$: Interface temperature (K)
 v : Interface velocity (m/s)
 x : Space coordinates through the thickness direction
 y : Space coordinates through the warp direction
 Y_i : The number of moles in the component i in gas phase
 μ_{mx} : The viscosity of binary gas mixture with water vapor and permanent gas in porous already dried layer (kg/m·s)
 ΔH_v : The vaporization heat of adsorbed water (kJ/kg)
 ΔH_s : Latent heat of sublimation of ice (kJ/kg).

Greek Letters

ε : The volume of space in each unit volume of material;
 ρ : Density, kg/m³.

Subscript

i : Components
 In: Permanent gas
 w : Water
 e : Effective value
 I: Dried area
 II: Freezing area
 n : Quadrature component
 x : X direction component
 y : Y direction component.

References

- [1] E.-N. Dragoi, S. Curteanu, and D. Fissore, "Freeze-drying modeling and monitoring using a new neuro-evolutive technique," *Chemical Engineering Science*, vol. 72, pp. 195–204, 2012.
- [2] A. A. Barresi, R. Pisano, V. Rasetto, D. Fissore, and D. L. Marchisio, "Model-based monitoring and control of industrial freeze-drying processes: effect of batch nonuniformity," *Drying Technology*, vol. 28, no. 5, pp. 577–590, 2010.
- [3] M. J. Pikal, S. Cardon, C. Bhugra et al., "The nonsteady state modeling of freeze drying: in-process product temperature and moisture content mapping and pharmaceutical product quality applications," *Pharmaceutical Development and Technology*, vol. 10, no. 1, pp. 17–32, 2005.
- [4] R. Pisano, D. Fissore, S. A. Velardi, and A. A. Barresi, "In-line optimization and control of an industrial freeze-drying process for pharmaceuticals," *Journal of Pharmaceutical Sciences*, vol. 99, no. 11, pp. 4691–4709, 2010.
- [5] N. Harnkarnsujarit, S. Charoenrein, and Y. H. Roos, "Microstructure formation of maltodextrin and sugar matrices in freeze-dried systems," *Carbohydrate Polymers*, vol. 88, no. 2, pp. 734–742, 2012.
- [6] M. Terta, G. Blekas, and A. Paraskevopoulou, "Retention of selected aroma compounds by polysaccharide solutions: a thermodynamic and kinetic approach," *Food Hydrocolloids*, vol. 20, no. 6, pp. 863–871, 2006.

- [7] A. Yongan, "High-efficiency low temperature drying equipment with heat hump," *Journal of Shenyang Architectural and Civil Engineering Institute*, vol. 12, no. 4, pp. 432–435, 1996.
- [8] J. F. Nastaj and K. Witkiewicz, "Mathematical modeling of the primary and secondary vacuum freeze drying of random solids at microwave heating," *International Journal of Heat and Mass Transfer*, vol. 52, no. 21-22, pp. 4796–4806, 2009.
- [9] J. F. Nastaj, K. Witkiewicz, and B. Wilczyńska, "Experimental and simulation studies of primary vacuum freeze-drying process of random solids at microwave heating," *International Communications in Heat and Mass Transfer*, vol. 35, no. 4, pp. 430–438, 2008.
- [10] A. I. Liapis and R. J. Litchfield, "Optimal control of a freeze dryer-I: theoretical development and quasi steady state analysis," *Chemical Engineering Science*, vol. 34, no. 7, pp. 975–981, 1979.
- [11] K. Georgiev, N. Kosturski, S. Margenov, and J. Starý, "On adaptive time stepping for large-scale parabolic problems: computer simulation of heat and mass transfer in vacuum freeze-drying," *Journal of Computational and Applied Mathematics*, vol. 226, no. 2, pp. 268–274, 2009.
- [12] A. I. Liapis and R. J. Litchfield, "Numerical solution of moving boundary transport problems in finite media by orthogonal collocation," *Computers and Chemical Engineering*, vol. 3, no. 1–4, pp. 615–621, 1979.
- [13] M. M. Tang, A. I. Liapis, and J. M. Marchello, "A multi-dimensional model describing the lyophilization of a pharmaceutical product in a vial," in *Proceedings of the 5th International Drying Symposium*, A. S. Mujumdar, Ed., pp. 57–64, Hemisphere Publishing Corporation, New York, NY, USA, 1986.
- [14] M. J. Millman, A. I. Liapis, and J. M. Marchello, "An analysis of the lyophilization process using a sorption-sublimation model and various operation policies," *AIChE Journal*, vol. 31, no. 10, pp. 1594–1604, 1985.
- [15] T. D. Tsvetkov and N. L. Vulchanov, "Toward the mathematical modeling of heat and mass transfer in vacuum freeze-drying. I. Thermodynamic analysis of heat- and mass-transfer processes in capillary porous materials undergoing freeze-drying," *Cryobiology*, vol. 18, no. 2, pp. 155–165, 1981.
- [16] R. B. Evans, G. M. Watson, and E. A. Mason, "Gaseous diffusion in porous media. II. Effect of pressure gradients," *The Journal of Chemical Physics*, vol. 36, no. 7, pp. 1894–1902, 1962.
- [17] A. Hottot, S. Vessot, and J. Andrieu, "Freeze drying of pharmaceuticals in vials: influence of freezing protocol and sample configuration on ice morphology and freeze-dried cake texture," *Chemical Engineering and Processing*, vol. 46, no. 7, pp. 666–674, 2007.
- [18] C. Agnieszka and L. Andrzej, "Rehydration and sorption properties of osmotically pretreated freeze-dried strawberries," *Journal of Food Engineering*, vol. 97, no. 2, pp. 267–274, 2010.
- [19] Z. Qinglian and L. Jianbo, "Contours and iso-surfaces drawing for the finite element method," *Journal of Shenyang Architectural and Civil Engineering University*, vol. 21, no. 3, pp. 220–224, 2005.
- [20] J. Babić, M. J. Cantalejo, and C. Arroqui, "The effects of freeze-drying process parameters on Broiler chicken breast meat," *Food Science and Technology*, vol. 42, no. 8, pp. 1325–1334, 2009.
- [21] K. Georgiev, N. Kosturski, S. Margenov, and J. Starý, "On adaptive time stepping for large-scale parabolic problems: computer simulation of heat and mass transfer in vacuum freeze-drying," *Journal of Computational and Applied Mathematics*, vol. 226, no. 2, pp. 268–274, 2009.
- [22] T. Branger, C. Bobin, M.-G. Iroulart et al., "Comparative study of two drying techniques used in radioactive source preparation: freeze-drying and evaporation using hot dry nitrogen jets," *Applied Radiation and Isotopes*, vol. 66, no. 6-7, pp. 685–690, 2008.
- [23] R. Thuwapanichayanan, S. Prachayawarakorn, J. Kunwisawa, and S. Soponronnarit, "Determination of effective moisture diffusivity and assessment of quality attributes of banana slices during drying," *Food Science and Technology*, vol. 44, no. 6, pp. 1502–1510, 2011.
- [24] S. A. Velardi and A. A. Barresi, "Development of simplified models for the freeze-drying process and investigation of the optimal operating conditions," *Chemical Engineering Research and Design*, vol. 86, no. 1, pp. 9–22, 2008.
- [25] J. Xiang, J. M. Hey, V. Liedtke, and D. Q. Wang, "Investigation of freeze-drying sublimation rates using a freeze-drying microbalance technique," *International Journal of Pharmaceutics*, vol. 279, no. 1-2, pp. 95–105, 2004.
- [26] M. C. Olguín, V. O. Salvadori, R. H. Mascheroni, and D. A. Tarzia, "An analytical solution for the coupled heat and mass transfer during the freezing of high-water content materials," *International Journal of Heat and Mass Transfer*, vol. 51, no. 17-18, pp. 4379–4391, 2008.
- [27] W. Y. Kuu, J. McShane, and J. Wong, "Determination of mass transfer coefficients during freeze drying using modeling and parameter estimation techniques," *International Journal of Pharmaceutics*, vol. 124, no. 2, pp. 241–252, 1995.

- [28] M. Farid and R. Kizilel, "A new approach to the analysis of heat and mass transfer in drying and frying of food products," *Chemical Engineering and Processing*, vol. 48, no. 1, pp. 217–223, 2009.
- [29] F. Rene, E. Wolff, and F. Rodolphe, "Vacuum freeze-drying of a liquid in a vial: determination of heat and mass-transfer coefficients and optimisation of operating pressure," *Chemical Engineering and Processing*, vol. 32, no. 4, pp. 245–251, 1993.
- [30] M. J. Millman, A. I. Liapis, and J. M. Marchello, "Guidelines for the desirable operation of batch freeze dryers during the removed of free water," *Journal of Food Technology*, vol. 19, pp. 725–738, 1984.

Research Article

Nonequilibrium Thermal Dynamic Modeling of Porous Medium Vacuum Drying Process

Zhijun Zhang and Ninghua Kong

School of Mechanical Engineering and Automation, Northeastern University, Shenyang 110004, China

Correspondence should be addressed to Zhijun Zhang, zhjzhang@mail.neu.edu.cn

Received 15 April 2012; Accepted 11 June 2012

Academic Editor: Zhonghua Wu

Copyright © 2012 Z. Zhang and N. Kong. This is an open access article distributed under the Creative Commons Attribution License, which permits unrestricted use, distribution, and reproduction in any medium, provided the original work is properly cited.

Porous medium vacuum drying is a complicated heat and mass transfer process. Based on the theory of heat and mass transfer, a coupled model for the porous medium vacuum drying process is constructed. The model is implemented and solved using COMSOL software. The water evaporation rate is determined using a nonequilibrium method with the rate constant parameter K_r . K_r values of 1, 10, 1000, and 10000 are simulated. The effects of vapor pressures of 1000, 5000, and 9000 Pa; initial moistures of 0.6, 0.5, and 0.4 water saturation; heat temperatures of 323, 333, and 343 K; and intrinsic permeability of 10^{-13} , 10^{-14} , and 10^{-15} m² are studied. The results facilitate a better understanding of the porous medium vacuum drying process.

1. Introduction

Vacuum drying is an excellent drying method for vegetables and fruits, among others. This approach is a low-temperature, nonpolluting method that produces good results. However, vacuum drying requires a complicated device and entails high costs. Scientists and engineers are currently studying vacuum drying equipment that could be used in corn drying [1–3]. However, the corn vacuum drying theory remains unclear. Given that corn is a porous medium, the vacuum drying of corn is a complicated heat and mass transfer process that has been the subject of intensive research [4–7]. All vacuum drying models have to address the water phase change during numerical solving. In one method, the vapor pressure is equal to its equilibrium value [8–11]. Another method is nonequilibrium method [12–16].

Erriguible studied convective and vacuum drying and identified the couple problem of heat and mass transfer between the inner and the outer porous medium [8, 9]. The numerical code applied to the porous medium and the computational fluid dynamics (CFD) Software (FLUENT) was obtained. Murugesan presented the same problem [10].

Perré and Turner used a dual-scale modeling approach to describe the coupling of the drier (large-scale) and the porous medium (macroscale) throughout the drying process [11]. The model was used to investigate the vacuum drying of a softwood board placed in an experimental vacuum chamber heated by two infrared emitters.

Torres et al. proposed a coupled model to describe the vacuum drying of oak wood at the laboratory scale [12, 13]. This model describes the physics of wood-water relations and interactions with a vacuum dryer. The results provided important information on liquid and gas phase transport in wood.

Warning implemented a multiphase porous media model involving heat and mass transfer within a potato chip in a commercial CFD program [14]. The simulations were run at different frying pressures of 1.33, 9.89, 16.7, and 101 kPa. Good agreement between the predicted and literature experimental moisture, oil, and acrylamide content was achieved. Regardless of fryer pressure, the model showed that the core pressure increased and became approximately 40 kPa higher than the surface. The model modified Darcy's law to account for the Klinkenberg effect.

Halder et al. developed an improved multiphase porous media model involving heat and mass transfer with careful consideration given to the selection of input parameters [15, 16]. The nonequilibrium formulation for evaporation, which provides a better description of the physics and is easier to implement in a typical CFD software, is used because it can explicitly express the evaporation rate in terms of the concentration of vapor and temperature. External heat transfer and mass transfer coefficients are estimated to reflect the different frying phases accurately, that is, the nonboiling phase and surface boiling and falling rate stages in the boiling phase.

As noted by Halder et al., water evaporation during frying or during other drying-like processes implemented using an equilibrium formulation may not always occur [14, 15]. The equations resulting from an equilibrium formulation cannot be implemented in any direct manner in the framework of most commercial software. A nonequilibrium formulation provides a better description of the physics and is also easier to implement in software, thus appearing to be the obvious alternative. Additionally, details on the nonequilibrium model have not been discussed thoroughly.

In this paper, heat and mass transfer of porous medium in the vacuum drying process is implemented by using a nonequilibrium method. First, different phase change rates were studied to understand their effect on the drying process. The effects of vapor pressure, initial moisture, heat temperature, and intrinsic permeability on the drying process were then examined.

2. Physical Model

A physical one-dimensional (1D) model that explains the drying process is shown in Figure 1. The bottom of the porous medium is heated by a hot plate. The top of the porous medium is subjected to gas pressure. The height of the porous medium is 1 cm.

3. Mathematical Model

The porous medium consists of a continuous rigid solid phase, an incompressible liquid phase (free water), and a continuous gas phase that is assumed to be a perfect mixture of vapor and dry air, considered as ideal gases. For a mathematical description of the transport

phenomenon in a porous medium, we adopt a continuum approach, wherein macroscopic partial differential equations are achieved through the volume averaging of the microscopic conservation laws. The value of any physical quantity at a point in space is given by its average value on the averaging volume centered at this point.

The moisture movement of the inner porous medium is liquid water and vapor movement; that is, the liquid water could become vapor, and the vapor and liquid water are moved by the pressure gradient.

The compressibility effects of the liquid phase are negligible, and the phase is homogeneous:

$$\bar{\rho}_l = \text{const} \tan t. \quad (3.1)$$

The solid phase is rigid and homogeneous:

$$\bar{\rho}_s = \text{const} \tan t. \quad (3.2)$$

The gaseous phase is considered an ideal gas. This phase ensures that

$$\begin{aligned} \bar{p}_a &= \frac{m_a P_a}{RT}, \\ \bar{p}_v &= \frac{m_v \bar{P}_v}{RT}, \\ \bar{P}_g &= \bar{P}_a + \bar{P}_v, \\ \bar{\rho}_g &= \bar{\rho}_a + \bar{\rho}_v. \end{aligned} \quad (3.3)$$

The assumption of the local thermal equilibrium between the solid, gas, and liquid phases involves

$$\bar{T}_s = \bar{T}_g = \bar{T}_l = \bar{T}. \quad (3.4)$$

Mass conservation equations are written for each component in each phase. Given that the solid phase is rigid, the following is given:

$$\frac{\partial \bar{\rho}_s}{\partial t} = 0. \quad (3.5)$$

The averaged mass conservation of the dry air yields

$$\frac{\partial(\varepsilon \cdot S_g \bar{\rho}_a)}{\partial t} + \nabla \cdot (\bar{\rho}_a \bar{V}_a) = 0. \quad (3.6)$$

For vapor,

$$\frac{\partial(\varepsilon \cdot S_g \bar{\rho}_v)}{\partial t} + \nabla \cdot (\bar{\rho}_v \bar{V}_v) = \dot{I}. \quad (3.7)$$

For free water,

$$\frac{\partial(\varepsilon \cdot S_w \bar{\rho}_l)}{\partial t} + \nabla \cdot (\bar{\rho}_l \bar{V}_l) = -\dot{I}. \quad (3.8)$$

For water, the general equation of mass conservation is obtained from the sum of the conservation equations of vapor (v) and free water (l). The general equation is written as follows:

$$\frac{\partial W}{\partial t} + \nabla \cdot \left\{ \frac{1}{\bar{\rho}_s} (\bar{\rho}_l \bar{V}_l + \bar{\rho}_v \bar{V}_v) \right\} = 0, \quad (3.9)$$

$$W = \frac{\varepsilon \cdot S_w \bar{\rho}_l + \varepsilon \cdot S_g \bar{\rho}_v}{(1 - \varepsilon) \bar{\rho}_s}. \quad (3.10)$$

For the Darcy flow of vapor,

$$\bar{\rho}_v \bar{V}_v = \bar{\rho}_v \bar{V}_g - \bar{\rho}_g D_{\text{eff}} \cdot \nabla \bar{\omega}. \quad (3.11)$$

For the Darcy flow of air,

$$\bar{\rho}_a \bar{V}_a = \bar{\rho}_a \bar{V}_g + \bar{\rho}_g D_{\text{eff}} \cdot \nabla \bar{\omega}, \quad (3.12)$$

where the gas and free water velocity is given by

$$\bar{V}_g = -\frac{k \cdot k_{rg}}{\mu_g} \cdot (\nabla \bar{P}_g - \rho_g \vec{g}), \quad (3.13)$$

$$\bar{V}_l = -\frac{k \cdot k_{rl}}{\mu_l} \cdot (\nabla \bar{P}_l - \rho_l \vec{g}).$$

The effective diffusion coefficient [8] is given by

$$D_{\text{eff}} = DB. \quad (3.14)$$

The vapor fraction in mixed gas is given by

$$\bar{\omega} = \frac{\rho_v}{\rho_g}. \quad (3.15)$$

The pressure moving the free water is given by

$$\bar{P}_l = \bar{P}_g - \bar{P}_c. \quad (3.16)$$

For capillary pressure,

$$\bar{P}_c = 56.75 \times 10^3 (1 - S_l) \exp\left(\frac{1.062}{S_l}\right). \quad (3.17)$$

The saturation of free water and gas is

$$S_g + S_l = 1. \quad (3.18)$$

Free water relative permeability is given by

$$k_{rl} = \begin{cases} \left(\frac{S_l - S_{cr}}{1 - S_{cr}}\right)^3 & S_w > S_{cr} \\ 0 & S_w \leq S_{cr}. \end{cases} \quad (3.19)$$

Gas relative permeability is given by

$$k_{rg} = S_g. \quad (3.20)$$

The water phase change rate is expressed as

$$\dot{I} = K_r \frac{m_v (a_w P_{sat} - P_v) S_g \varepsilon}{RT}. \quad (3.21)$$

Water saturation vapor pressure is given by

$$P_{sat} = \frac{101325}{760} \times 10^{(8.07131 - 1730.63 / (233.426 + (T - 273)))}. \quad (3.22)$$

By considering the hypothesis of the local thermal equilibrium, the energy conservation is reduced to a unique equation:

$$\begin{aligned} \frac{\partial \bar{\rho} \bar{h}}{\partial t} + \nabla \cdot \left\{ (\bar{\rho}_a \bar{V}_a \bar{h}_a + \bar{\rho}_v \bar{V}_v \bar{h}_v + \bar{\rho}_l \bar{V}_l \bar{h}_l - \lambda_e \cdot \nabla \bar{T} - \Delta H \cdot \dot{I}) \right\} &= 0, \\ \lambda_e &= (1 - \varepsilon) \lambda_s + \varepsilon (S_l + S_g (\omega \lambda_v + (1 - \omega) \lambda_a)), \\ \bar{\rho} \bar{h} &= \bar{\rho}_s \bar{h}_s + \varepsilon \cdot S_g \bar{\rho}_a \bar{h}_a + \varepsilon \cdot S_g \bar{\rho}_v \bar{h}_v + \varepsilon \cdot S_l \bar{\rho}_l \bar{h}_l. \end{aligned} \quad (3.23)$$

4. Boundary Condition and Parameters

The air pressure on the external surface at the top of the porous medium is fixed, and the boundary condition for air is given by

$$P_a = P_{av}. \quad (4.1)$$

The boundary condition for vapor at the top of the porous medium is given by

$$P_v = P_{vb}. \quad (4.2)$$

To simulate the vapor pressure of the vacuum drying chamber effect on the drying process, four different vapor pressure boundary values are used.

The boundary condition for free water at the top of the porous medium is

$$n \cdot (-D\nabla S_w) = 0. \quad (4.3)$$

The boundary condition for energy at the top of the porous medium is

$$n \cdot (k\nabla T) = h(T_{amb} - T). \quad (4.4)$$

The boundary condition at the bottom of the porous medium is

$$T = T_h. \quad (4.5)$$

Three different T_h values are used in the simulation.

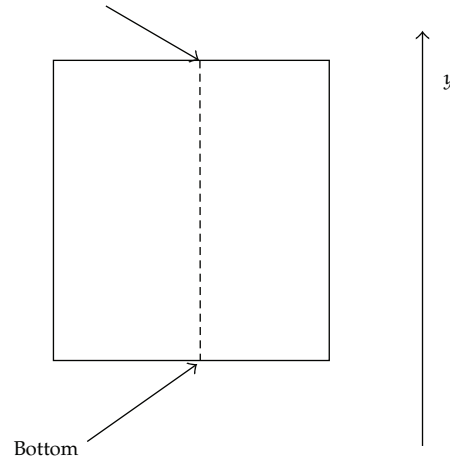
The initial moisture of the porous medium is represented by the liquid water saturation; different initial water saturation values are used. To compare the effects, drying base moisture content was also used, as shown in (3.9). The water phase change rate is studied using four different rate constant parameter values. The modeling parameters are shown in Table 1.

5. Numerical Solution

COMSOL Multiphysics 3.5a was used to solve the set of equations. COMSOL is an advanced software used for modeling and simulating any physical process described by partial derivative equations. The set of equations introduced above was solved using the relative initial and boundary conditions of each. COMSOL offers three possibilities for writing the equations: (1) using a template (Fick's Law, Fourier's Law), (2) using the coefficient form (for mildly nonlinear problems), and (3) using the general form (for most nonlinear problems). Differential equations in the coefficient form were written using an unsymmetric-pattern multifrontal method. We used a direct solver for sparse matrices (UMFPACK), which involves significantly more complicated algorithms than solvers used for dense matrices. The main complication is the need to handle the fill-in in factors L and U efficiently.

Table 1: Parameters used in the simulation process.

Parameter	Symbol	Value	Unit
Rate constant parameter	K_r	1, 10, 1000, 10000	s^{-1}
Intrinsic permeability	k	$10^{-13}, 10^{-14}, 10^{-15}$	m^2
Initial water saturation	S_{l0}	0.6, 0.5, 0.4	
Initial moisture (dry base)	W_0	2.01, 1.68, 1.34	
Vapor pressure of vacuum drying chamber	P_{vb}	1000, 5000, 9000	Pa
Heat temperature	T_h	323, 333, 343	K
Porosity	ε	0.615	
Solid density	ρ_s	476	$kg\ m^{-3}$
Air pressure of vacuum drying chamber	P_{ab}	0.001	Pa
Heat exchange coefficient	h	2.5	$W\ m^{-2}\ K^{-1}$
Air temperature of vacuum drying chamber	T_{amb}	293	K

**Figure 1:** 1D model of porous medium.

A two-dimensional (2D) grid was used to solve the equations using COMSOL Multiphysics 3.5a. Given the symmetry condition setting at the left and the right sides, the 1D model shown in Figure 1 was, in fact, the model that was applied. The mesh consists of 4×100 elements (2D), and time stepping is 1 (0 s to 200 s of solution), 10 (200 s to 100000 s of solution), and 100 (100000 s to 500000 s of solution). Several grid sensitivity tests were conducted to determine the sufficiency of the mesh scheme and to ensure that the results are grid-independent. The maximum element size was established as $1e^{-4}$. A backward differentiation formula was used to solve time-dependent variables. Relative tolerance was set to $1e^{-3}$, whereas absolute tolerance was set to $1e^{-4}$. The simulations were performed using a Lenovo Thinkpad X200 with Intel Core 2 Duo processor with 2.4 GHz processing speed, and 2048 MB of RAM running Windows XP.

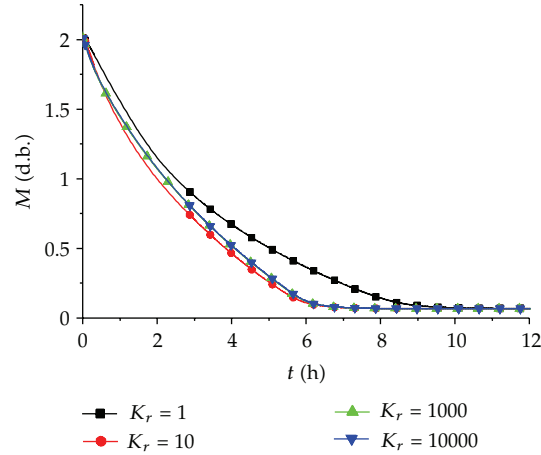


Figure 2: Moisture curves of different K_r values.

6. Results and Discussion

6.1. Effect of Phase Change Rate

The phase change rate of water could not be determined using any method for porous medium drying [14, 15]. The rate constant parameter K_r has a dimension of reciprocal time in which phase change occurs. A large K_r value signifies that phase change occurs within a small time frame. For assumption of equilibrium, either K_r is infinitely large or phase change occurs instantaneously. A very high K_r value, however, makes the convergence of the numerical solution difficult.

In the simulations, K_r is set as 1, 10, 100, 1000, and 10000. The other parameters are $S_{i0} = 0.6$, $k = 10^{-13}$, $P_{vb} = 1000$ Pa, and $T_h = 323$ K. However, when K_r is 100, the numerical solution is not convergent even the time step is reduced and the grid is refined, the reason for which is unknown. The results of the other K_r values are shown in Figures 2 to 8. Figure 2 shows the moisture curves of different K_r values. Moisture M is obviously affected by the K_r value. When K_r is set as 1, the drying process is longer (approximately 9 h). However, when $K_r \geq 10$, the total drying time remains almost the same (approximately 6 h). Under the vacuum conditions, the free water evaporated easily because it was boiling, which resulted in a faster drying rate. For the quick drying process, a higher value ($K_r > 100$) is typically adopted [13].

Figures 3 and 4 show the temperature curves at $y = 5$, 7.5, and 10 mm at different K_r values. The temperature is increased rapidly at the start of drying and is then lowered gradually. As the drying process continues, the temperature is increased slowly. The temperature is rapidly increased when the free water has evaporated. When the drying is nearly finished, the temperature remains unchanged. The end temperatures at the same final position are the same for all K_r values. At $y = 5$ mm, the end temperature is approximately 312 K; at $y = 7.5$ mm, the end temperature is approximately 315 K; and at $y = 10$ mm, the end temperature is approximately 317 K. The simulation results do not coincide with those of the equilibrium method, wherein temperature is increased at the beginning, remained unchanged throughout the process, and then increased slowly until a steady value was obtained [8].

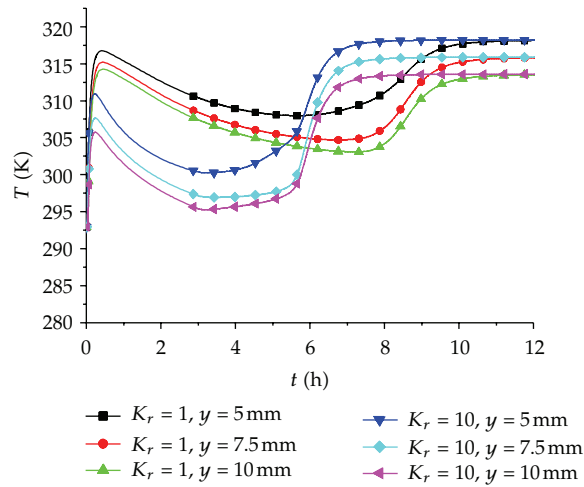


Figure 3: Temperature curve of $K_r = 1$ and 10.

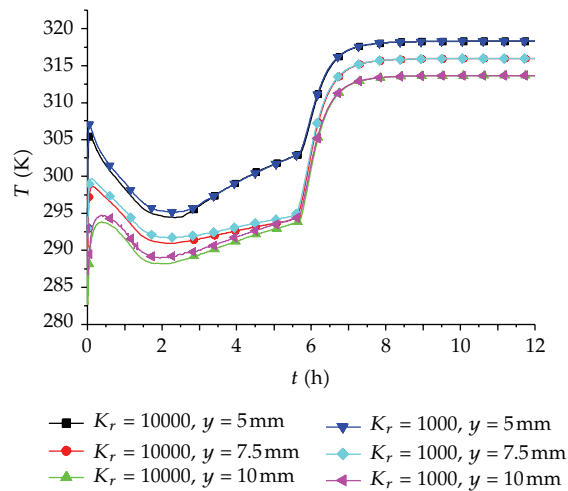


Figure 4: Temperature curve of $K_r = 1000$ and 10000.

The temperature change is near to same as the K_r value increases. That is especially noticeable when comparing $K_r = 1$ with $K_r = 1000$ and 10000. The temperature curve is almost the same for $K_r = 1000$ and 10000.

Figures 5 to 8 show the moisture change curves of different K_r values along the y direction at 0.5, 1, 2, 3, 4, 5, 6, 7, 8, 9, and 10 h. The moisture curve of $K_r = 1$ obviously differs from the curve of $K_r = 10, 1000$, and 10000. Throughout most of the drying time, the moisture of $K_r = 1$ is lower near the heat position ($y = 0$), and the moisture is higher farther away from the heat position ($y = 0.01 \text{ m}$). Until the latter part of the drying process (7 h), the middle section near the top has higher moisture because of the relatively low free water evaporation rate and the relatively large free water movement. Pressure gradient moves the moisture from the bottom to the top. However, the moisture values at $K_r = 10, 1000$, and 10000 are higher in

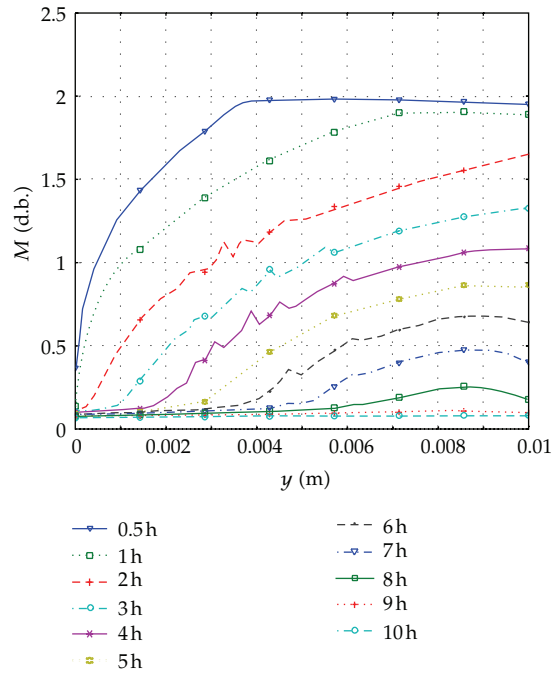


Figure 5: Moisture change at $K_r = 1$.

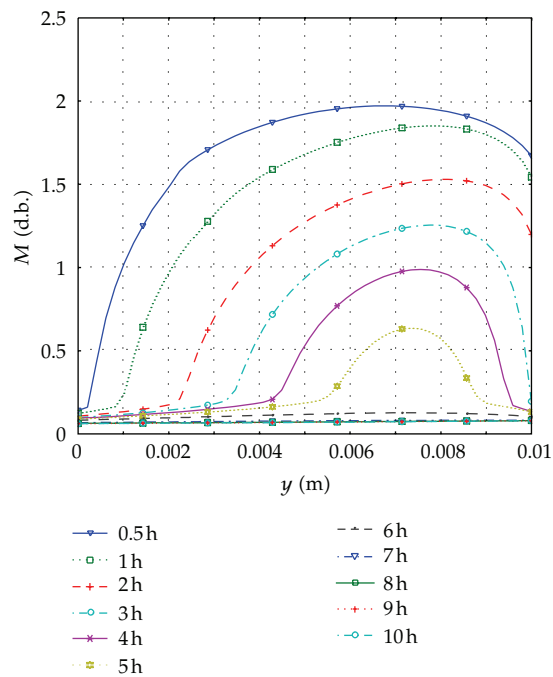


Figure 6: Moisture change at $K_r = 10$.

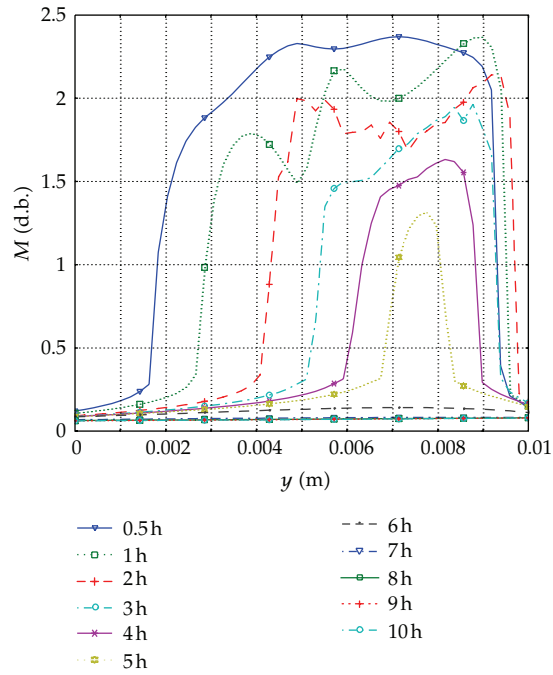


Figure 7: Moisture change at $K_r = 1000$.

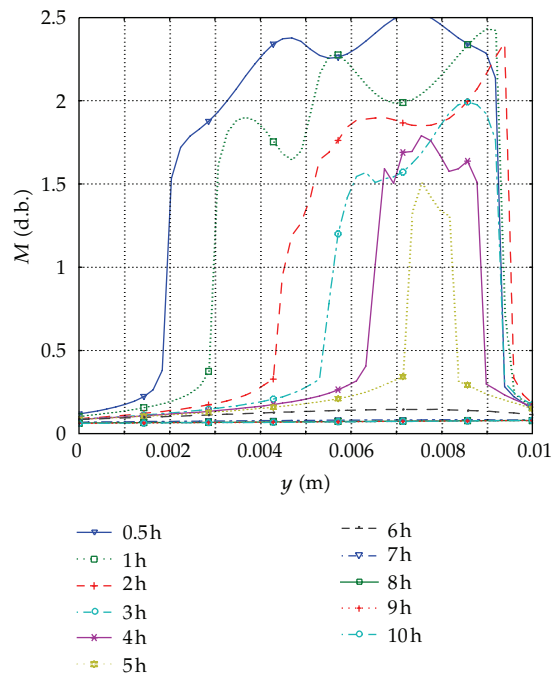


Figure 8: Moisture change at $K_r = 10000$.

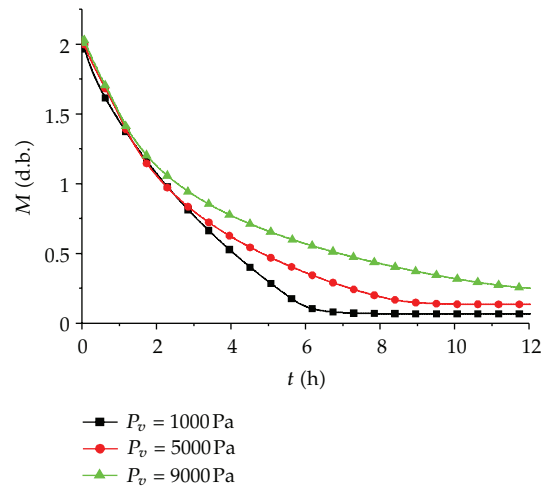


Figure 9: Moisture curves of different P_{vb} .

the middle near the top throughout most of the drying time; the moisture change appears in Figure 6 as a “ Ω ” symbol.

The moisture curves of $K_r = 1000$ and 10000 are almost the same. However, the curves are not as smooth as that of $K_r = 1$ because of the higher free water evaporation rate. This issue could be resolved by reducing the time step in the resolving process. The moisture is greater than the initial moisture at the initial drying time because of the free water movement. As shown in Figures 2 to 8, the simulation results of $K_r = 1000$ and 10000 are almost the same. $K_r = 1000$ is adequate for the quick drying process [14, 15].

6.2. Effect of Vapor Pressure in Vacuum Drying Chamber

The pressure of a vacuum drying chamber, especially vapor pressure, plays an important role in the vacuum drying process and is also linked to the drying cost. The moisture curves of $P_{vb} = 1000$, 5000 , and 9000 Pa are shown in Figure 9. The other simulation parameters are $S_{l0} = 0.6$, $k = 10^{-13}$, $K_r = 1000$, and $T_h = 323$ K. The vapor pressure has a greater effect on the drying process; a lower vapor pressure results in greater pressure degradation. The drying times are approximately 6, 8, and 12 h. The movements of free water and vapor, as well as the free water evaporation rate, are quicker, as given by (3.13), and (3.21), respectively.

The different vapor pressure effects on the temperature curve are shown in Figure 10. Compared with the temperature curve at $P_{vb} = 1000$ Pa, no significant change was observed in the temperature curve at $P_{vb} = 5000$ and 9000 Pa. The temperature is increased at the start of drying, then it is lowered which is insignificant, especially at $P_{vb} = 9000$ Pa. The moisture changes at $P_{vb} = 5000$ and 9000 Pa are shown in Figures 11 and 12, respectively, as compared with the moisture change at $P_{vb} = 1000$ Pa (Figure 7).

The curve was smoother because the increasing vapor pressure lowers the water evaporation rate, as shown in (3.21). For $P_{vb} = 9000$ Pa in particular, the maximum moisture value appears at $y = 0.01$ m in the drying process. The moisture curve does not appear as the “ Ω ” symbol.

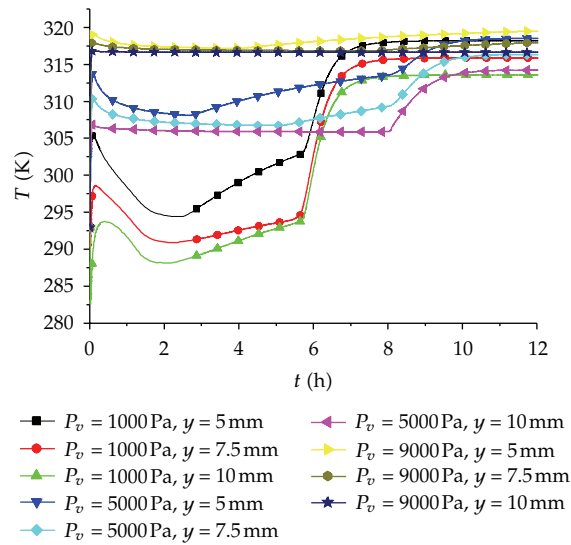


Figure 10: Temperature curves of different P_{vb} .

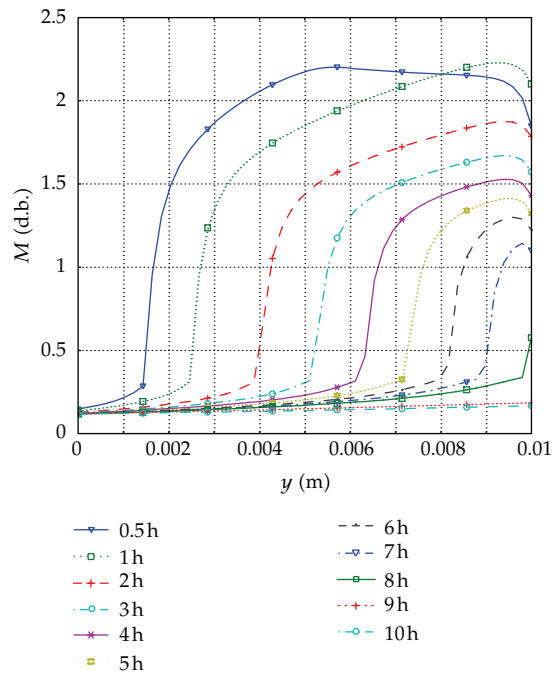


Figure 11: Moisture change of $P_{vb} = 5000$ Pa.

6.3. Effect of Initial Moisture Content

The effect of initial moisture content on the moisture curve is shown in Figure 13. To compare the results, moisture is represented by the moisture ratio M/M_0 . The drying times are 4.5,

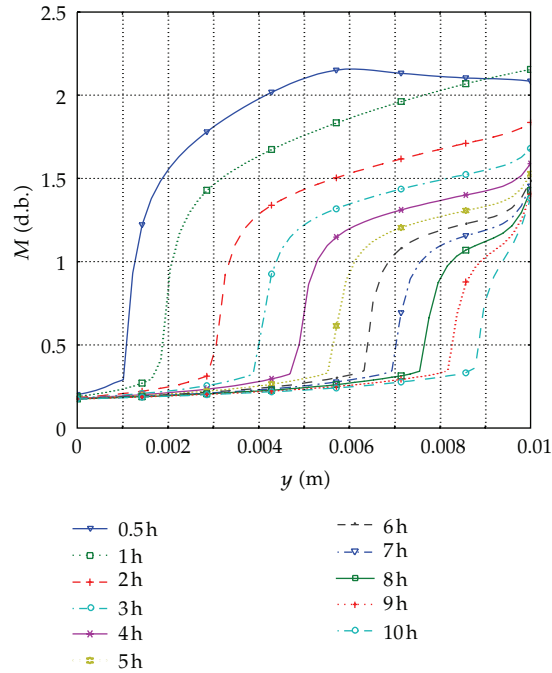


Figure 12: Moisture change of $P_{vb} = 9000$ Pa.

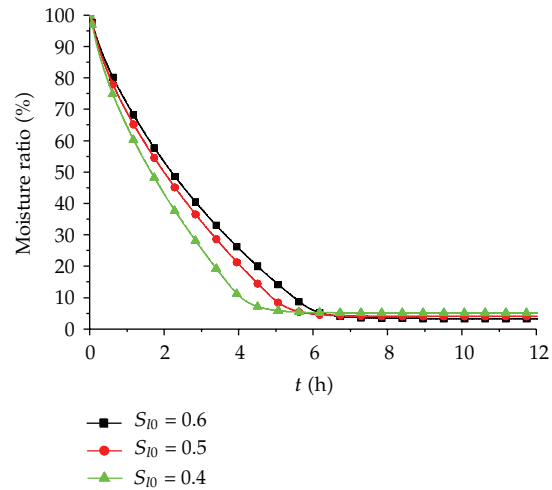


Figure 13: Moisture curves at different S_{10} .

5.5, and 6 h, respectively, for the initial $S_{10} = 0.6, 0.5,$ and 0.4 . The other parameters are $K_r = 1000, k = 10^{-13}, P_{vb} = 1000$ Pa, and $T_h = 323$ K.

The temperature curve is shown in Figure 14. The temperature was obviously affected by the initial moisture, especially on the surface of the porous medium, at $y = 0.01$ m. Higher initial moisture resulted in lower temperature during the drying process.

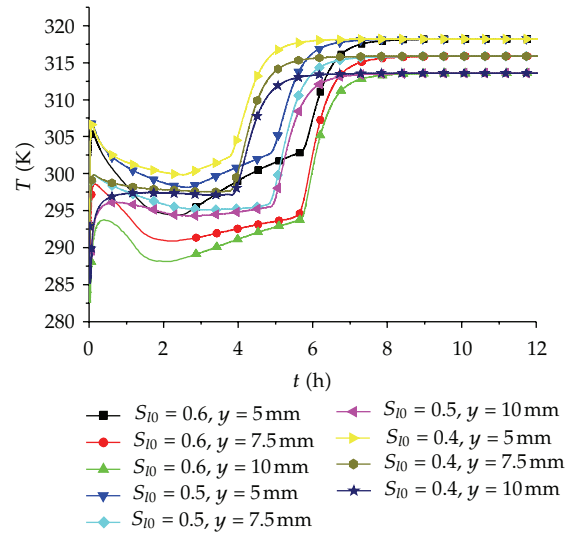


Figure 14: Temperature curves at different S_{10} .

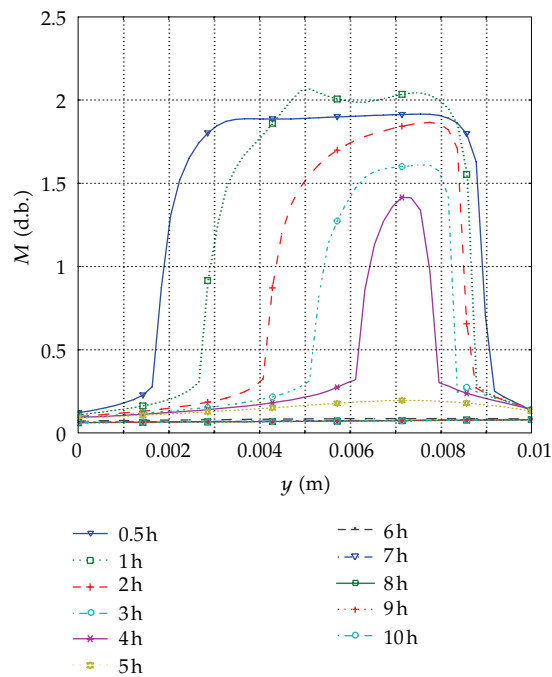


Figure 15: Moisture change at $S_{10} = 0.5$.

The moisture change is shown in Figures 15 and 16 for initial moisture $S_{10} = 0.5$ and 0.4 , respectively, as compared with $S_{10} = 0.6$ (in Figure 7). Except for the value, the changes are similar.

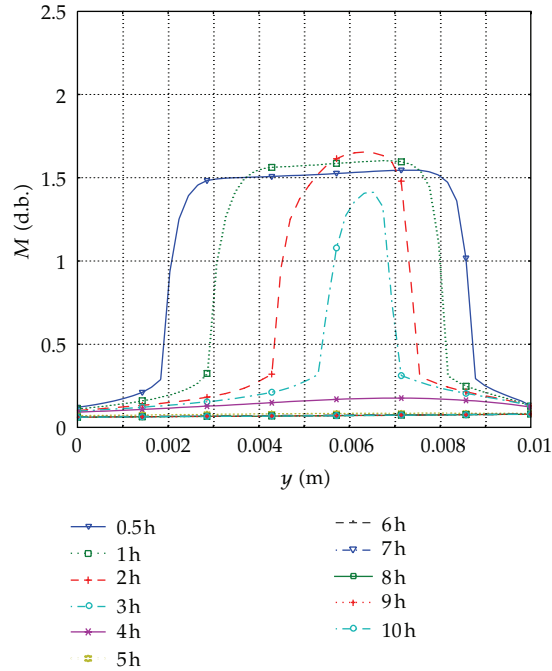


Figure 16: Moisture change at $S_{l0} = 0.4$.

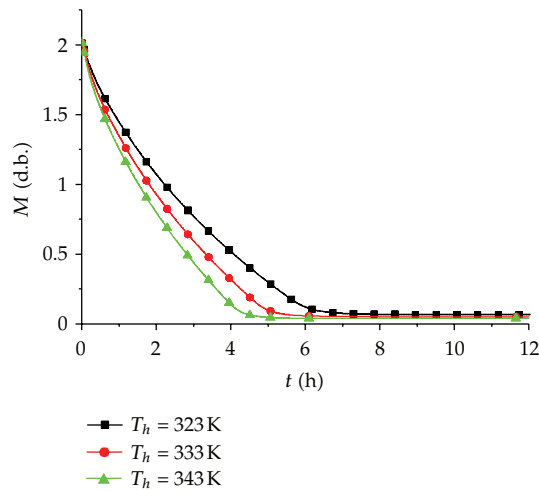


Figure 17: Moisture curves at different T_h .

6.4. Effect of Heat Temperature

The effect of heat temperature on moisture is shown in Figure 17. The drying end times are 6, 5, and 4.5 h, respectively, for the heat temperature $T_h = 323, 333,$ and 343 K. The other parameters are $S_{l0} = 0.6, k = 10^{-13}, K_r = 1000,$ and $P_v = 1000$ Pa. The temperature changes at different points were similar except for the value, as shown in Figure 18. A similar result

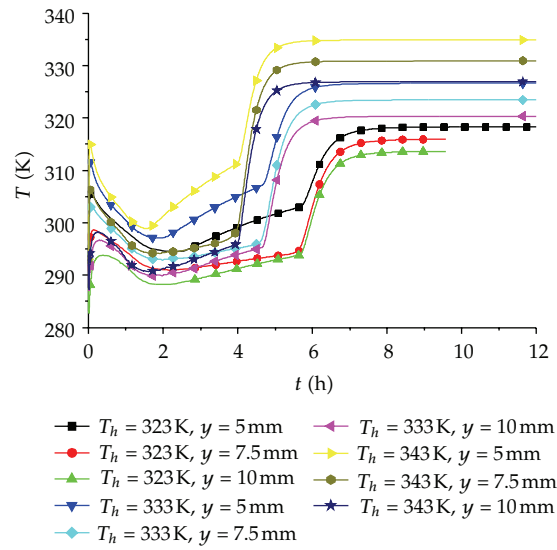


Figure 18: Temperature curves at different T_h .

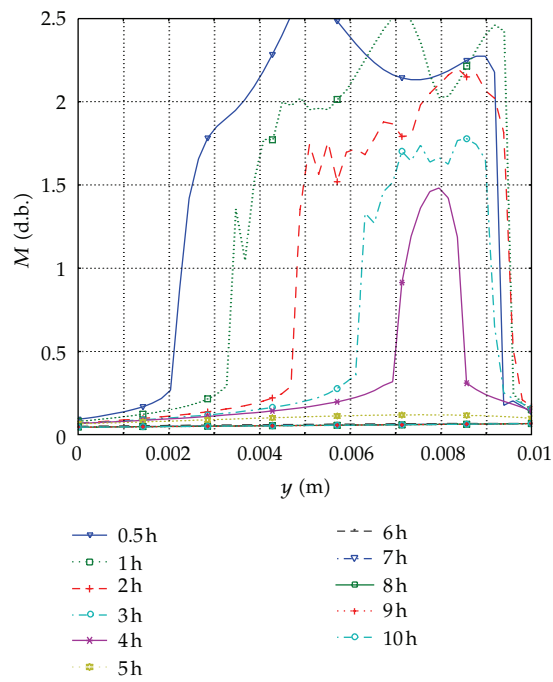


Figure 19: Temperature curve at $T_h = 333\text{K}$.

was found for the moisture changes at different times in Figures 19 and 20 compared with Figure 7.

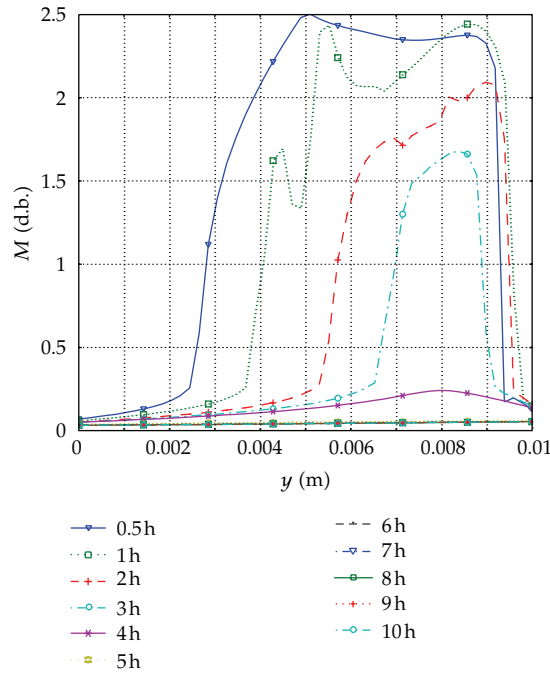


Figure 20: Temperature curve at $T_h = 343$ K.

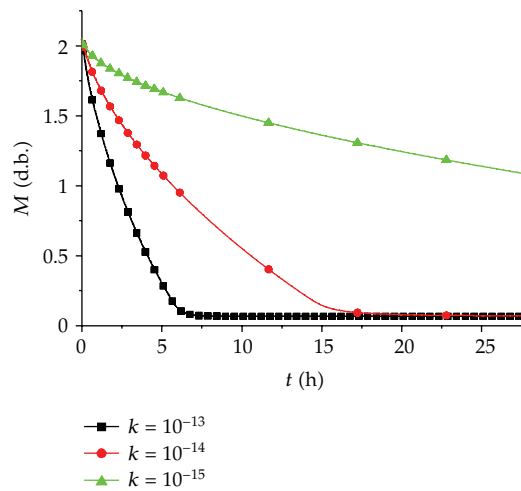


Figure 21: Moisture curves of different K .

6.5. Effect of Intrinsic Permeability

Intrinsic permeability of porous medium is an inherent property and cannot be changed, and measuring it is difficult. Figures 21 and 22 show the moisture and temperature curves at different permeabilities $k = 10^{-13}$, 10^{-14} , and 10^{-15} . Intrinsic permeability has a greater effect because the transfer of free water and vapor is affected by (3.13). The drying time became evidently longer as the intrinsic permeability was reduced because the moisture movement

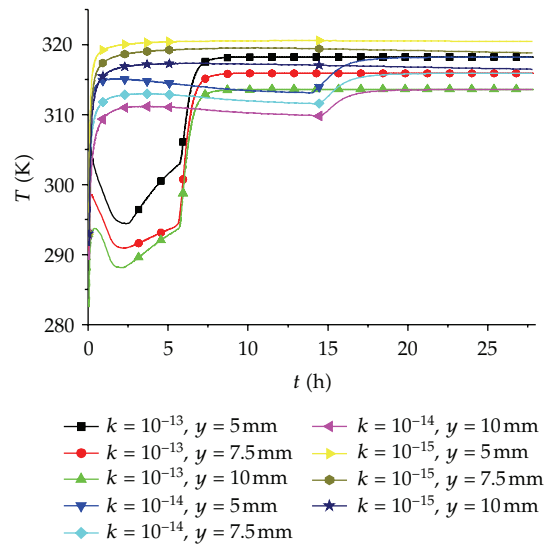


Figure 22: Temperature curves of different k .

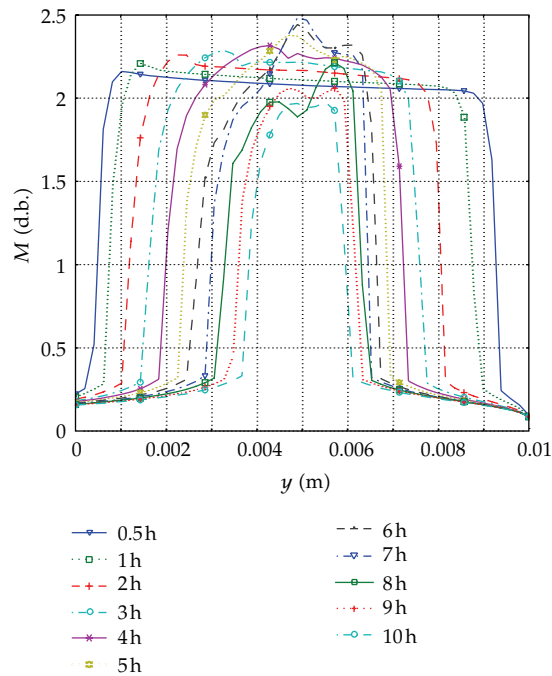


Figure 23: Temperature curves at $k = 10^{-14}$.

velocity was lowered at the same pressure gradient. The temperature is increased because the mass transfer rate is lower.

The effect of intrinsic permeability on moisture change at different time is shown in Figures 23 and 24. The moisture in the middle of the porous medium was not lowered quickly, even at the drying end time for $k = 10^{-14}$ (Figure 23) compared with $k = 10^{-13}$ (Figure 7).

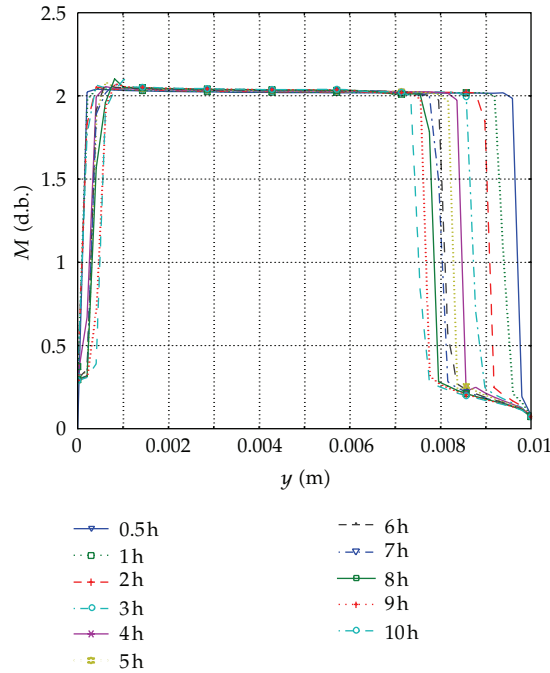


Figure 24: Temperature curves at $k = 10^{-15}$.

7. Conclusion

A coupled model of porous medium vacuum drying based on the theory of heat and mass transfer was implemented in this paper. The model was implemented and solved using COMSOL. The temperature increased quickly at the start of drying and then lowered gradually. As the drying process continued, the temperature increased slowly. In the absence of free water, temperature increased rapidly. As the drying process concluded, the temperature remained unchanged. The water evaporation rate could not be obtained during the porous medium vacuum drying process. The rate constant parameter is essential to the nonequilibrium method. When $K_r \geq 1000$, the simulation of the drying process was not evidently affected. Vapor pressure and heat transfer affected the transfer of mass. A similar effect was found in the initial moisture and the heat temperature. Intrinsic permeability had a greater effect on the drying process.

Nomenclature

- B : Diagonal tensor
- D : Diffusivity ($\text{m}^2 \text{s}^{-1}$)
- D_{eff} : Diffusion tensor ($\text{m}^2 \text{s}^{-1}$)
- g : Gravity vector (m s^{-2})
- h : Intrinsic averaged enthalpy (J kg^{-1})
- I : Water phase rate ($\text{kg s}^{-1} \text{m}^{-3}$)
- k : Intrinsic permeability (m^2)
- k_r : Relative permeability

m : Mass (kg)
 n : Outer unit normal to the product
 P : Pressure (Pa)
 P_c : Capillary pressure (Pa)
 R : Universal Gas constant ($\text{J kmol}^{-1} \text{K}^{-1}$)
 S : Saturation
 t : Time (s)
 T : Temperature (K)
 W : Moisture content (in dry basis).

Greek Letters

ΔH : Latent of phase change (J kg^{-1})
 λ_{ef} : Effective thermal conductivity tensor ($\text{W m}^{-1} \text{K}^{-1}$)
 μ : Viscosity ($\text{kg m}^{-1} \text{s}^{-1}$)
 ρ : Density (kg m^{-3})
 ω : Vapor fraction.

Subscripts

a : Dry air
 g : Gas
 l : Liquid
 s : Solid
 v : Vapor
 sat : Vapor saturation.

Mathematical Operators

Δ : Gradient operator
 $\nabla \cdot$: Divergence operator.

Acknowledgment

This research was supported by the National Natural Science Foundation of China (Grants no. 31000665, no. 51176027).

References

- [1] C. H. Xu, Z. J. Zhang, S. W. Zhang, and X. He, "Probe into the structure of tower continuous vacuum dryer," in *Proceedings of the 5th Asia-Pacific Drying Conference (ADC '07)*, pp. 1261–1267, August 2007.
- [2] Z. J. Zhang, C. H. Xu, S. W. Zhang, and X. He, "The study of corn low temperature continuous tower type vacuum dryer," in *Proceedings of the 5th Asia-Pacific Drying Conference (ADC '07)*, pp. 330–337, August 2007.

- [3] Z. Zhang, C. Xu, S. Zhang, and L. Zhao, "Computer simulation of flow field in tower continuous vacuum dryer," in *Proceedings of the International Conference on Computer Science and Information Technology (ICCSIT '08)*, pp. 534–538, September 2008.
- [4] Y. Ichikawa and A. P. S. Selvadurai, *Transport Phenomena in Porous Media, Aspects of Micro/Macro Behaviour*, Springer, 2012.
- [5] A. K. Haghi, "Transport phenomena in porous media: a review," *Theoretical Foundations of Chemical Engineering*, vol. 40, no. 1, pp. 14–26, 2006.
- [6] S. J. Kowalski, *Drying of Porous Materials*, Springer, 2007.
- [7] J. Bear and Y. Bachmat, *Introduction To Modeling of Transport Phenomena in Porous Media*, Springer, 1990.
- [8] A. Erriguible, P. Bernada, F. Couture, and M. A. Roques, "Simulation of vacuum drying by coupling models," *Chemical Engineering and Processing: Process Intensification*, vol. 46, no. 12, pp. 1274–1285, 2007.
- [9] A. Erriguible, P. Bernada, F. Couture, and M. A. Roques, "Modeling of heat and mass transfer at the boundary between a porous medium and its surroundings," *Drying Technology*, vol. 23, no. 3, pp. 455–472, 2005.
- [10] K. Murugesan, H. N. Suresh, K. N. Seetharamu, P. A. Aswatha Narayana, and T. Sundararajan, "A theoretical model of brick drying as a conjugate problem," *International Journal of Heat and Mass Transfer*, vol. 44, no. 21, pp. 4075–4086, 2001.
- [11] P. Perré and I. W. Turner, "A dual-scale model for describing drier and porous medium interactions," *AIChE Journal*, vol. 52, no. 9, pp. 3109–3117, 2006.
- [12] S. S. Torres, W. Jomaa, J.-R. Puiggali, and S. Avramidis, "Multiphysics modeling of vacuum drying of wood," *Applied Mathematical Modelling. Simulation and Computation for Engineering and Environmental Systems*, vol. 35, no. 10, pp. 5006–5016, 2011.
- [13] S. S. Torres, J. R. Ramírez, and L. L. Méndez-Lagunas, "Modeling plain vacuum drying by considering a dynamic capillary pressure," *Chemical and Biochemical Engineering Quarterly*, vol. 25, no. 3, pp. 327–334, 2011.
- [14] A. Warning, A. Dhall, D. Mitrea, and A. K. Datta, "Porous media based model for deep-fat vacuum frying potato chips," *Journal of Food Engineering*, vol. 110, no. 3, pp. 428–440, 2012.
- [15] A. Halder, A. Dhall, and A. K. Datta, "An improved, easily implementable, porous media based model for deep-fat frying. Part I: model development and input parameters," *Food and Bioprocess Processing*, vol. 85, no. 3, pp. 209–219, 2007.
- [16] A. Halder, A. Dhall, and A. K. Datta, "An improved, easily implementable, porous media based model for deep-fat frying. Part II: results, validation and sensitivity analysis," *Food and Bioprocess Processing*, vol. 85, no. 3, pp. 220–230, 2007.

Research Article

Distribution of Vapor Pressure in the Vacuum Freeze-Drying Equipment

Shiwei Zhang¹ and Jun Liu²

¹ School of Mechanical Engineering and Automation, Northeastern University, Shenyang 110004, China

² Normal School of Shenyang University, Shenyang 110015, China

Correspondence should be addressed to Jun Liu, lilizhao0214@163.com

Received 13 April 2012; Accepted 14 May 2012

Academic Editor: Zhijun Zhang

Copyright © 2012 S. Zhang and J. Liu. This is an open access article distributed under the Creative Commons Attribution License, which permits unrestricted use, distribution, and reproduction in any medium, provided the original work is properly cited.

In the big vacuum freeze-drying equipment, the drying rate of materials is uneven at different positions. This phenomenon can be explained by the uneven distribution of vapor pressure in chamber during the freeze-drying process. In this paper, a mathematical model is developed to describe the vapor flow in the passageways either between material plates and in the channel between plate groups. The distribution of vapor pressure along flow passageway is given. Two characteristic factors of passageways are defined to express the effects of structural and process parameters on vapor pressure distribution. The affecting factors and their actions are quantitatively discussed in detail. Two examples are calculated and analyzed. The analysis method and the conclusions are useful to estimate the difference of material drying rate at different parts in equipment and to direct the choice of structural and process parameters.

1. Introduction

Generally speaking, the food vacuum freeze-drying equipments of which the freeze-drying area is equivalent to or larger than 50 m² are classified as big vacuum freeze-drying equipments [1]. In this type of vacuum freeze-drying equipment, there always exists a phenomenon that the drying rates of materials are uneven at different positions [2]. The reason is commonly charged upon the uneven temperature distribution of material plate [3, 4]. But, the uneven distribution of vapor pressure in vacuum chamber is usually ignored. In fact, the big vacuum freeze-drying equipment always adopts the form of multilayer of big area material plates (shelves) in order to improve the production efficiency and output. And in order to enhance the volume utilization rate of the vacuum chamber, the space between material plates is relatively narrow, and the evacuating port of the vacuum chamber is always on one side of it. All these structural characteristics accordingly lead to the result that

a flexural, long, and narrow flow transfer passageway is formed from the evaporating surfaces of the materials on the plates to the evacuating port of the vacuum chamber and can produce a flow resistance that cannot be ignored. And in the big vacuum freeze-drying equipment the water vapor flow in the sublimating drying stage is rather large, so in the long and narrow passageway there is a significant water vapor pressure difference, and this finally leads to the result that the drying rate of the materials is different on different plates or even in different positions of the same plate in the big vacuum freeze-drying equipment.

Analyzing the distribution of vapor pressure in the big vacuum freeze-drying equipment during the process of vacuum freeze-drying is significant to the correct evaluation of the inhomogeneity of the drying rate and its reduction. The former research on the mass transfer of vapor in the freeze-drying equipment mostly focused on the diffusion process and average drying rate in the materials to be dried [5–7]. But there is less study on the process of the vapor flowing from the surfaces of the materials to the evacuating port of the freeze-drying chamber and the difference of the drying rate in different parts of the materials caused by flowing resistance. This paper develops a mathematic model which describes the flow of the vapor outside the materials in the freeze-drying equipment. The distribution of vapor pressure and the relationship of parameters of each influencing factor are determined. And it also puts forward a quantitative analysis method of drying rate in different positions of the material and the theoretical designing basis of the key structure and processing parameter of the freeze-drying equipment.

2. Structure and Simplified Model

As shown in Figure 1, the material plates and pallets in the big freeze-drying equipment are usually arranged as the form of multilayer matrix, several or more than ten layers vertically aligned to form a group. There is an equidistant passageway between each two plates. One group, two groups or even more groups are arranged in parallel in the vacuum chamber. On both sides of each group and between two groups, there is an evacuating channel. The evacuating port of the vacuum chamber is often on the back of it opposite to the evacuating channels between groups (position a in Figure 1) or on the top or the bottom (position b or b' in Figure 1). It also can be on the lateral side of the chamber (position d and d', or position c in Figure 1). This form can have two evacuating ports.

In the freeze-drying process, the vapor sublimated from the material firstly flows to the evacuating channel between groups through the passageway along the plates, and then flows to the evacuating port along the evacuating channel. Obviously, in the same plate, the vapor sublimated from the material close to the evacuating channel can easily enter the evacuating channel between groups. But because the vapor sublimated from the material in the center of the plate is far from the evacuating channel, not only its transfer distance is long, but also it would merge the vapor sublimated from the material passing by and then flow to the evacuating channel together therefore, the flow resistance is bigger; and this results in that the vapor pressure component in the center of the passageway along the plate is obviously higher than that on the edge of the plate. Similarly, the vapor entering into the evacuating channel would also merge the one flowed out from other plates and then flow together to the evacuating port of the vacuum chamber. And this results in the uneven distribution of vapor pressure in the channel between plate groups. The final result is that the vapor pressure on the edge of the plate close to the evacuating port is the lowest where the material dries quickly, while the vapor pressure in the central of the plate far from the evacuating port is the highest

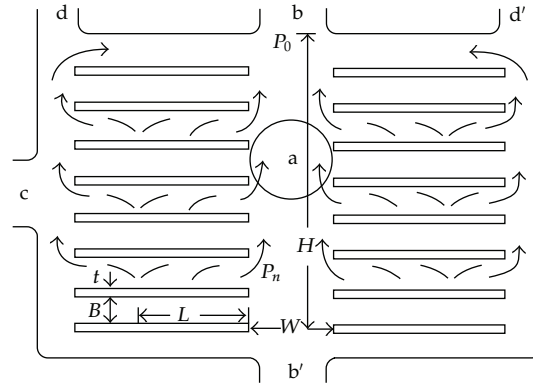


Figure 1: Structure sketch map of multilayer matrix in big-scale freezing equipment.

where the material dries slowly. This is just the significant reason for the uneven distribution of the drying rate of the material in the big vacuum freeze-drying equipment.

In this paper, a mathematic model is firstly developed for calculating the vapor flow and the pressure distribution in the unilateral passageway between plates in order to discover how the equipment's structure and process parameters affect the distribution of vapor pressure. And then the result is extended to the evacuating channel between plate groups and a method is consequently put forward to analyze the distribution of vapor pressure in the whole freeze-drying equipment.

The simplified model of the vapor flow in the unilateral passageway between plates is shown in Figure 2. The coordinate axis X is established along the midline of the width of the passageway, taking the midpoint of the plate as original point, that is, the effective length L of the passageway equals to half of the width of the plate. When the evacuating channels on both sides of the plate are largely different, the original point should be at the demarcation point where the vapor flows towards two sides, respectively. As to the plate which has the evacuating channel on one side only while its other side is closed, the original point should be on the closed termination and the effective length L of the passageway should be the full width of plate. The coordinate axis Y is established along the height direction of the passageway. The bottom of the upper plate is in the position where $Y = B/2$. The upper surface of material on this plate is in the position where $Y = -B/2$, and the vapor sublimates from this surface to the passageway between plates. The length direction of plate vertical to the XOY plane is regarded as to be infinite, so only the unit length of the plate is studied.

3. Hypothesis and Mathematical Equations

In order to simplify the calculation, the following hypotheses are made:

- (1) in the whole passageway, the vapor sublimates homogeneously from the surface of the material with constant rate. It is not influenced by the distribution of vapor pressure. The outgassing rate G_m of the material's surface can be calculated through the total dehydration quantity for some time in the freeze-drying process divided by the area of plate and time;

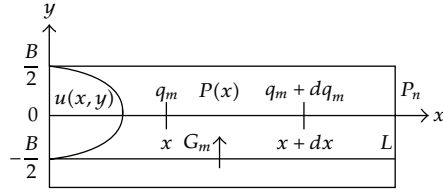


Figure 2: Simplified model of the vapor flow in the unilateral passageway between plates.

- (2) both the influence of the permanent gas in the freezing chamber and the flow of vapor along the Y direction in the passageway are ignored. Attention is only focused on the one dimensional flow along the X direction and it is supposed that the flow is steady lamellar flow and the distribution of its flow velocity can be calculated according to the Poiseuille's flow between flat planes;
- (3) the relationship between the vapor density and the pressure obeys to the perfect gas equation.

Some parameters and their units are defined as follows: B is the height of passageway between plates, m; L is the unilateral length of the passageway, m; u is the flow velocity of vapor, m/s; μ is the kinematical viscosity of vapor, Pa·s; $P(x)$ is the vapor pressure somewhere in the passageway between plates, Pa; q_m is the mass flow through the passageway section, kg/s; G_m is the outgassing rate of the material's surface, kg/(m²s); M is the molar mass of the vapor, 0.018 kg/mol; R is the universal gas constant, 8.3145 J/(mol·K); T is the Kelvin temperature of vapor, K; P_n is the vapor pressure at the outlet of the passageway, Pa.

The mathematical equation which describes the vapor flow in the passageway between plates is as follows: distribution of the vapor flow velocity is

$$u(x, y) = -\frac{1}{2\mu} \cdot \frac{dp}{dx} \cdot \left[\left(\frac{B}{2} \right)^2 - y^2 \right]. \quad (3.1)$$

The mass flow through any passageway section X is

$$q_m(x) = \int_{-B/2}^{B/2} \rho u(x, y) \cdot dy = -\frac{MB^3}{12\mu RT} \cdot p \cdot \frac{dp}{dx}. \quad (3.2)$$

In the above equation, the perfect gas equation has been used as

$$\rho = \frac{pM}{RT}. \quad (3.3)$$

Considering the law of conservation of mass, the mass increment in the segment $x \sim x + dx$ is

$$dq_m = -\frac{MB^3}{12\mu RT} d\left(p \frac{dp}{dx}\right) = G_m \cdot dx \quad (3.4)$$

Accordingly, the control equation can be obtained which describes the distribution of vapor pressure

$$\frac{d^2}{dx^2}(p^2) = -\frac{24\mu RTG_m}{MB^3}. \quad (3.5)$$

Using the terminal condition

$$x = 0, \quad \frac{dp}{dx} = 0, \quad x = L, \quad p = p_n, \quad (3.6)$$

there will be

$$p(x) = p_n \sqrt{1 + \alpha - \alpha \left(\frac{x}{L}\right)^2}, \quad (3.7)$$

where, the characteristic coefficient of the passageway α is defined as

$$\alpha = \frac{12\mu RTG_m \cdot L^2}{MB^3 p_n^2}. \quad (3.8)$$

And the mass flows either through any passage section x and at the outlet of the passageway where $x = L$ are respectively obtained as

$$q_m(x) = G_m \cdot x, \quad q_m(L) = G_m \cdot L. \quad (3.9)$$

The analytical method and the calculated result above can be extended to the calculation of the pressure distribution in the evacuating channel between plate groups. Referring to the mark symbol in Figure 1, the width of the evacuating channel between plate groups W is substituted for the width of the passageway between plates B . The average distance H from the farthest plate to the evacuating port is substituted for the unilateral length L of the passageway between plates. The coordinate axis z is established to express the distance from a certain plate to the farthest plate. The total outgassing quantity of each plate at its outlet $G_m L$ is uniformly spread in the width $B + t$ of space between plates. And it is considered that the outgassing appears on both sides of the evacuating channel between groups. Then, the outgassing rate G_z corresponding to the evacuating channel between groups is

$$G_z = \frac{2G_m L}{B + t}. \quad (3.10)$$

If P_0 is defined to express the vapor pressure at the terminal end of the evacuating channel between groups, that is, at the evacuating port of the vacuum chamber, then the formula

calculating the distribution of vapor pressure $p_n(z)$ in the evacuating channel between groups is

$$p_n(z) = p_0 \sqrt{1 + \beta - \beta \left(\frac{z}{H}\right)^2}, \quad (3.11)$$

where, the characteristic coefficient of the evacuating channel between groups β is defined as

$$\beta = \frac{12\mu RTG_z \cdot H^2}{MW^3 p_0^2}. \quad (3.12)$$

4. Discussion about the Calculating Results

- (1) Using the above result, the vapor pressure at any appointed position in the vacuum freeze-drying equipment can be conveniently calculated. Firstly, P_0 must be estimated, which is the lowest vapor pressure at the evacuating port and is produced by the vacuum system and the ice condenser. Then, based on the related structural parameters of freeze-dryer such as H, W, B, t , and L , besides the processing parameters G_m and P_0 , the vapor pressure P_n at the outlets of the passageway in any plates can be calculated by formulae (3.10), (3.11), and (3.12). At last, the vapor pressure $P(x)$ in any position of the passageway of the plate can be worked out by formulae (3.7) and (3.8). For example, in general case, the central part ($x = 0$) of the farthest plate ($z = 0$) is the place where vapor pressure is the highest in the vacuum chamber, and the value of maximum vapor pressure is

$$p_{\max} = p_0 \sqrt{1 + \beta} \sqrt{1 + \alpha}. \quad (4.1)$$

- (2) In the passageway of a certain plate, the maximal pressure difference between the central part and the edge part is

$$\Delta p = p(0) - p_n = p_n (\sqrt{1 + \alpha} - 1). \quad (4.2)$$

The deviation ratio of maximal pressure in the passageway of this plate is defined as

$$\delta = \frac{\Delta p}{p_n} = \sqrt{1 + \alpha} - 1. \quad (4.3)$$

The relation curve of δ - α is shown in Figure 3. From the figure, it is found that if you want the deviation ratio of pressure δ to be small, correspondingly the characteristic coefficient of the passageway between plates α should also be small. Similarly, the deviation ratio of maximal pressure in the evacuating channel between groups can be defined. Its relationship to the characteristic coefficient of the evacuating channel

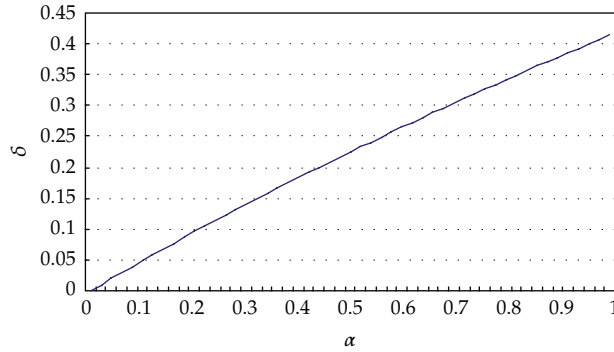


Figure 3: The relation of the deviation ratio of maximal pressure to the characteristic coefficient.

between groups is the same to formula (4.3). The deviation ratio of maximal pressure for the whole vacuum chamber should be

$$\delta_{\max} = \frac{p_{\max} - p_0}{p_0} = \sqrt{1 + \alpha} \sqrt{1 + \beta} - 1. \quad (4.4)$$

If you want δ_{\max} to be less than a certain value, you have to control the value of α and β simultaneously.

- (3) The distribution of vapor pressure along the passageway of a certain plate is only related to the value of α . The pressure variation $p(x)/p_n \sim x/L$ is shown in Figure 4. From the definition formula (3.8) of α , it is known that the influencing factors include not only the geometrical structure parameters of passageway B and L , but also the processing parameters G_m and P_n . The difference of the power of each parameter indicates that they have different effects on the vapor pressure distribution. The relationship of the characteristic parameter α to the length L and height B of the passageway is expressed as $\alpha \propto L^2/B^3$. This does not obey to the proportional similarity criterion. For example, if both L and B are reduced by one time, the value of α will increase one time but not keep invariant. Therefore, in order to reduce the value of α , that will reduce the pressure difference between the central part and the edge part of the passageway, appropriately increasing the height B is more effective than reducing the length L . The relationship of the characteristic parameter α to the processing parameters G_m and P_n is $\alpha \propto G_m/p_n^2$. It indicates that when the outgassing quantity of the material surface G_m increases, the α will increase with direct proportion, and the pressure difference between the central part and the edge part of the passageway will also increase. On the other hand, when the outlet pressure P_n decreases, though the characteristic coefficient α and the relative deviation ratio δ is increasing sharply, the maximal pressure difference Δp is not increasing quickly and its value will not exceed $\Delta p_{\max} = p_n \sqrt{\alpha}$.
- (4) Similarly, the distribution of vapor pressure along the evacuating channel between groups is only related to the value of β . The pressure variation $p_n/p_0 \sim z/H$ is also shown in Figure 4. Its influencing factors contain geometrical structure parameters and processing parameters. The restrictive relationship among them and their relation to β are the same as the results above.

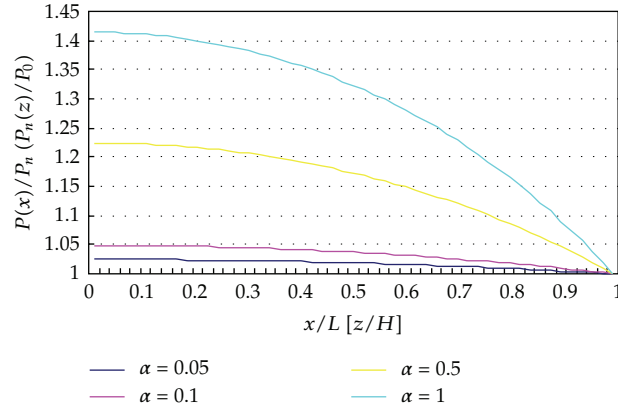


Figure 4: Vapor pressure distribution in the passageway channel between plates.

- (5) Using the calculated result of vapor pressure distribution, the approximate quantitative analysis of the material drying rate in different positions of plates in big freeze-drying equipments can be made. The research shows that the relation of the sublimation rate G_m of the moisture in material to the vapor pressure P on the upper surface of material is approximately like this: $G_m \propto \sqrt{p_v - p}$. Where the P_v is the saturated vapor pressure on the sublimation interface and is approximated as a constant during the freeze-drying process. Then the relative difference of the drying rate in different position can be estimated by substituting values of vapor pressure P .
- (6) The above result can be the theoretical reference for the design of structure and processing parameters of freeze-drying equipment. For instance, it is usually chosen that the characteristic coefficient α of the passageway in the farthest plate equals to the characteristic coefficient β of the evacuating channel between groups. If the value of deviation ratio of maximal pressure in the whole vacuum chamber is determined, then the relationship of the structural parameters should be

$$\frac{LW^3(B+t)}{2H^2B^3} = 1 + \delta_{\max}. \quad (4.5)$$

5. Calculation Example

Using the above calculation method, the checking computations of vapor pressure distribution in two types of food vacuum freeze-drying equipments are respectively made. The first example is a type of the food vacuum freeze-drying equipment LG-50 with the shelf area of 50 m^2 . The arrangement layout of its plate system is the same as the one shown in Figure 1. Two plate groups are lateral symmetry and each group has sixteen radiation heating plates. Between each two adjoining radiation heating plates, there hangs a material pallet. The total width between each pallet and the plate are all 0.6 m . Between each two groups and on both sides of them, there is a wide evacuating channel which leads to the evacuating port towards the ice condenser. The evacuating port is on the bottom of the central channel between groups (b' in the Figure 1), and its shape is a whole strip along the length direction

Table 1: The structural, processing, and calculated parameters of example 1.

Structural parameters	Processing parameters	Calculated parameters
$B = 0.025$ m	$p_0 = 50$ Pa	$\beta = 5.2 \times 10^{-3}$
$t = 0.065$ m	$G_m = 1$ kg/(m ² h) = 2.78×10^{-4} kg/(m ² s)	$\alpha = 0.097$
$L = 0.3$ m	$T = 310$ K = 37°C	$\delta_{\max} = 0.050$
$W = 0.38$ m	$\mu = 8.8 \times 10^{-5}$ Pa·s	$p_{\max} = 52.5$ Pa
$H = 1.6$ m	$G_z = 1.85 \times 10^{-3}$ kg/(m ² s)	$\Delta p_{\max} = 2.5$ Pa
$n = 1 \sim 15$		

of plates (vertical to the paper in the Figure 1). So the vapor flow of each plate can flow down directly from the central and bilateral evacuating channel to the evacuating port.

The structural parameters, determined processing parameters, and calculated results of the pressure distribution are shown in Table 1. It indicates that the value of the characteristic coefficient β is very small. This shows that the vapor can flow in the wide evacuating channel between groups favorably and will not produce measurable pressure difference on the two sides of the plates. The distribution of vapor pressure in the whole drying chamber is quite even. The deviation ratio of maximal pressure δ_{\max} is only 4.7% and the factual value of pressure difference is 2.5 Pa. The existence of pressure difference is for that the characteristic coefficient α is a little big that is, the pressure difference mainly exists in the central and on the edge of the plates. Furthermore, by adjusting the position of the pallet between two plates to increase the value of B , the value of α can be decreased, therefore, both the deviation ratio of pressure and pressure difference between plates may be decreased. For example, when $B = 0.03$ m and $t = 0.06$ m, the maximal pressure difference is $\Delta p_{\max} = 1.5$ Pa.

The second example is a big food vacuum freeze-drying equipment of which the area is approximately 200 m². The arrangement layout of its plate system is the same as the first example, as shown in Figure 1. There are evacuating channels between groups with the same width in the center and on the two sides of each two plates. The two evacuating ports are respectively on the top of bilateral channels (d and d' in Figure 1). But, because the space between the top radiation heating plate and the top of vacuum drying chamber is too small, the vapor flowing from the two groups of plates cannot flow to the bilateral evacuating ports through the central evacuating channel. It is only discharged through the bilateral evacuating channels. And this equals to only the plates having evacuating channel on one side. At the same time, the evacuating port is set in the center of the freeze-drying chamber of which the length is 8 m (vertical to the paper in Figure 1). So the vapor from the plates on the two ends of chamber need to transfer about 4.5 m along the bilateral evacuating channels before it arrives at the evacuating port. The cross-section area of the evacuating port is much smaller than that of the evacuating channel, so the closer to the evacuating port, the bigger the converted outgassing rate of the channel between groups is. And this makes the average outgassing rate G_z to be about five times of the normal value. These factors all enlarge the uneven level of pressure distribution in the whole drying chamber.

During the calculation of the pressure distribution in the drying chamber, the attention is focused on the vapor flowing process from the plates on two ends of the chamber to the bilateral evacuating channels. The structural parameters, processing parameters and calculated results are shown in Table 2. It indicates that the deviation ratio of maximal pressure in the chamber is close to 18.8% and the maximal pressure difference is $\Delta p_{\max} = 9.4$ Pa. It has exceeded the allowable deviation range of normal work. And it has been found that the drying extent of the freeze-dried food is uneven from the experiment. This indirectly

Table 2: The structural, processing, and calculated parameters of example 2.

Structural parameters	Processing parameters	Calculated parameters
$B = 0.03 \text{ m}$	$p_0 = 50 \text{ Pa}$	$\beta = 0.196$
$t = 0.065 \text{ m}$	$G_m = 1 \text{ kg}/(\text{m}^2\text{h}) = 2.78 \times 10^{-4} \text{ kg}/(\text{m}^2\text{s})$	$\alpha = 0.181$
$L = 0.6 \text{ m}$	$T = 310 \text{ K} = 37^\circ\text{C}$	$\delta_{\max} = 0.188$
$W = 0.38 \text{ m}$	$\mu = 8.8 \times 10^{-5} \text{ Pa}\cdot\text{s}$	$p_{\max} = 59.43 \text{ Pa}$
$H = 4.5 \text{ m}$	$G_z = 8.78 \times 10^{-3} \text{ kg}/(\text{m}^2\text{s})$	$\Delta p_{\max} = 9.43 \text{ Pa}$
$n = 1 \sim 19$		

indicates the correctness of the calculated results. Afterwards, through increasing the number of evacuating port and properly arranging them, the pressure distribution in the drying chamber tends to be even and the drying extent becomes uniform.

6. Conclusion

- (1) The calculation indicates that there exists an uneven vapor pressure distribution in big vacuum freeze-drying equipments due to flowing resistance.
- (2) Though the position of the evacuating port and the structure of the evacuating channel are properly arranging, the uneven pressure distribution can be improved, and the internal pressure difference can be decreased.
- (3) The checking computations indicate that when the values of characteristic coefficient α and β exceed 15% and the value of deviation ratio of maximal pressure exceeds 15%, it can be obviously found that the drying extent is uneven in the freeze-dried food.

References

- [1] A. Ciurzynska and A. Lenart, "Freeze-drying—application in food processing and biotechnology—a review," *Polish Journal of Food and Nutrition Sciences*, vol. 61, no. 3, pp. 165–171, 2011.
- [2] M. J. Pikal, S. Cardon, C. Bhugra et al., "The nonsteady state modeling of freeze drying: inprocess product temperature and moisture content mapping and pharmaceutical product quality applications," *Pharmaceutical Development and Technology*, vol. 10, no. 1, pp. 17–32, 2005.
- [3] C. S. Song, J. H. Nam, C. J. Kim, and S. T. Ro, "Temperature distribution in a vial during freeze-drying of skim milk," *Journal of Food Engineering*, vol. 67, no. 4, pp. 467–475, 2005.
- [4] M. Farid and S. Butcher, "A generalized correlation for heat and mass transfer in freezing, drying, frying, and freeze drying," *Drying Technology*, vol. 21, no. 2, pp. 231–247, 2003.
- [5] A. A. Barresi, R. Pisano, V. Rasetto, D. Fissore, and D. L. Marchisio, "Model-based monitoring and control of industrial freeze-drying processes: effect of batch nonuniformity," *Drying Technology*, vol. 28, no. 5, pp. 577–590, 2010.
- [6] R. J. Litchfield and A. I. Liapis, "An adsorption-sublimation model for a freeze dryer," *Chemical Engineering Science*, vol. 34, no. 9, pp. 1085–1090, 1979.
- [7] R. Pisano, A. A. Barresi, and D. Fissore, "Innovation in monitoring food freeze drying," *Drying Technology*, vol. 29, no. 16, pp. 1920–1931, 2011.

Research Article

SDSim: A Novel Simulator for Solar Drying Processes

Yolanda Bolea, Antoni Grau, and Alexandre Miranda

Automatic Control Department, Technical University of Catalonia UPC, E-08028 Barcelona, Spain

Correspondence should be addressed to Antoni Grau, antoni.grau@upc.edu

Received 16 March 2012; Accepted 26 April 2012

Academic Editor: Zhijun Zhang

Copyright © 2012 Yolanda Bolea et al. This is an open access article distributed under the Creative Commons Attribution License, which permits unrestricted use, distribution, and reproduction in any medium, provided the original work is properly cited.

SDSim is a novel solar dryer simulator based in a multicrop, inclined multipass solar air heater with in-built thermal storage mathematical model. This model has been developed as a designing and developing tool used to study and forecast the behavior of the system model in order to improve its drying efficiency and achieving a return on the dryer investment. The main feature of this simulator is that most of the parameters are permitted to be changed during the simulation process allowing finding the more suitable system for any specific situation with a user-friendly environment. The model has been evaluated in a real solar dryer system by comparing model estimates to collected data.

1. Introduction

Food drying is a very simple, ancient skill. It is one of the most accessible and hence the most widespread processing technology. Sun drying of fruits and vegetables is still practiced largely unchanged from ancient times. Traditional sun drying takes place by storing the product under direct sunlight. Sun drying is only possible in areas where, in an average year, the weather allows foods to be dried immediately after harvest. The main advantages of sun drying are low capital and operating costs and the fact that little expertise is required. The main disadvantages of this method are as follows: contamination, theft, or damage by birds, rats, or insects; slow or intermittent drying and no protection from rain or dew that wets the product encourages mould growth and may result in a relatively high final moisture content; low and variable quality of products due to over- or underdrying; large areas of land needed for the shallow layers of food; laborious since the crop must be turned, moved if it rains; direct exposure to sunlight reduces the quality (color and vitamin content) of some fruits and vegetables. Moreover, since sun drying depends on uncontrolled factors, production of uniform and standard products is not expected. The quality of sun-dried foods can be

improved by reducing the size of pieces to achieve faster drying and by drying on raised platforms, covered with cloth or netting to protect against insects and animals [1, 2].

Due to the current trends towards higher cost of fossil fuels and uncertainty regarding future cost and availability, the use of solar energy in food processing will probably increase and become more economically feasible in the near future. Solar dryers have some advantages over sun drying when correctly designed [3–7]. They give faster drying rates by heating the air to 10–30°C above ambient, which causes the air to move faster through the dryer, reduces its humidity, and deters insects. The faster drying reduces the risk of spoilage, improves quality of the product and gives a higher throughput, so reducing the drying area that is needed. However care is needed when drying fruits to prevent too rapid drying which will prevent complete drying and would result in case hardening and subsequent mould growth. Solar dryers also protect foods from dust, insects, birds, and animals. They can be constructed from locally available materials at a relatively low capital cost, and there are no fuel costs. Thus, they can be useful in areas where fuel or electricity are expensive, land for sun drying is in short supply or expensive, sunshine is plentiful, but the air humidity is high. Moreover, they may be useful as a means of heating air for artificial dryers to reduce fuel costs [8]. Solar food drying can be used in most areas but how quickly the food dries is affected by many variables, especially the amount of sunlight and relative humidity. Typical drying times in solar dryers range from 1 to 3 days depending on sun, air movement, humidity, and the type of food to be dried [9, 10].

The principle that lies behind the design of solar dryers is as follows: in drying relative and absolute humidity are of great importance. Air can take up moisture, but only up to a limit. This limit is the absolute (maximum) humidity, and it is temperature dependent. When air passes over a moist food, it will take up moisture until it is virtually fully saturated, that is, until absolute humidity has been reached. But, the capacity of the air for taking up this moisture is dependent on its temperature. The higher the temperature, the higher the absolute humidity is and the larger the uptake of moisture is too. If air is warmed, the amount of moisture in it remains the same, but the relative humidity falls, and the air is therefore enabled to take up more moisture from its surrounding. To produce a high-quality product economically, it must be dried fast, but without using excessive heat, which could cause product degradation. Drying time can be shortened by two main procedures; one is to raise the product temperature so that the moisture can be readily vaporized, while at the same time the humid air is constantly being removed. The second is to treat the product to be dried so that the moisture barriers, such as dense hydrophobic skin layers or long water migration paths, will be minimized [11].

In environmental and agricultural sciences, complex systems need often to be described with mathematical models. The development of model structures adequate for practical use is carried out with different approaches, depending on the goals of the modeling process as well as on the available information. Most part of environmental and agricultural processes are intrinsically distributed parameter systems, and their behavior is therefore naturally described by partial differential equations (PDEs) that, besides being function of time, depend also on spatial coordinates. Possible examples are given by processes in which mass or energy transport phenomena occur. The resulting models are infinite-dimensional state models. Usually this kind of equations does not have analytical solutions, and numerical methods (such as, Euler method, finite elements techniques, Preissman method, characteristics methods, etc.) are used for their resolution. This type of description usually involves a huge number of parameters and requires time-consuming computations [12]. In the case of solar crop drying system involves the transport of moisture to the surface

of the product and subsequent evaporation of the moisture by thermal heating. Thus, solar thermal crop-drying is a complex process of simultaneous heat and mass transfer. Then, to represent of behavior of the crop drying plant of a precise and complete way, a partial differential equations system is needed.

Agricultural models and decision support systems (DSSs) are becoming increasingly available for a wide audience of users. The Great Plains Framework for Agricultural Resource Management (GPFARM) DSS is a strategic planning tool for farmers, ranchers, and agricultural consultants that incorporates a science simulation model with an economic analysis package and multicriteria decision aid for evaluating individual fields or aggregating to the entire enterprise. The GPFARM DSS is currently being expanded to include (1) better strategic planning by simulating a greater range of crops over a wider geographic range and management systems, (2) incorporating a tactical planning component, and (3) adding a production, environmental, and economic risk component [13]. Another farming simulator in this case specifically for harvesting systems in agriculture is "CropSyst", that is, a multiyear, multicrop, daily time step cropping systems simulation model developed to serve as an analytical tool to study the effect of climate, soils, and management on cropping systems productivity and the environment. The development of this simulator started in the early 1990s, evolving to a suite of programs including a cropping systems simulator, a weather generator (ClimGen), GIS-CropSyst cooperater program (ArcCs), a watershed model (CropSyst Watershed), and several miscellaneous utility programs [14]. Specifically in this simulator a mathematical model which is intended for crop growth simulation over a unit field area (m^2) is implemented [15].

Nowadays in farming sector one of the most potential future applications is the solar drying of agricultural products. Losses of fruits and vegetables during their drying in developing countries are estimated to be 30–40% of production. The postharvest losses of agricultural products in the rural areas of the developing countries can be reduced drastically by using well-designed solar drying systems. Before using the drying systems on large scale, computer simulation models must be performed to simulate the short and long-term performance of the drying systems with and without the storage media to estimate the solar drying curves of the dried products and investigate the cost benefits of the solar drying of agricultural products. So far, some related works [16–23] perform the study and analysis about this kind of systems using the modeling and evolution of their behavior computed mainly in MATLAB (but also in other proprietary code) by the research authors. Therefore, in solar drying systems research as well as in their management, the engineers, researchers, and managers are required to implement their own model to simulate the drying behavior prior to their implementation. This fact is a drawback because there do not exist open source simulators or interactive software to make easier the task of simulating the systems with changing parameters or specifications. The simulator that authors present in this paper is intended to implement a generic user-friendly crop-drying simulator based on solar energy that will reproduce the system behavior and will be accessible to any user requiring a study about this problem without the need of creating his/her own simulator-wasting time and resources. The mathematical model that has been implemented in the simulator is based in a multitray crop drying using inclined multipass solar air heater with in-built thermal storage.

Considering the importance of solar crop drying, this new simulator (SDSim) has been implemented with Easy Java Simulation (Ejs). This software developing tool is explained and referenced in Section 3.

Using the SDSim simulator the temperatures of the different trays, the moisture evaporation, and the drying rate for each produce are predicted. Also the dryer efficiency

to face towards the midday sun. The solar air heater is oriented to face south and tilted at β° angle from the horizontal plane. The system has four drying trays at equal vertical spacing. The drying chamber is provided with glass windows on three sides, that is, east, south, and west to receive additional solar energy. The rear side (north) is provided with an insulating wall. The dryer receives energy from the solar air heater at the first tray. Part of this heat is used to dry the crop in the first tray, and the rest is transferred to the second, third, and fourth trays. Solar energy entering through the windows is absorbed by the crop surface, heats up the crop and accelerates the drying rate. Thus, it improves the system performance. The whole system works as a mixed-mode (passive and active) dryer.

This process involves the mass and heat transfer. Therefore, dried food and the glass' properties should be studied, as the thermodynamic properties. The solar radiation is transmitted from the glass covers and is absorbed by the absorber plate. The air flows in between the glass covers, above the absorber plate, and below the storage material, where it is heated. The energy balance equations on the various components of the system are written with the following assumptions: (i) the heat capacities of the air, glass cover, absorber plate, and insulation are negligible, (ii) there is no temperature gradient along the thickness of the glass cover, (iii) storage material has an average temperature (T_s) at a time (t), (this assumption may be achieved with the small thickness of storage material), (iv) no stratification exists perpendicular to the air flow in the ducts, (v) the system is perfectly insulated, and there is no air leakage, (vi) the volume shrinkage of the crop is negligible during drying, (vii) the system is facing towards midday sun.

The mathematical model that describes the solar drier behavior is represented by the following laws.

2.1. Energy Balance on Solar Air Heater

First Glass Cover

We have

$$\begin{aligned} \alpha_{g1} \cdot I_t \cdot A_{g1} + hr_{g2g1} \cdot (T_{g2} - T_{g1}) \cdot A_{g1} \\ = hc_{g1f1} \cdot (T_{g1} - T_{f1}) \cdot A_{g1} + hc_{g1a} \cdot (T_{g1} - T_a) \cdot A_{g1} \\ + hr_{g1sky} (T_{g1} - T_{sky}) \cdot A_{g1}, \end{aligned} \quad (2.1)$$

where $T_{sky} = T_a - 6$ [24].

Second Glass Cover

We have

$$\begin{aligned} \tau_{g2} \cdot \alpha_{g2} \cdot I_t \cdot A_{g2} + hr_{pg2} (T_p - T_{g2}) \cdot A_{g2} + hc_{f1g2} \cdot (T_{f1} - T_{g2}) \cdot A_{g2} \\ = hr_{g2g1} \cdot (T_{g2} - T_{g1}) \cdot A_{g2} + hc_{g2f2} \cdot (T_{g2} - T_{f2}) \cdot A_{g2} \end{aligned} \quad (2.2)$$

Absorber Plate

We have

$$\tau_{g1} \cdot \tau_{g2} \cdot \alpha_p \cdot I_t \cdot A_p = hr_{pg2} \cdot (T_p - T_{g2}) \cdot A_p + hc_{pf2} \cdot (T_p - T_{f2}) \cdot A_p + hc_{ps} \cdot (T_p - T_s) \cdot A_p. \quad (2.3)$$

Fluid Entrance during the First Glass Cover (for Air Stream I)

We have

$$hc_{g1f1} \cdot (T_{g1} - T_{f1}) \cdot bdx = \dot{m}_a \cdot C_a \cdot \frac{dT_{f1}}{dx} \cdot dx + hc_{f1g2} \cdot (T_{f1} - T_{g2}) \cdot bdx. \quad (2.4)$$

Fluid during the Second Glass Cover (for Air Stream II)

One has

$$hc_{g2f2} \cdot (T_{g2} - T_{f2}) \cdot bdx + hc_{pf2} \cdot (T_p - T_{f2}) \cdot bdx = \dot{m}_a \cdot C_a \cdot \frac{dT_{f2}}{dx} \cdot dx. \quad (2.5)$$

Fluid during the Third Glass Cover (for Air Stream III)

One has

$$hc_{sf3} \cdot (T_s - T_{f3}) \cdot bdx = \dot{m}_a \cdot C_a \cdot \frac{dT_{f3}}{dx} \cdot dx + Ub \cdot (T_{f3} - T_a) \cdot bdx. \quad (2.6)$$

2.2. Storage Material

One has

$$hc_{ps} \cdot (T_p - T_s) \cdot A_p = \dot{m}_s \cdot C_s \cdot \frac{dT_s}{dt} \cdot A_p \cdot hc_{sf3} (T_s - T_{f3}). \quad (2.7)$$

Energy Outlet from Solar Air Heater and Energy Balance on Drying Cabin

Useful energy from solar air heater [25]

$$\dot{Q}_u = \dot{m}_a \cdot C_a \cdot (T_f - T_a) \quad (2.8)$$

2.3. Energy Balance on Different Trays in the Drying Chamber

First Tray

We have

$$\begin{aligned} \dot{Q}_u + \alpha_c \cdot \sum I_i \cdot A_{w1i} \cdot \tau_i - \left(\sum U_i \cdot A_{w1i} + U_b \cdot A_{w1b} \right) \cdot (T_{c1} - T_a) \\ = M_{c1} \cdot C_c \cdot \frac{dT_{c1}}{dt} + A_c \cdot h_{c1} \cdot (T_{c1} - T_{c2}). \end{aligned} \quad (2.9)$$

Second Tray

We have

$$\begin{aligned} A_c \cdot h_{c1} \cdot (T_{c1} - T_{c2}) + \alpha_c \cdot \sum I_i \cdot A_{w2i} \cdot \tau_i - \left(\sum U_i \cdot A_{w2i} + U_b \cdot A_{w2b} \right) \cdot (T_{c2} - T_a) \\ = M_{c2} \cdot C_c \cdot \frac{dT_{c2}}{dt} + A_c \cdot h_{c2} \cdot (T_{c2} - T_{c3}). \end{aligned} \quad (2.10)$$

Third Tray

One has

$$\begin{aligned} A_c \cdot h_{c2} \cdot (T_{c2} - T_{c3}) + \alpha_c \cdot \sum I_i \cdot A_{w3i} \cdot \tau_i - \left(\sum U_i \cdot A_{w3i} + U_b \cdot A_{w3b} \right) \cdot (T_{c3} - T_a) \\ = M_{c3} \cdot C_c \cdot \frac{dT_{c3}}{dt} + A_c \cdot h_{c3} \cdot (T_{c3} - T_{c4}). \end{aligned} \quad (2.11)$$

Fourth Tray

We have

$$\begin{aligned} A_c \cdot h_{c3} \cdot (T_{c3} - T_{c4}) + \alpha_c \cdot \sum I_i \cdot A_{w4i} \cdot \tau_i - \left(\sum U_i \cdot A_{w4i} + U_b \cdot A_{w4b} \right) \cdot (T_{c4} - T_a) \\ = M_{c4} \cdot C_c \cdot \frac{dT_{c4}}{dt} + A_c \cdot h_{c4} \cdot (T_{c4} - T_{ch}). \end{aligned} \quad (2.12)$$

Chamber

We have

$$A_c \cdot h_{c4} \cdot (T_{c4} - T_{ch}) = \dot{m}_a \cdot C_f \cdot (T_{ch} - T_a) + h_{ch} \cdot A_{ch} \cdot (T_{ch} - T_a). \quad (2.13)$$

The performance of the solar collector can be evaluated if the crop temperatures (T_{c1} , T_{c2} , T_{c3} , and T_{c4}) in the different trays are known in above equations. To find out the crop

temperatures, (2.8)–(2.12) can be rearranged into the following four coupled differential equation:

$$\begin{aligned}
 \frac{dT_{c1}}{dt} + k_{11} \cdot T_{c1} + k_{12} \cdot T_{c2} + k_{13} \cdot T_{c3} + k_{14} \cdot T_{c4} &= F_1(t), \\
 \frac{dT_{c2}}{dt} + k_{21} \cdot T_{c1} + k_{22} \cdot T_{c2} + k_{23} \cdot T_{c3} + k_{24} \cdot T_{c4} &= F_2(t), \\
 \frac{dT_{c3}}{dt} + k_{31} \cdot T_{c1} + k_{32} \cdot T_{c2} + k_{33} \cdot T_{c3} + k_{34} \cdot T_{c4} &= F_3(t), \\
 \frac{dT_{c4}}{dt} + k_{41} \cdot T_{c1} + k_{42} \cdot T_{c2} + k_{43} \cdot T_{c3} + k_{44} \cdot T_{c4} &= F_4(t),
 \end{aligned} \tag{2.14}$$

and the coefficients are:

$$\begin{aligned}
 k_{11} &= \frac{h_{c1} \cdot A_c + \sum U_i \cdot A_{w1i} + U_b \cdot A_{w1b}}{M_{c1} \cdot C_c}, & k_{12} &= \frac{-h_{c1} \cdot A_c}{M_{c1} \cdot C_c}, & k_{13} &= 0.0, & k_{14} &= 0.0, \\
 F_1(t) &= \frac{\dot{Q}_u \cdot \alpha_c \cdot \sum I_i \cdot A_{w1i} \tau_i \cdot T_a \sum (U_i \cdot A_{w1i} + U_b \cdot A_{w1b})}{M_{c1} \cdot C_c}, \\
 k_{21} &= \frac{-h_{c1} \cdot A_c}{M_{c2} \cdot C_c}, & k_{22} &= \frac{h_{c2} \cdot A_c + \sum U_i \cdot A_{w2i} + U_b \cdot A_{w2b} + h_{c1} \cdot A_c}{M_{c2} \cdot C_c}, \\
 k_{23} &= \frac{-h_{c2} \cdot A_c}{M_{c2} \cdot C_c}, & k_{24} &= 0.0, \\
 F_2(t) &= \frac{\alpha_c \cdot \sum I_i \cdot A_{w2i} \tau_i + T_a \cdot \sum (U_i \cdot A_{w2i} + U_b \cdot A_{w2b})}{M_{c2} \cdot C_c}, \\
 k_{31} &= 0.0 & k_{32} &= \frac{-h_{c2} \cdot A_c}{M_{c3} \cdot C_c}, \\
 k_{33} &= \frac{h_{c3} \cdot A_c + \sum U_i \cdot A_{w3i} + U_b \cdot A_{w3b} + h_{c2} \cdot A_c}{M_{c3} \cdot C_c}, & k_{34} &= \frac{-h_{c3} \cdot A_c}{M_{c3} \cdot C_c}, \\
 F_3(t) &= \frac{\alpha_c \cdot \sum I_i \cdot A_{w3i} \tau_i \cdot T_a \cdot \sum (U_i \cdot A_{w3i} + U_b \cdot A_{w3b})}{M_{c3} \cdot C_c}, \\
 k_{41} &= 0.0, & k_{42} &= 0.0, & k_{43} &= \frac{-h_{c3} \cdot A_c}{M_{c4} \cdot C_c}, \\
 k_{44} &= \frac{U_{ch} + \sum U_i \cdot A_{w4i} + U_b \cdot A_{w4b} + h_{c3} \cdot A_c}{M_{c4} \cdot C_c}, \\
 F_4(t) &= \frac{\alpha_c \cdot \sum I_i \cdot A_{w4i} \tau_i \cdot T_a \cdot \sum (U_i \cdot A_{w4i} + U_b \cdot A_{w4b}) + T_a \cdot U_{ch}}{M_{c4} \cdot C_c}, \\
 U_{ch} &= \frac{(\dot{m}_a \cdot C_f + h_{ch} \cdot A_{ch}) h_{c4} \cdot A_c}{M_{c4} \cdot C_f + h_{ch} \cdot A_{ch} + h_{c4} \cdot A_c}.
 \end{aligned} \tag{2.15}$$

The rate of moisture content change in thin drying bed can be written as the following drying equation:

$$\frac{dM}{dt} = -K_d(M - M_e), \quad (2.16)$$

where $K_d = a \exp(-b'/T_c)$, and M_e is the equilibrium moisture content. After a considerable time, the evolution of M tends to M_e . In this case, M_e is not a constant value, but it depends on the temperature and the water activity reaching an equilibrium with its variation. Regarding this variable, there exist different models to calculate it corresponding to the family of the desorption isotherms. For an extensive review and models discussion, see [26]. The most accepted model has been proposed by Henderson at [27], and the model is

$$M_e = \left[-\frac{\ln(1 - a_w)}{A(T_C + B)} \right]^{1/D}. \quad (2.17)$$

The constants and the value for the water activity are found by experimentation in every crop to be dried.

Another important output variable is the system drying efficiency, and it can be understood by the overall thermal efficiency of the drying. This overall thermal efficiency can be defined as the ratio of heat energy used in the vaporization of the moisture plus the thermal energy used to raise the temperature of the crops, to that of solar radiation collected by the solar air heater and the crop surface. In this work, the following expression is used to evaluate it:

$$\eta_o = \frac{L_c \cdot \sum_{t=1}^{24} \sum_{j=1}^4 M_{ev,t,j} + C_c \cdot \sum_{t=1}^{24} \sum_{j=1}^4 M_{c,t,j} \cdot (T_{c,t,j} - T_{c,t-1,j})}{3600 \cdot \sum_{t=1}^{24} (A_p \cdot I_t + A_c \cdot I_i)}, \quad (2.18)$$

where the vertical radiation I_i is the sum of the radiations that receive the solar drier from the windows oriented to the sun during all the day, that is,

$$I_i = I_{\text{south}} + I_{\text{west}} + I_{\text{east}} \quad (2.19)$$

calculated using classical formulation found in [28, 29].

M_{ev} is the moisture evaporation in kg water, in other words, the variation of the mass of water in the crop. This mass of water can be calculated using the initial value of the mass of the crop (mass of water + mass of dry matter) and its moisture content using the next relations

$$\begin{aligned} \text{mass dry matter} &= \frac{M_c(t=0)}{1 + M(t=0)}, \\ \text{mass of water}(t) &= M(t) \cdot \text{mass dry matter}, \\ M_{ev}(t) &= \text{mass of water}(t-1) - \text{mass of water}(t) \end{aligned} \quad (2.20)$$

evaluated every hour.

3. Simulator Development

3.1. Easy Java Simulations

Easy Java simulations (EJSs) is the tool that authors chose to program models and the simulation views. EJS is a freeware, open-source tool developed in Java, specifically designed to create interactive dynamic simulations [30]. It was originally designed to be used by students for interactive learning under the supervision of educators with a low programming level. However, the user needs to know in detail the analytical model of the process and the design of the graphical view. EJS guides the user in the process of creating interactive simulations, in a simple and practical way.

The architecture of EJS derives from the model-view control paradigm, whose philosophy is that interactive simulations must be composed of three parts: the model, the view, and the control. According to that, the steps to build an application in EJS are the following. (1) To define the model is necessary to specify the variables that describe the system and the mathematical equations interrelating them, (2) to define the view in order to represent the states of the process, and finally (3) to define the control in order to describe the actions that the modeler can execute above the simulation. These three parts are interconnected because the model affects to the view, and the control actions affect to behavior of the model. Finally, the view affects to the model and to the control because the graphical interface can contain information about them.

EJS simulations are created through specifying a model to be run by the internal simulation engine and by building a view to visualize the model state and that readily responds to user interactions. So, to define the model in EJS, it is necessary to identify the variables that describe the process, to initialize them, and also to describe the mathematical equations that generate the model. The view is the user-to-model interface of interactive simulations. It is intended to provide a visual representation of the model's relevant properties and dynamic behavior and also to facilitate the user's interactive actions. EJS includes a set of ready-to-use visual elements. With them, the modeler can compose a sophisticated view in a simple, drag, and drop way. The properties of the view elements can be linked to the model variables, producing a bi-directional flow of information between the view and the model. Any change of a model variable is automatically displayed by the view. Reciprocally, any user interaction with the view automatically modifies the value of the corresponding model variable. Once the modeler has defined the model and the view of the interactive simulation, EJS generates the Java source code of the simulation program, compiles the program, packs the resulting object files into a compressed file, and generates HTML pages containing the narrative and the simulation as an applet. The user can readily run the simulation and/or publish it on the Internet. Easy Java simulations, the software tool, a complete English manual for it, can be downloaded for free from EJS' web server at [31].

To summarize, the model is the scientific part of the simulation; yet the creation of the necessary graphical user interface (the view) is the part of the simulation that demands more knowledge of advanced programming techniques.

3.2. SDSim Simulator Development

When developing a simulation with EJSs there are three separate parts: description, model, and views.

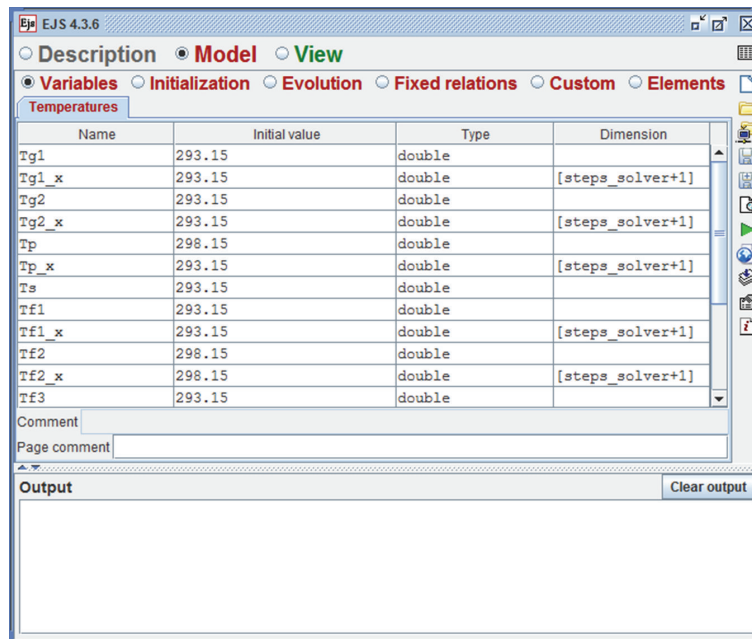


Figure 2: Variables declaration screen.

The description part is devoted to describe the model, as an introduction, with the most relevant equations, parameters and as many figures and pictures as the developer would like to add to make attractive the read of this introduction.

The model part is the heart of the simulator, and only Java code is allowed. All the evolution equations will be programmed as well as their relationships. All the variables and their initializations will be programmed. There is also an Ordinary Differential Equations (ODE) editor where the equations can be programmed.

The view part is necessary to have interaction with the simulation. The view editor allows the programmer to design a layout of the input/output. With some drawing elements, different views can be created and, the most important thing, those drawings elements can be associated to model variables. Then, at simulation time, as the variables change with time, the elements also change creating a dynamic effect of the simulation. Obviously, some plots can also be created. The parameters of the simulation can be also modified at execution time through button or sliders, modifying in real time the simulation. This interaction with the user makes EJS very attractive to develop and utilize this software to design, implement, and use it.

3.2.1. The Model

The first step when programming the model is to declare the variables and constants that will be used along the program. Figure 2 shows the variable declaration screen. For any variable, its name, initial value, type, and dimension can be defined.

Once the variables have been declared, if they need to be initialized using not single values but equations or more complex functions, the Initialization tab can be used. All the

The screenshot shows the EJS 4.3.6 interface with the 'Model' tab selected. The code in the 'Climatic' section is as follows:

```

a1_amb = Math.PI/((2.0*Math.PI*14.0/24.0)-(2.0*Math.PI*6.0/24.0)-2.0*Math.PI);
a2_amb = Math.PI/((2.0*Math.PI*6.0/24.0)-(2.0*Math.PI*14.0/24.0));
a3_amb = Math.PI/(2.0*Math.PI+(2.0*Math.PI*6.0/24.0)-(2.0*Math.PI*14.0/24.0));
b1_amb = -a1_amb*(2.0*Math.PI*6.0/24.0);
b2_amb = -a2_amb*(2.0*Math.PI*14.0/24.0);
b3_amb = -(Math.PI+a3_amb*(2.0*Math.PI*14.0/24.0));

w = 2.0*Math.PI*thora/24.0;

if (thora>0.0 && thora<=6.0) {
  Ta = Tmax-((Tmax-Tmin)/2.0)*(1.0+Math.cos(a1_amb*w+b1_amb));
} else if (thora>6.0 && thora<=14.0) {
  Ta = Tmin+((Tmax-Tmin)/2.0)*(1.0+Math.cos(a2_amb*w+b2_amb));
}

```

Figure 3: Complex variable initialization.

The screenshot shows the EJS 4.3.6 interface with the 'Model' tab selected. The 'Evolution' section displays a table of ordinary differential equations (ODEs) for a solar drier model. The table has columns for 'Indep. Var.', 't.time', 'State', 'Rate', and 'Prelim code'. The equations are as follows:

Indep. Var.	t.time	State	Rate	Prelim code
		$\frac{d Ts}{d time}$	$(d2 * Tp + d3 * Tf3 - Ts) / d1$	
		$\frac{d Tc1}{d time}$	$F1 - k11 * Tc1 - k12 * Tc2 - k13 * Tc3 - k14 * Tc4$	
		$\frac{d Tc2}{d time}$	$F2 - k21 * Tc1 - k22 * Tc2 - k23 * Tc3 - k24 * Tc4$	
		$\frac{d Tc3}{d time}$	$F3 - k31 * Tc1 - k32 * Tc2 - k33 * Tc3 - k34 * Tc4$	
		$\frac{d Tc4}{d time}$	$F4 - k41 * Tc1 - k42 * Tc2 - k43 * Tc3 - k44 * Tc4$	
		$\frac{d M1}{d time}$	$-Kd1 * (M1 - Me1)$	
		$\frac{d M2}{d time}$	$-Kd2 * (M2 - Me2)$	
		$\frac{d M3}{d time}$	$-Kd3 * (M3 - Me3)$	
		$\frac{d M4}{d time}$	$-Kd4 * (M4 - Me4)$	

Additional parameters shown in the interface include: FPS: 2, SPD: 1, Solver: Fehlberg 8, Tol: 0.00001, and Autoplay: Comment.

Figure 4: Ordinary differential equations editor.

```

EJS 4.3.6 - Solar Drier.ejs
Description Model View
Variables Initialization Evolution Fixed relations Custom Elements
ssolver_System

public void ssolver_System() {

    int j;
    double k1_f1,k2_f1,k3_f1,k4_f1;
    double k1_f2,k2_f2,k3_f2,k4_f2;
    double k1_f3,k2_f3,k3_f3,k4_f3;
    double h;
    h = L/(double)steps_solver;

    for (j = 0 ; j < steps_solver ; j++) {

        k1_f1 = (Tg1_x[j]*e2+Tg2_x[j]*e3-Tf1_x[j])/e1;
        k1_f2 = (Tg2_x[j]*f2+Tp_x[j]*f3-(Tf2_x[j]+0.5*k1_f2*h))/f1;
        k1_f3 = (Ts*g2+Ta*g3-Tf3_x[j])/g1;

        k2_f1 = (Tg1_x[j]*e2+Tg2_x[j]*e3-(Tf1_x[j]+0.5*k1_f1*h))/e1;
        k2_f2 = (Tg2_x[j]*f2+Tp_x[j]*f3-(Tf2_x[j]+0.5*k2_f2*h))/f1;
        k2_f3 = (Ts*g2+Ta*g3-(Tf3_x[j]+0.5*k2_f3*h))/g1;

        k3_f1 = (Tg1_x[j]*e2+Tg2_x[j]*e3-(Tf1_x[j]+0.5*k2_f1*h))/e1;
        k3_f2 = (Tg2_x[j]*f2+Tp_x[j]*f3-(Tf2_x[j]+0.5*k2_f2*h))/f1;
        k3_f3 = (Ts*g2+Ta*g3-(Tf3_x[j]+0.5*k2_f3*h))/g1;

        k4_f1 = (Tg1_x[j]*e2+Tg2_x[j]*e3-(Tf1_x[j]+k3_f1*h))/e1;
        k4_f2 = (Tg2_x[j]*f2+Tp_x[j]*f3-(Tf2_x[j]+k3_f2*h))/f1;
        k4_f3 = (Ts*g2+Ta*g3-(Tf3_x[j]+k3_f3*h))/g1;

        Tf1_x[j+1] = Tf1_x[j]+(h/6.0)*(k1_f1+2.0*k2_f1+2.0*k3_f1+k4_f1);
        Tf2_x[j+1] = Tf2_x[j]+(h/6.0)*(k1_f2+2.0*k2_f2+2.0*k3_f2+k4_f2);
        Tf3_x[j+1] = Tf3_x[j]+(h/6.0)*(k1_f3+2.0*k2_f3+2.0*k3_f3+k4_f3);

        Tg2_x[j+1] = ((b1+c1*b2+a1*b4)+Tf1_x[j]*(b3+a3*b4)+Tf2_x[j]*(c3*b2+b5)+Ts*
        Tp1_x[j+1] = a1+Tg2_x[j]*a2+Tf1_x[j]*a3+Ta*a4+Tkva5;
    }
}

```

Figure 5: Runge-Kutta solver in Java code.

code programmed here will be executed once and always before the simulation starts. A snapshot of the model variables initialization can be seen in Figure 3.

The next step is to implement the evolution of the simulation. Mainly, the model is defined using ordinary differential equations (ODEs), and EJS provides a tab to declare the equations that will be automatically solved. Programmer is allowed to choose among different numerical methods to integrate the equations, choosing also the step of integration. Among those methods programmer can find the simple Euler method, Euler-Richardson, Runge-Kutta of different orders, Bogacki-Shampine 3(2), Cash-Karp 5(4), different Fehlberg methods, different Dormand-Prince methods, Radau 5(4), and even a sophisticated QSS 3 method. The editor accepts as many equations are required in the model.

If the model incorporates partial equations (with more than one independent variable), or some ODEs with different independent variable or even if the model has algebraic equations, then the model can be implemented without the editor but using another tab in the same evolution step where Java code is accepted. Also, it is possible to combine both, the Java code and the ODE editor. This is the case in the proposed model in this paper. The ODE editor is used to program the equations in the time as independent variable, but for those equations in the model that use x as independent variable a numerical method has been programmed.

Figure 4 shows the ODE editor; note the solver method popup menu. Its simplicity makes easier to implement any ODE equations system with an independent variable. In Figure 5 the evolution of the simulation can be programmed directly in Java code; in this case, the figure shows the programming of a Runge-Kutta solver method [32, 33]. The combination

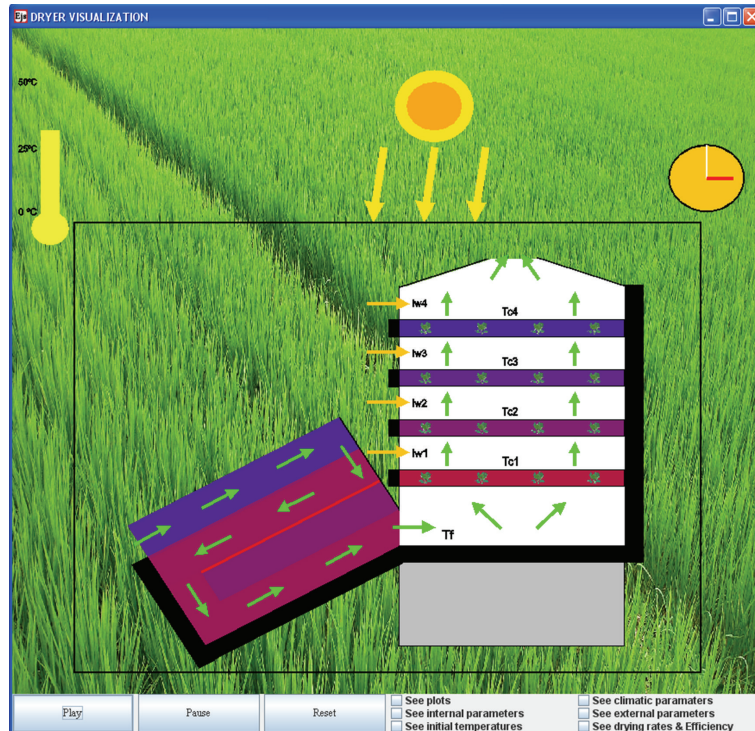


Figure 6: Main view of the solar dryer simulator (SDSim).

of both makes EJS very useful to program models in a modular, coherent programming scheme.

Tabs “Custom” and “Fixed Relations” allow the programmer to insert additional code for functions called from the “Evolution” tab. This code will be programmed in Java.

3.2.2. The View

To define the view of the simulation, there is a special editor that allows inserting the graphical elements in a tree structure. Those elements are plots, pictures, and interactive objects.

For the main view, authors have designed a draw with the most important elements in the simulation in the solar drier: the air flow, the multitray, the sun movement, the temperature evolution, and the time. This view is shown in Figure 6. Together with the drawing elements, there are buttons to start, pause, and reset the simulation. As the simulation evolves in time, the different elements associated to the model variables also change their shape or position in the screen. For instance, the sun moves from left to right simulating the day (from east to west), incrementing its size until midday, and decrementing it during the afternoon. Also the arrows, simulating the sun rays, point always to the solar drier as the sun moves. The effect is very attractive and very comprehensive for those who are not used on programming. In this view, it is possible to select among different plots to show that the evolution of the variables respects the independent variable (time t or position x) as

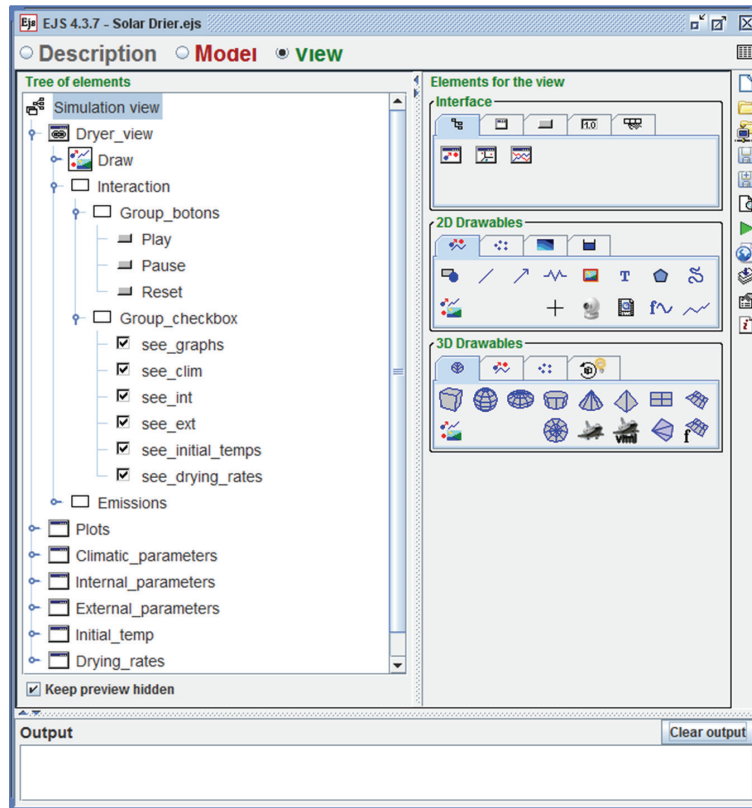


Figure 7: Main menu to create a view.

a classical plot. Moreover, it is possible to open some dialogs to modify the model parameters to change the simulation setup and evolution.

To interface the simulation with the user, six different frames are proposed: the graphical evolution (Drier view); four frames to modify the model parameters (internal parameters, external parameters, climatic parameters, and initial temperatures) and one frame to show numerical plots of output model variables.

To create a view, a tree structure must be followed. In this structure, programmer can simultaneously insert interfaces, 2D drawables, and 3D drawables, depending on the required element and choosing among an already defined library of objects. Figure 7 shows the tree structure used to represent the view of the solar drier and just a few of the elements needed to create the view, plots and dialogs to interface with the user.

Among several elements to show in the simulation evolution, one of the most useful are plots that represent numerically the variables evolution along the simulation-independent variable. Firstly, a Plotting Panel has to be inserted in the tree of elements in a desired position. Then a trace element has to be inserted within the plotting panel indicating which variable must be represented. In Figure 8, the trace of variable T_a respect the time has been inserted in a plotting panel.

To draw the main view, the solar drier, a 2D-drawable element is required, and specifically is the element "shape," see Figure 9. In this element, it is possible to indicate the position, size, scale, and different transformations for a predefined shape. In this case

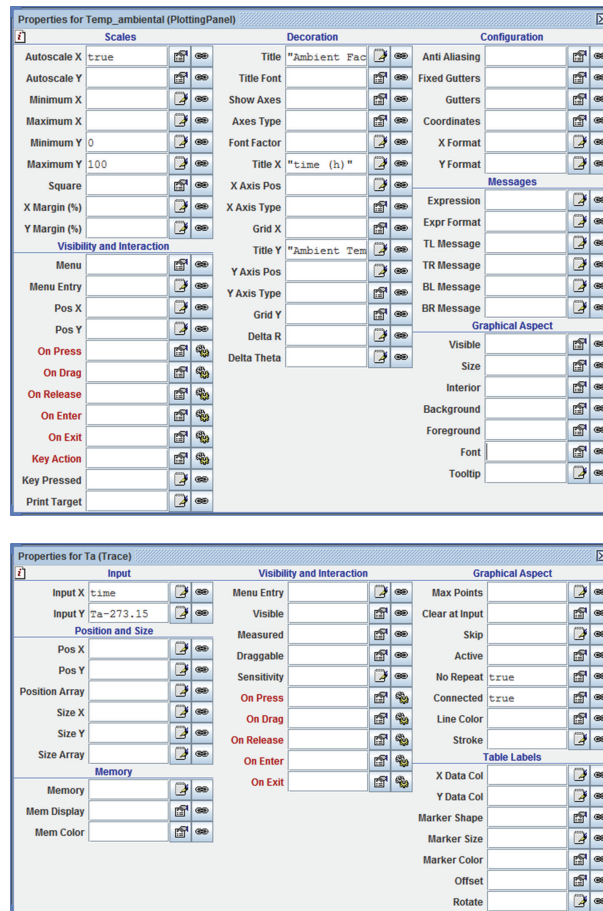


Figure 8: EJS elements to create a plotting panel and a trace within it.

the shape is a rectangle filled in with a color indicated in the variable “color_g1” that changes along the simulation evolution. The remainder elements in the main view are built in a similar way (round shape for the sun and the clock, arrow elements for the sun rays, rectangle for the temperature...) with varying parameters associated to simulation variables. The final view is quite laborious because all the elements must coincide and evolve properly, but the result is sometime astonishing for the user.

4. Simulation Results

Before executing the simulation, user has to initialize the different parameters and variables involved in the drying process. More specifically, climatic conditions, external parameters, internal parameters, and the initial values of the temperatures need to be set. Once all these parameters have been selected, the user can initiate the simulation by clicking on the play button.

Among the different variables studied in the simulation, it is necessary to differentiate between those variables in which evolution depends only on the time $f(t)$ and those which

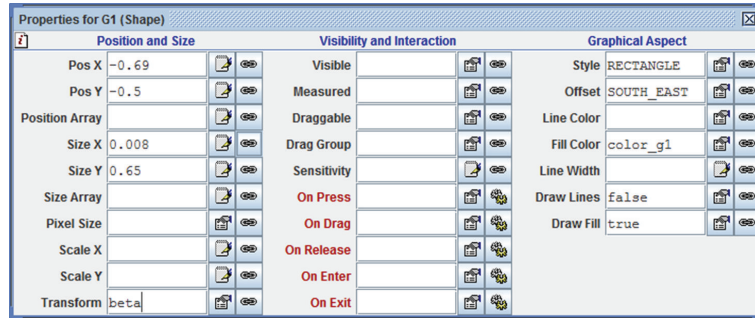


Figure 9: Element to represent shapes.

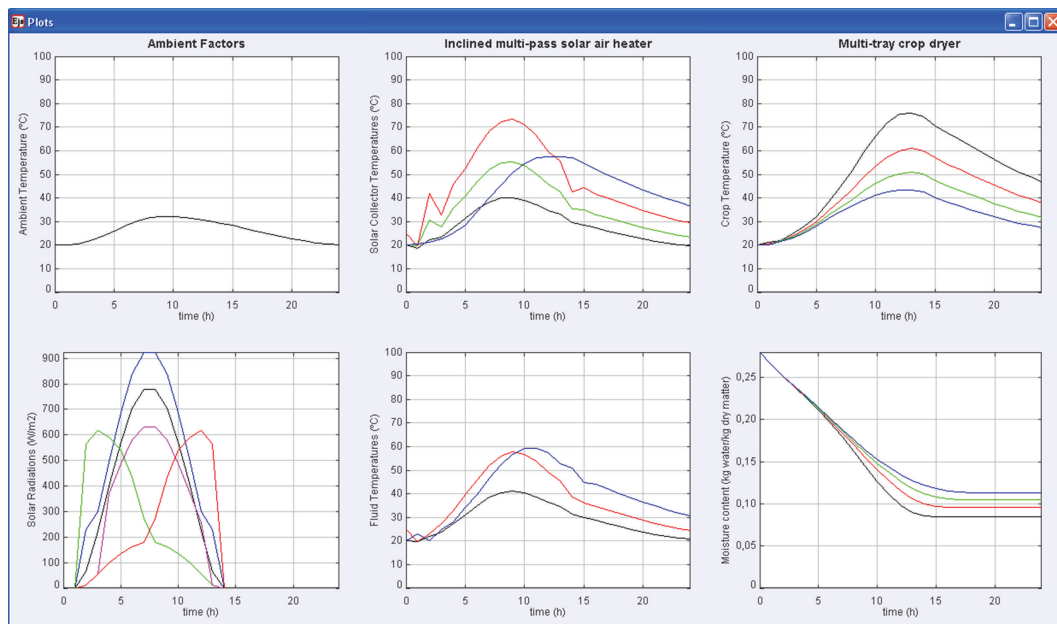


Figure 10: Plots representing output model variables.

evolve also as a function of position $f(x, t)$. Except the storage material, which is considered to be at the same temperature in each instant of time, the rest of temperatures of the multipass air heater depend on both time and position. In contrast, the temperatures of the crops and their moistures are only a function of time.

Easy Java does not permit to solve partial differential equations or ordinary differential equations with different independent variable using the ODE editor, and only it is allowed to solve ordinary differential equations with one independent variable. In our case, to solve the equations in time t , the ODE editor is used with Fehlberg-8(7) numerical method. Instead, when the equations to be solved are in the independent variable x , a 4th order Runge-Kutta is implemented in Java, see Figure 5. Both methods give accurate results and satisfactory solutions [32, 33].

The simulation begins ($t = 1$ hour) with the computation of the time-dependent variables which are the storage material temperature (T_s), the crop temperatures

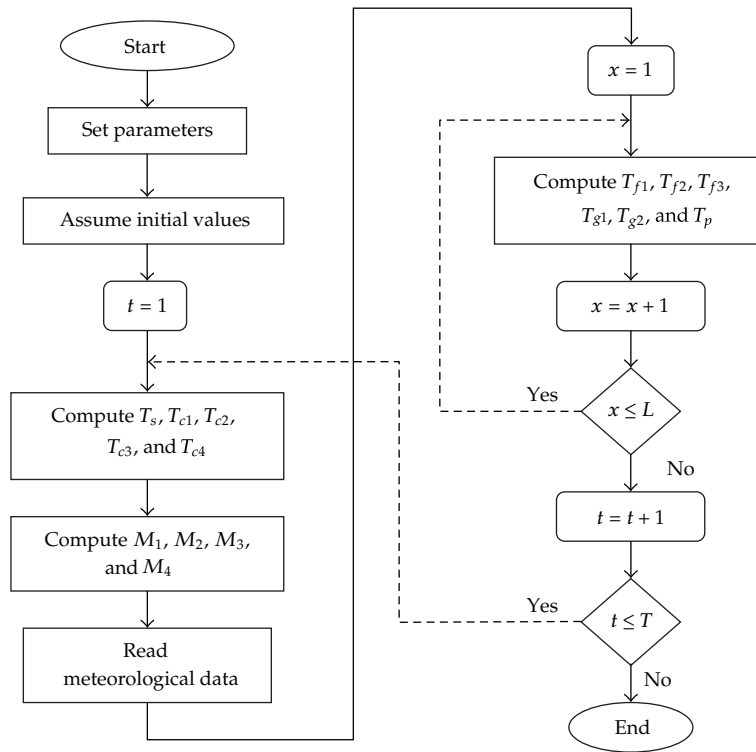


Figure 11: Simulation flux diagram.

$(T_{c1}, T_{c2}, T_{c3},$ and $T_{c4})$, and the crops moisture content ($M_1, M_2, M_3,$ and M_4). Once they are calculated, the external meteorological data (solar radiation and ambient temperature) is read. After this, the position is initialized ($x = 1$), and the rest of the collector temperatures are calculated ($T_{g1}, T_{g2}, T_p, T_{f1}, T_{f2},$ and T_{f3}). Then, the time remains fixed but the position x is incremented, evaluating these collector temperatures for different positions of x until the total length L is reached, the integration step for x can be chosen by the programmer. Finally, the time is incremented, and this process is repeated for each hour up to the maximum time established T , which is a complete day (24 h) for the images shown in this paper. Figure 11 represents the flux diagram of execution.

It has to be noticed that the increment of time and the computation of the time depending variables is done in the same step by the ODE solver of the Easy Java Simulation.

The main view of the simulation can be seen in Figure 6. The view represents the solar drier and all the changing elements during the simulation: air flow in the heater, temperatures in the heater and the drier, the sun size and position, the sun rays, the clock, the thermometer, and air flow along the trays. Each graphical element is associated to an output variable, and then the elements move and evolve in the view. At the bottom of the main view, there are the starting, pausing, and resetting buttons as well as the boxes to select the windows to see the plots or the dialogs. If plots are selected then the plots in Figure 10 pop in the screen showing six plots representing the most relevant variables in the model. The plot in the upper right position shows the evolution of the temperature in each tray where the crops are located to be dried. If a click is done on the plot, it pops a more detailed image, shown in Figure 12. In

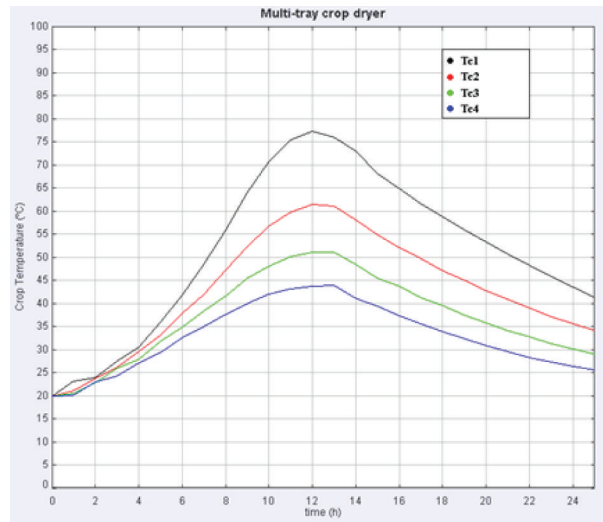


Figure 12: Enlargement of the multitray crop dryer temperature.

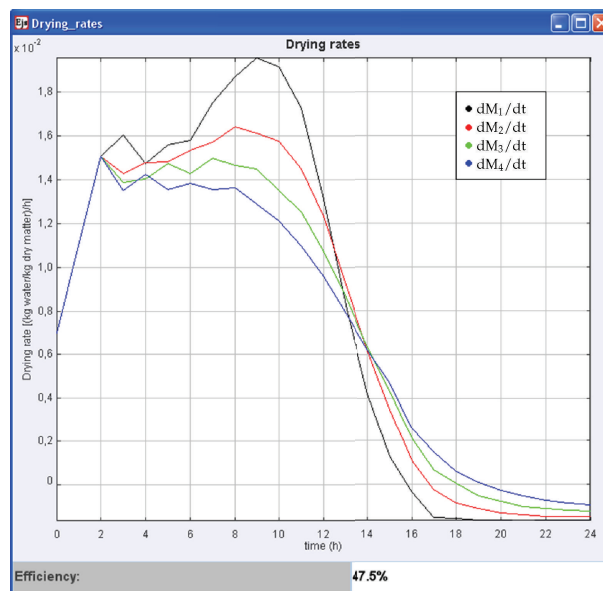


Figure 13: Variation of the moisture contents.

this new image, the legend for each trace appears in the plotting area allowing knowing and following the temperature for tray along the simulation time.

A very interesting result of the simulation is the moisture contents of the different crops placed in the trays. The evolution of this variable, M , can be seen in Figure 10 lower right, and it indicated how the moisture contents decrease with time until a final value that it is considered the final moisture for that crops. From this bottom value, the moisture reaches the equilibrium moisture contents, M_e in the model, that it is a value that depends on the external factors such as the temperature. In this example, for a rough rice crop, the

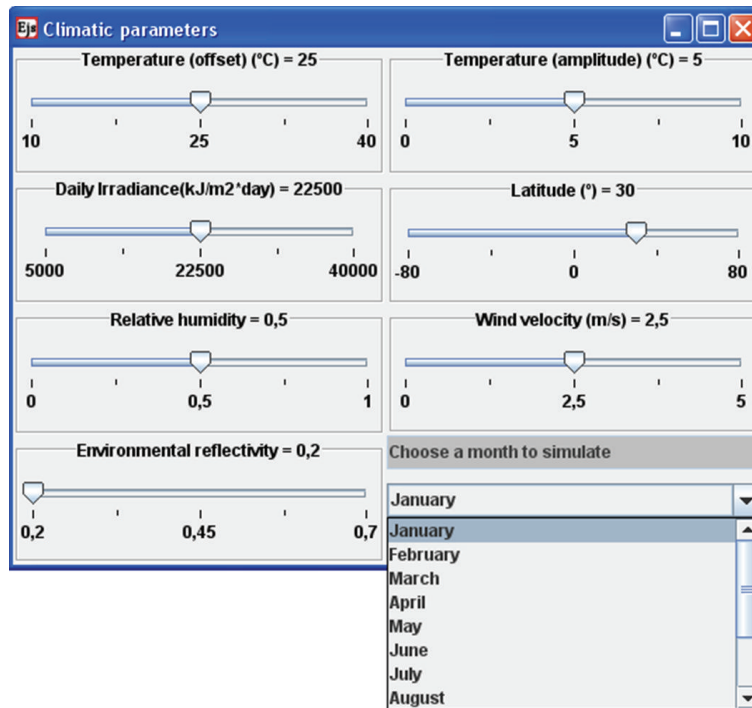


Figure 14: Dialog to modify the climatic parameters.

equilibrium varies between 0.08 and 0.10 kg water/kg of dry matter in the lower tray (the most effective in the drying process) [9, 26].

It is also of interest to plot the variation of the moisture contents (dM/dt) along the time to see the most effective hours of drying. As it was expected, the solar drier accumulates heat during the day and reaches its maximum drying effect in the afternoon, with a peak at 3.00 PM. The plot can be seen in Figure 13 for each tray in the drier. At the bottom of the figure, the efficiency is displayed. This value is calculated following the expression for η_0 in the model equations. The interactive simulator allows the engineers and drier designers to change the parameters in order to find the most efficient design for new solar driers. This is the final goal of the simulator.

All the results and values for the output variables have been validated with the real results in [19], showing that the model behaves as it is expected corresponding to the collected experimental data in the solar drier. If the model works properly with the real data and the validation is correct, then the parameters can be changed and the new results are expected to correspond to the design of the resulting solar drier with those modified parameters.

One important feature of EJS is the interactivity that user can have with the simulation, and it is achieved with the modification of the model parameters during the simulation. In Figures 14, 15, and 16, the current values of different model parameters are displayed and, using the sliders, the pop-up menus or the numerical fields, they can be changed. Once they are changed, the simulation resumes executing with the modified values, changing the evolution according to these new parameter values.

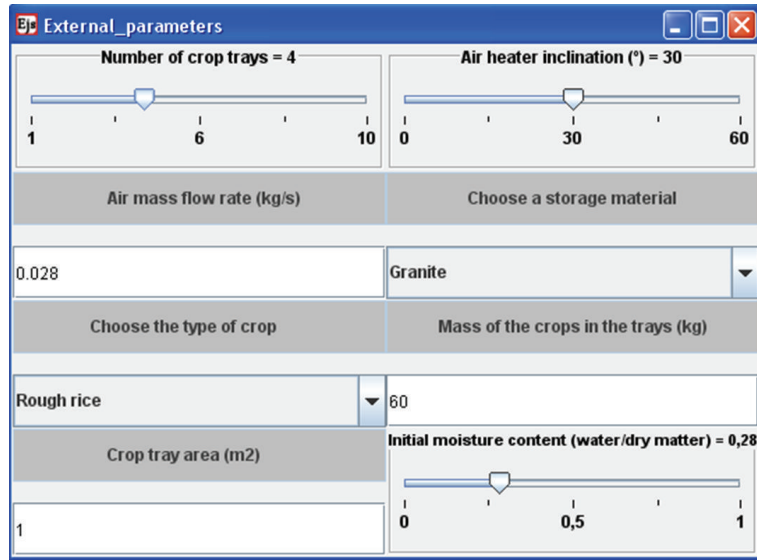


Figure 15: Dialog to modify the external parameters.

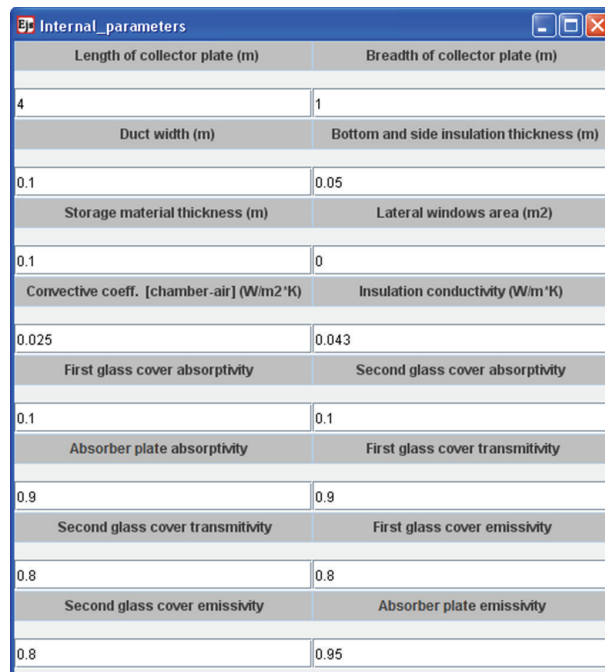


Figure 16: Dialog to modify the internal parameters.

In order to set the input variables to the model (temperature and solar radiation), the user can choose between to use a mathematical function to generate those values or to choose a database with experimental data [28, 29, 34]. This aspect enriches the simulator, and it is very useful to test real designs with actual collected data.

5. Conclusions

In this research paper, authors have implemented a novel kind of simulator or solar driers. The model is based in a real drier in order to validate the model and the simulator. This model is based in a multicrop, inclined multipass solar air heater with in-built thermal storage drier. The simulator has the ability to interact with the user, and the model parameters can be changed during the evolution time modifying the simulation results. The objective of the simulator is to find the most efficient design for new solar driers.

Nomenclature

A :	Area, m^2
A, B, D, b' :	Constants
a_w :	Water activity, decimal
b :	Breadth of collector plate, m
C :	Specific heat at constant pressure, $J \cdot kg^{-1} \cdot K^{-1}$
d :	Duct width, m
g :	Acceleration due to gravity, $m \cdot s^{-2}$
hc :	Convective heat transfer coefficient, $W \cdot m^{-2} \cdot K^{-1}$
h_c :	Convective heat and mass transfer coefficient from crop to air, $W \cdot m^{-2} \cdot K^{-1}$
h_{ch} :	Convective heat loss coefficient from chamber to air, $W \cdot m^{-2} \cdot K^{-1}$
hr :	Radiative heat transfer coefficient, $W \cdot m^{-2} \cdot K^{-1}$
h_o :	Convective and radiative heat transfer coefficient due to wind, $W \cdot m^{-2} \cdot K^{-1}$
I_h :	Hourly average solar radiation on horizontal surface, $W \cdot m^{-2}$
I_t :	Hourly average solar radiation on tilted surface, $W \cdot m^{-2}$
I_v :	Hourly average solar radiation on vertical surface, $W \cdot m^{-2}$
K :	Conductivity, $W \cdot m^{-1} \cdot K^{-1}$
K_d :	Drying constant, s^{-1}
L :	Length of collector plate, m
L_c :	Latent heat of vaporization of moisture from crop, $J \cdot kg^{-1}$
l :	Thickness, m
M :	Moisture content of grain, kg water/kg of dry matter
M_c :	Mass of the crop in the trays, kg
M_e :	Equivalent moisture content, kg water/kg of dry matter
M_{ev} :	Moisture evaporation per hour, $kg \cdot water \cdot h^{-1}$
m_s :	Mass of storage material, kg
m_a :	Mass flow rate, $kg \cdot s^{-1}$
Nu :	Nusselt number
Q_u :	Rate of useful thermal energy from solar air heater, W
Ra :	Rayleigh number
T :	Temperature, K
T_c :	Temperature, $^{\circ}C$
ΔT :	Temperature difference, K
t :	Time, s
U_b :	Bottom or side loss coefficient, $W \cdot m^{-2} \cdot K^{-1}$
U_i :	Overall heat loss coefficient from the glass windows, $W \cdot m^{-2} \cdot K^{-1}$
v :	Wind velocity, $m \cdot s^{-1}$
x :	Length of coordinate in direction of flow, m.

Greeks

a :	Absorptivity
α_f :	Diffusivity of air, $\text{m}^2 \text{s}^{-1}$
β :	Tilt angle of collector, degree
β' :	Expansion factor, K^{-1}
ε :	Emissivity
γ :	Relative humidity of air, decimal
η_o :	Overall thermal efficiency, %
ν_f :	Kinematic viscosity of air, $\text{m}^2 \text{s}^{-1}$
ρ :	Density, $\text{kg}\cdot\text{m}^{-3}$
σ :	Stefan-Boltzmann constant, $\text{W}\cdot\text{m}^{-2}\cdot\text{K}^{-4}$
τ :	Transmissivity.

Subscripts

a :	Air
b :	Bottom and side insulation of collector and dryer
ba :	Bottom of insulation to air
c :	Crop
$c1, c2, c3, c4$:	Crop in tray 1, 2, 3, 4
ch :	Chamber
f :	Fluid (air)
$f1$:	Air stream-I
$f1g2$:	Air in stream-I to second glass cover
$f2$:	Air stream-II
$f3$:	Air stream-III
$g1$:	First glass cover
$g1a$:	First glass cover to air
$g1f1$:	First glass cover to air in stream I
$g1sky$:	First glass cover to sky
$g2$:	Second glass cover
$g2g1$:	Second glass cover to first glass cover
$g2f2$:	Second glass cover to air in stream II
i :	Sides of glass window, integer 1, 2, 3
j :	Number of trays, integer 1, 2, 3, 4
p :	Absorber plate
$pf2$:	Absorber plate to air in stream II
$pg2$:	Absorber plate to second glass cover
ps :	Absorber plate to storage material
s :	Storage material
$sf3$:	Storage material to air in stream III
sky :	Sky
w :	Window
$w1, w2, w3, w4$:	Window of tray 1, 2, 3,4.

Acknowledgments

This work has been partially funded by the Technical University of Catalonia under the Project UPC-ICE "2011 Pedagogical Innovation Projects."

References

- [1] I. Farkas, "Solar drying," *Stewart Postharvest Review*, vol. 4, no. 2, article 9, 2008.
- [2] K. R. Manohar and P. Chandra, "Drying of agricultural produce in a greenhouse type solar dryer," *International Agricultural Engineering Journal*, vol. 9, no. 3, pp. 139–150, 2000.
- [3] S. Aboul-Enein, A. A. El-Sebaei, M. R. I. Ramadan, and H. G. El-Gohary, "Parametric study of a solar air heater with and without thermal storage for solar drying applications," *Renewable Energy*, vol. 21, no. 3-4, pp. 505–522, 2000.
- [4] M. M. Alkilani, K. Sopian, M. A. Alghoul, M. Sohif, and M. H. Ruslan, "Review of solar air collectors with thermal storage units," *Renewable and Sustainable Energy Reviews*, vol. 15, no. 3, pp. 1476–1490, 2011.
- [5] O. V. Ekechukwu and B. Norton, "Review of solar-energy drying systems II: an overview of solar drying technology," *Energy Conversion and Management*, vol. 40, no. 6, pp. 615–655, 1999.
- [6] O. V. Ekechukwu and B. Norton, "Review of solar-energy drying systems III: Low temperature air-heating solar collectors for crop drying applications," *Energy Conversion and Management*, vol. 40, no. 6, pp. 657–667, 1999.
- [7] I. Farkas, "Integrated use of solar energy crop drying," in *Proceedings of the European Drying Conference (EuroDrying '11)*, Palma de Mallorca, Spain, 2011.
- [8] H. R. Bolin and D. K. Salunkhe, "Food dehydration by solar energy," *Critical reviews in food science and nutrition*, vol. 16, no. 4, pp. 327–354, 1982.
- [9] M. A. Basunia and T. Abe, "Thin-layer solar drying characteristics of rough rice under natural convection," *Journal of Food Engineering*, vol. 47, no. 4, pp. 295–301, 2000.
- [10] T. M. DeJong, "Peach: peach crop yield and tree growth simulation model for research and education," in *Proceedings of the 5th International Symposium on Computer Modelling in Fruit Research and Orchard Management*, Wageningen, The Netherlands, October 1999.
- [11] P. Fellows, "Guidelines for small-scale fruit and vegetable processors," FAO Agricultural Services Bulletin 127, FAO of the United Nations, Rome, Italy, 1997.
- [12] G. Belforte, F. Dabbene, and P. Gay, "LPV approximation of distributed parameter systems in environmental modelling," *Environmental Modelling and Software*, vol. 20, no. 8, pp. 1063–1070, 2005.
- [13] G. S. McMaster, J. C. Ascough, D. A. Edmunds, A. A. Andales, L. Wagner, and F. Fox, "Multi-crop plant growth modeling for agricultural models and decision support systems," in *Proceedings of the International Congress on Modeling and Simulation Proceedings*, December 2005.
- [14] CropSyst, http://www.bsye.wsu.edu/cs_suite/cropsyst/.
- [15] C. O. Stöckle, M. Donatelli, and R. Nelson, "CropSyst, a cropping systems simulation model," *European Journal of Agronomy*, vol. 18, no. 3-4, pp. 289–307, 2003.
- [16] M. Condori and L. Saravia, "The performance of forced convection greenhouse driers," *Renewable Energy*, vol. 13, no. 4, pp. 453–469, 1998.
- [17] R. K. Goyal and G. N. Tiwari, "Parametric study of a reverse flat plate absorber cabinet dryer: a new concept," *Solar Energy*, vol. 60, no. 1, pp. 41–48, 1997.
- [18] D. Jain and G. N. Tiwari, "Thermal aspects of open sun drying of various crops," *Energy*, vol. 28, no. 1, pp. 37–54, 2003.
- [19] D. Jain and R. K. Jain, "Performance evaluation of an inclined multi-pass solar air heater with in-built thermal storage on deep-bed drying application," *Journal of Food Engineering*, vol. 65, no. 4, pp. 497–509, 2004.
- [20] D. Jain, "Modeling the system performance of multi-tray crop drying using an inclined multi-pass solar air heater with in-built thermal storage," *Journal of Food Engineering*, vol. 71, no. 1, pp. 44–54, 2005.
- [21] C. Ratti and A. S. Mujumdar, "Solar drying of foods: Modeling and numerical simulation," *Solar Energy*, vol. 60, no. 3-4, pp. 151–157, 1997.

- [22] M. S. Sodha, A. Dang, P. K. Bansal, and S. B. Sharman, "An analytical and experimental study of open sun drying and a cabinet tyre drier," *Energy Conversion and Management*, vol. 25, no. 3, pp. 263–271, 1985.
- [23] O. Yaldiz, C. Ertekin, and H. I. Uzun, "Mathematical modeling of thin layer solar drying of sultana grapes," *Energy*, vol. 26, no. 5, pp. 457–465, 2001.
- [24] A. Whiller, *Design Factors Influencing Solar Collectors, Low Temperature Engineering Application of Solar Energy*, American Society of Heating, Refrigerating and Airconditioning Engineers, New York, NY, USA, 1967.
- [25] J. A. Duffie and W. A. Beckman, *Solar Engineering and Thermal Process*, John Wiley and Son, New York, NY, USA, 2nd edition, 1991.
- [26] A. Iguaz and P. Virseda, "Moisture desorption isotherms of rough rice at high temperatures," *Journal of Food Engineering*, vol. 79, no. 3, pp. 794–802, 2007.
- [27] S. M. Henderson, "A basic concept of equilibrium moisture," *Agricultural Engineering*, vol. 33, pp. 29–32, 1952.
- [28] B. H. Khan, *Non Conventional Energy Sources*, Tata Mc-Graw Hills, 2nd edition, 2009.
- [29] N. Z. Al-Rawahi, Y. H. Zurigat, and N. A. Al-Azri, "Prediction of hourly solar radiation on horizontal and inclined surfaces for Muscat/Oman," *The Journal of Engineering Research*, vol. 8, no. 2, pp. 19–31, 2011.
- [30] F. Esquembre, "Easy Java Simulations: a software tool to create scientific simulations in Java," *Computer Physics Communications*, vol. 156, no. 2, pp. 199–204, 2004.
- [31] Easy Java Simulations, EJS, <http://fem.um.es/Ejs/>.
- [32] E. Hairer, S. P. Nørsett, and G. Wanner, *Solving Ordinary Differential Equations I: Nonstiff Problems*, vol. 8, Springer, Berlin, Germany, 2nd edition, 1993.
- [33] R. K. Goyal and G. N. Tiwari, "Effect of thermal storage on the performance of a deep bed drying system," *International Journal of Ambient Energy*, vol. 20, no. 3, pp. 125–136, 1999.
- [34] J. D. Aguilar, P. J. Perez, J. De la Casa, and C. Rus, "Cálculo de la energía generado por un sistema fotovoltaico conectado a red: Aplicación docente," Universidad de Jaén, 2006.

Research Article

Municipal Sewage Sludge Drying Treatment by an Composite Modifier

Na Wei

School of Civil Engineering and Architecture, Wuhan Polytechnic University, Wuhan 430023, China

Correspondence should be addressed to Na Wei, weina31@126.com

Received 16 December 2011; Revised 14 February 2012; Accepted 14 February 2012

Academic Editor: Zhijun Zhang

Copyright © 2012 Na Wei. This is an open access article distributed under the Creative Commons Attribution License, which permits unrestricted use, distribution, and reproduction in any medium, provided the original work is properly cited.

A sludge composite modifier (SCM) which comprises a mixture of three cementitious components was proposed for sludge drying and stabilization. Effect of SCM components on sludge moisture content was analyzed using uniform design and the optimum composition of SCM was determined by computer-aided modeling and optimization. To compare the drying effect of SCM, quicklime, and Portland cement, the effects of material content and curing time on moisture content of sludge were also studied. The results showed that the optimum ratio of modifier component was slag/cement clinker/dihydrate gypsum = 0.64/0.292/0.068 and the moisture content of SCM-stabilized sludge decreased with the increasing material content and extending curing time. Besides, the experimental results showed that optimized SCM behaved better than quicklime and Portland cement in sludge semi-drying and XRD analysis revealed that the main hydrated product of stabilization was ettringite, which played an important role in the effective drying process. Sewage sludge stabilized using SCM could be used as an effective landfill cover.

1. Introduction

Sewage sludge is the waste that remains after the treatment of municipal wastewater by wastewater treatment plants. The disposal of huge quantities of sewage sludge is a major environmental problem. This problem is especially significant in cities [1, 2]. In China, the annual production of moist sewage sludge was about 11 million tons in 2010 [3], and it is expected that wastewater treatment percentage will reach 75% by 2015, thus production of sewage sludge in China will continuously increase [4]. It is expected that sewage sludge disposal will be one of the most complex environmental problems facing the engineering in this field in China. In general, sludge that is discharged from treatment plants in the form of dehydrated cakes has a high water content of 75–85% and one sludge stabilization option is to dry it, which yields a solid that is low in humidity. This solid can be easily stored, recycled, or

transported to other facilities. Dried sewage sludge can be dumped in landfills, pyrolyzed, incinerated, or gasificated [5].

In recent years, conventional thermal drying and solar drying methods are usually adopted to dry sewage sludge. The typical thermal methods currently widely used to dry sludge include convection heat transfer of direct hot gas blasting and conduction heat transfer of steam inside screw and sludge [6]. Thermal drying is an efficient method that produces a biologically stable material with improved characteristics; however, the significant fuel consumption and potential emission of greenhouse gases (mainly CO₂) are important conditions [7]. Besides, Ulrich Luboschik [8] found that the operating costs of the solar drying system are competitive, but the characteristic feature of solar drying is the dependence on radiation intensity, which varies not only with daily cycle, but also with season and based on a year, approximately 750 kg water/m² ground space can be removed from the sludge. Mathioudakis et al. [9] reported the extended dewatering of sewage sludge in solar drying plants and found that during summer conditions, drying was completed within 7–12 days, but in autumn conditions the duration increased up to 32 days. Obviously, the conventional evaporative drying process may take long processing time, or involve high energy consumption.

On the other hand, many cementitious materials such as quicklime and cement have been used for sludge stabilization [10–13]. However, despite the fact that stabilization of sludge with cementitious materials has an extensive history of use, there exist few experimental studies for materials-based sludge drying as research is mainly oriented towards mechanical and sanitary properties of stabilized sludge. In addition, slag has received much attention as a cost-effective and efficient solidifying agent because of its cement-like characteristics and its abundance as a waste product from steel production plants. It is an economical material for sewage sludge stabilization and drying. Thus a sludge modifier (SCM) which comprises three kinds of cementitious materials (slag, cement clinker, and dihydrate gypsum) was proposed and optimized for more economical sludge drying and stabilization. Due to the complex components of SCM, it involves many parameters and complex interactions between them, the one-factor-at-a-time approach requires prohibitively large numbers of trials to systematically identify the drying effects of different components. In order to minimize the number of experimental trials in optimizing the sludge modifier formula, statistical and computational methods were proposed to be applied in this investigation. The uniform design is a new method established together by Wang et al. [14]. It is a fractional design which may be used when the underlying model between the response and factors is unknown or partially unknown. By uniform design method, the optimal proportion of SCM components was experimentally determined. Furthermore, the dewatering ability of SCM was investigated and compared with quicklime and Portland cement to examine the feasibility of its utilization as a drier in the context of economical drying process of sludge.

2. Experiment and Results

2.1. Materials

The sewage sludge used was obtained from the Wastewater Treatment Plant of Hanxi, Wuhan city. The main characteristics of sludge are listed in Table 1. The chemical compositions of quicklime, Portland cement, slag, cement clinker, and dihydrate gypsum are listed in Table 2.

Table 1: Main characteristics of the sewage sludge.

Moisture (%)	Density (g/cm ³)	PH	Organic matter (%)
80.87	1.04	7.07	60.20

Table 2: Chemical composition of quicklime, Portland cement, slag, cement clinker, and dihydrate gypsum (wt%).

	CaO	SiO ₂	Al ₂ O ₃	Fe ₂ O ₃	SO ₃	MgO
Quicklime	81.12	3.70	0.49	0.09	0.04	0.01
Portland cement	59.82	24.13	6.35	3.57	2.24	0.98
Slag	37.68	30.46	14.95	1.12	1.95	9.9
Cement clinker	63.83	21.48	4.72	3.63	0.67	3.70
Dihydrate gypsum	42.87	4.2	0.25	0.05	44.22	1.17

2.2. Sample Preparation and Measurement

Sludge samples in wet conditions were mixed with materials (quicklime, Portland cement, and SCM, resp.) and the mixtures were cured at room temperature for various periods. The mixing procedures are as follows: the wet sludge was placed in a mixer first, materials with a designed content were then added and the mixture stirred for 30 min. After homogenization, mixtures were placed into open containers and cured at room temperature. Representative samples were collected from each mixture at specific time intervals, that is, 3 h, 1, 3, 7, and 14 d, and were analyzed for the measurement of the moisture content on wet basis. The values of moisture content reported are the average of three specimens of each stabilized mixtures.

2.3. SCM Prescription Experiment

The influence of SCM components on stabilized sludge moisture content and the optimum proportion of SCM components were investigated with uniform recipe design method. In this study, samples were prepared by mixing wet sewage sludge and three SCM components in various ratios and all mixtures were stabilized for a period of 3 h. The property is the moisture content of stabilized mixtures, denoted by Y (%) and factors involved are proportions of sludge (x_1), slag (x_2), cement clinker (x_3), and dihydrate gypsum (x_4). The proper ranges of factors, obtained by previous experiments, were

$$0.5 \leq x_1 \leq 0.99, \quad 0.004 \leq x_2 \leq 0.45, \quad 0.0005 \leq x_3 \leq 0.275, \quad 0.0005 \leq x_4 \leq 0.27. \quad (2.1)$$

The selections of these ranges are based on technical and/or economical reasons. Then the uniform design table and corresponding experimental scheme were obtained by the conditional probability distribution method [15]. The obtained uniform design table, together with the experimental scheme and results are listed in Table 3.

Furthermore, the optimum formula of SCM was determined by corresponding mathematical modeling and optimization. We used this optimized SCM in subsequent sludge drying experiments.

Table 3: Uniform design table and experimental scheme and results.

No	No. of columns			Factors				Y (%)
	1	2	3	x_1	x_2	x_3	x_4	
1	11	8	7	0.6070	0.0435	0.1624	0.1871	41.31
2	7	16	6	0.5144	0.1004	0.1458	0.2394	31.95
3	14	15	12	0.7027	0.0818	0.1727	0.0428	48.71
4	6	9	13	0.5749	0.0105	0.1145	0.3001	41.54
5	16	10	9	0.6817	0.0992	0.1201	0.0990	47.59
6	1	7	5	0.5012	0.0641	0.1385	0.2963	32.91
7	15	3	4	0.7729	0.0168	0.1309	0.0795	57.15
8	8	5	1	0.7022	0.0331	0.1453	0.1194	49.84
9	10	1	11	0.7599	0.1280	0.0512	0.0608	52.77
10	9	12	16	0.6472	0.0228	0.1667	0.1633	45.88
11	4	11	3	0.8052	0.0930	0.0931	0.0087	58.39
12	3	4	15	0.7352	0.0933	0.0307	0.1408	49.42
13	2	14	10	0.6752	0.1279	0.1715	0.0254	43.24
14	5	2	8	0.5280	0.0652	0.0720	0.3348	36.33
15	13	6	14	0.5070	0.0932	0.1478	0.2520	32.17
16	12	13	2	0.7165	0.0605	0.0105	0.2124	52.55

2.4. Sludge Drying Experiments

To evaluate the changes in sludge moisture content caused by SCM in relation to its content and duration of stabilization process, mixtures of sludge-SCM were prepared with different SCM contents and cured for different periods. Meanwhile, quicklime and Portland cement, as conventional binder, were used for comparison and sludge-quicklime and sludge-Portland cement samples were prepared similarly.

Here, materials content, which was defined as weight percentage of materials in sludge-material mixture, and curing time were the two considered factors. Various material content and curing time, respectively, ranging from 5% to 60% and 3 h to 14 d, were examined.

2.5. X-Ray Diffraction Analysis of Hydration Products of SCM

XRD was performed to identify and quantify the crystalline mineral phases present in the SCM hydration products. For this purpose, pure SCM pastes (without the addition of sludge) were prepared with a water/SCM ratio of 0.56 by weight. The pastes were analyzed with an X-ray diffractometer (Philip, PE Model 1729) using Cu Ka radiation.

2.6. SEM Analysis

SEM analysis was performed on raw sludge and the modifier-dried sludge sample with SCM. The samples were gilt with Au and SEM was operated at 20 kV of acceleration voltage.

Table 4: The verification experiments and results.

No	x_1	x_2	x_3	x_4	Y (%)	Y' (%)	$ \Delta Y $ (%)
17	0.6	0.1	0.16	0.14	37.57	37.25	0.32
18	0.7	0.1	0.12	0.08	45.95	46.57	0.62
19	0.8	0.12	0.04	0.04	55.86	56.14	0.54
20	0.9	0.05	0.025	0.025	68.20	68.81	0.61

3. Discussions

3.1. Ratio of SCM Components Optimization

Results of uniform design scheme were analyzed using second-order polynomial stepwise regression analysis. The obtained equation, together with its significance level (P) and correlation coefficient after adjustment (Ra) are given in (3.1). Analyzed by F -test method, (3.1) is intensively significant. Furthermore, the validity of (3.1) was assessed experimentally and the results (Table 4) showed that the predicted value (Y) was close to the experimental result (Y'). Then, combing the results of uniform design and verification experiment, a similar regression analysis was made to improve veracity of model prediction. The results obtained are given in (3.2)

$$Y = -0.1656 + 0.9483x_1 - 2.2063x_2^2 + 0.3486x_4^2 \quad (3.1)$$

$$(P = 0.0001, Ra = 0.9952),$$

$$Y = 0.2669 - 0.5329x_2 + 0.5568x_1^2 - 0.3344x_3^2 - 0.8734x_3 \times x_4 \quad (3.2)$$

$$(P = 0.0001, Ra = 0.9977).$$

Thus, the final regression model between Y and x_i ($i = 1, 2, 3, 4$) can be expressed by (3.2). The model optimization step is to find $x_1^*, x_2^*, x_3^*, x_4^*$ such that

$$Y^* = Y^*(x_1^*, x_2^*, x_3^*, x_4^*) = \min Y(x_1, x_2, x_3, x_4), \quad (3.3)$$

$$0.5 \leq x_1 \leq 0.99, \quad 0.004 \leq x_2 \leq 0.45, \quad 0.0005 \leq x_3 \leq 0.275, \quad 0.0005 \leq x_4 \leq 0.27,$$

where $Y^*(x_1^*, x_2^*, x_3^*, x_4^*) = Y^*$ is given by (3.2). Here, Simulated Annealing method was used to optimize the model and determine the optimum ratio of SCM components. The result indicated that sludge moisture content exhibited its lowest value at the weight ratio of slag to cement clinker to dihydrate gypsum of 0.64 : 0.292 : 0.068.

3.2. Influence of Material Content on Stabilized Sludge Moisture Content

Figure 1 shows that SCM is more effective than Portland cement and compared with quicklime, SCM is more effective in sludge drying at a lower content (<50 wt%), whereas quicklime behaves better at higher content. This is probably caused by different physical-chemical interactions involved in different sludge-material systems.

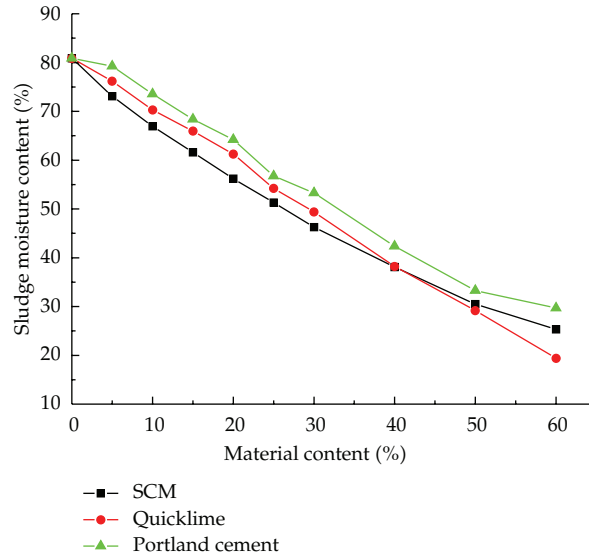
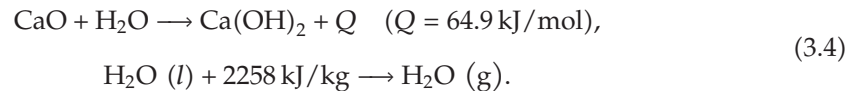


Figure 1: Moisture content of stabilized sludge cured for 3 h as a function of material content.

For Portland cement, the hydration reactions between SCM components and free water in sludge are responsible for the sludge drying and stabilization. The hydration product of Portland cement is C-S-H gel and a spot of ettringite ($3\text{CaO}\cdot\text{Al}_2\text{O}_3\cdot 3\text{CaSO}_4\cdot 32\text{H}_2\text{O}$, abbreviated as Aft), which can convert some free water in sludge into crystal water. However the amount of hydration products was few and the free water being converted was few due to the slow hydration rate of Portland cement. This is the reason why Portland cement has poor drying effect. Thus three kinds of cementitious components were chosen to speed the hydration rate and the formation of C-S-H gel especially Aft. Thus, the sludge moisture content decreases with the increase of SCM content; however, when the modifier content is relatively high, the tendency of decrease slows down because the amount of free water in sludge is limited.

For quicklime, sludge drying is attributed to both chemical reaction and physical evaporation. The reactions are expressed, respectively, in



From (3.4), 1 g CaO consumes 0.32 g water, while the amount of water evaporated by hydration heat is 0.51 g. Thus, physical evaporation is the main mechanism for quicklime-based sludge drying. This is the reason why the moisture content of quicklime-stabilized sludge decreases obviously with the quicklime content.

It can be seen that the SCM is more suitable for sludge semi-drying treatment, while the quicklime can be used for sludge-drying treatment. Obviously, the increase of materials content will increase the total quantity of sludge. Thus it will increase the treatment cost of the sludge disposal and it is not economical in industry to use such a large amount of quicklime.

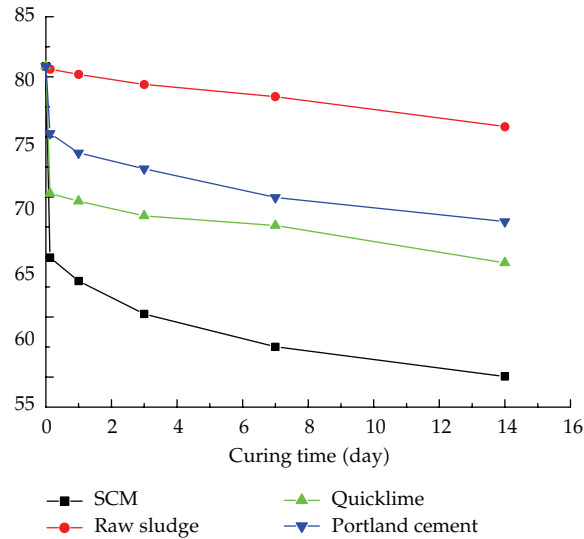


Figure 2: Moisture content of raw sludge and stabilized sludge (10 wt% material) versus curing time.

3.3. Influence of Curing Time on Stabilized Sludge Moisture Content

As shown in Figure 2, moisture content of raw sludge and both three stabilized samples decreased with the duration of stabilizing process. Here the three stabilized mixtures of sludge-SCM, sludge-quicklime, and sludge-Portland cement were prepared with a same content of 10%.

Obviously the drop of raw sludge moisture content, a relative slower one, is attributed to air-based water evaporation. For all three materials, the moisture content of stabilized mixtures drops fast at early ages (3 h), and then gradually slow at later ages. But compared with quicklime-added samples, the later reduction in moisture content of SCM-added sample is more significant, which may be due to further hydration of SCM and correspondingly the continuous chemical binding of free water in sludge.

Thus, for quicklime, sludge drying only depends on the physical evaporation, while for SCM, sludge drying depends on both physical evaporation and hydration reactions between modifier components and free water.

3.4. Analysis of SCM Hydration Products

From XRD patterns of SCM pastes shown in Figure 3, it can be seen that after 1 day of curing, ettringite ($3\text{CaO}\cdot\text{Al}_2\text{O}_3\cdot 3\text{CaSO}_4\cdot 32\text{H}_2\text{O}$, abbreviated as AFt) phase and calcium silicate hydrate ($\text{CaO}\cdot\text{SiO}_2\cdot n\text{H}_2\text{O}$, briefed as C-S-H) phase had been formed and AFt was the major hydration product. When it extended to 3 days of hydration, the major peaks of AFt and C-S-H became stronger.

Ettringite is a mineral which rarely occurs in nature but is widely present in the mineralogy of hydrated cements. Water is especially important to ettringite because of the high water content of the solid, which has the constitution, $3\text{CaO}\cdot\text{Al}_2\text{O}_3\cdot 3\text{CaSO}_4\cdot 32\text{H}_2\text{O}$. With a higher water content of about 46% in ettringite, it can convert more free water in sludge into crystal water. Therefore, from the XRD analysis, it can be inferred that the formation of AFt

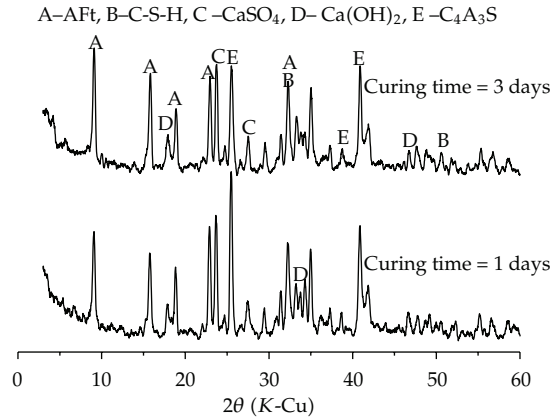


Figure 3: XRD pattern of SCM after hydration for 1 and 3 days.

plays an important part for the sludge drying. Besides, it can be concluded that the combined use of slag/cement clinker/dihydrate gypsum, together with their proportion optimization, promotes the appearance of AFt and in turn leads to the dramatic moisture content reduction.

3.5. SEM Analysis

SEM observations of raw sewage sludge and the dried sludge with SCM are shown in Figure 4. As shown in Figure 4(a), the platy construction of raw sewage sludge is disordered and incompact. What is more, the raw sewage sludge exhibited a poor structure with a rough and granular texture with a large amount of open porosity. Figure 4(b) shows that large amounts of hydration products (AFt and C-S-H) cover on the surface of sludge particles, and the particles aggregate together due to agglutination caused by the formation of crystal structure of AFt and C-S-H. It reveals that the addition of SCM and the mixing procedure resulted in a dense and homogeneous microstructure with less porosity. It may be the reason why the porosity ratio and water content of the dried sludge declines significantly.

The SEM analysis of raw sludge and stabilized sludge also confirmed that the combined use of slag, cement clinker, and dihydrate gypsum, together with their proportion optimization, promoted the appearance of AFt and in turn led to the dramatic moisture content reduction. Thus, both sludge drying and stabilization process took place through the speedy formation of AFt and calcium silicate hydrate, converting most free water of sludge into crystal water.

4. Conclusions

The following conclusions can be drawn from this investigation.

- (1) A composite modifier is proposed for sludge drying and stabilization. The experimentally optimized mix ratio of slag to cement clinker to dihydrate gypsum of 0.64:0.292:0.068.
- (2) The moisture content of SCM-added sludge decreases with the increasing of SCM content and the extending curing time. However, with the further increase of SCM

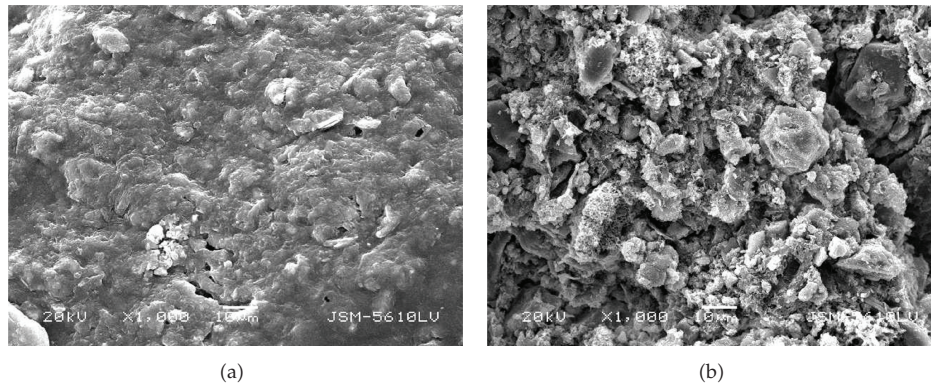


Figure 4: SEM micrographs of sludge: (a) raw sewage sludge and (b) dried sludge after 3 days of curing.

content and extending of curing time, the tendency of decrease slows down, due to the limited free water in sludge.

- (3) Comparing with Portland cement, SCM shows better drying effect. Besides, the comparative experiment with SCM and quicklime reveals that SCM is more effective for semi-drying treatment of sludge, in which 40–60% water content was achieved.
- (4) XRD analysis and SEM analysis of SCM hydration products demonstrated that combined use of slag, cement clinker, dihydrate gypsum, together with their mixing ratio optimization, result in a quick formation of Aft, which may play an important role in sludge drying and stabilization.

Acknowledgment

This research has been supported by the Introduced Talent Support Project of Wuhan Polytechnic University, China (Project no. 2010RZ08).

References

- [1] D. Gavaldà, J. D. Scheiner, J. C. Revel et al., "Agronomic and environmental impacts of a single application of heat-dried sludge on an Alfisol," *Science of the Total Environment*, vol. 343, no. 1–3, pp. 97–109, 2005.
- [2] U. Song and E. J. Lee, "Environmental and economical assessment of sewage sludge compost application on soil and plants in a landfill," *Resources, Conservation and Recycling*, vol. 54, no. 12, pp. 1109–1116, 2010.
- [3] Q. H. Lin, H. Cheng, and G. Y. Chen, "Preparation and characterization of carbonaceous adsorbents from sewage sludge using a pilot-scale microwave heating equipment," *Journal of Analytical and Applied Pyrolysis*, vol. 93, pp. 113–119, 2012.
- [4] W. Y. Deng, J. H. Yan, X. D. Li et al., "Measurement and simulation of the contact drying of sewage sludge in a Nara-type paddle dryer," *Chemical Engineering Science*, vol. 64, no. 24, pp. 5117–5124, 2009.
- [5] J. W. Judex, M. Gaiffi, and H. C. Burgbacher, "Gasification of dried sewage sludge: status of the demonstration and the pilot plant," *Waste Management*, vol. 32, no. 4, pp. 719–723, 2012.
- [6] T. I. Ohm, J. S. Chae, K. S. Lim, and S. H. Moon, "The evaporative drying of sludge by immersion in hot oil: effects of oil type and temperature," *Journal of Hazardous Materials*, vol. 178, no. 1–3, pp. 483–488, 2010.

- [7] D. Kalderis, M. Aivalioti, and E. Gidaracos, "Options for sustainable sewage sludge management in small wastewater treatment plants on islands: the case of crete," *Desalination*, vol. 260, no. 1–3, pp. 211–217, 2010.
- [8] U. Luboschik, "Solar sludge drying-based on the IST process," *Renewable Energy*, vol. 16, no. 1–4, pp. 785–788, 1999.
- [9] V. L. Mathioudakis, A. G. Kapagiannidis, E. Athanasoulia, V. I. Diamantis, P. Melidis, and A. Aivasidis, "Extended dewatering of sewage sludge in solar drying plants," *Desalination*, vol. 248, no. 1–3, pp. 733–739, 2009.
- [10] S. Valls and E. Vázquez, "Stabilization and solidification of sewage sludges with Portland cement," *Cement and Concrete Research*, vol. 30, no. 10, pp. 1671–1678, 2000.
- [11] O. Malliou, M. Katsioti, A. Georgiadis, and A. Katsiri, "Properties of stabilized/solidified admixtures of cement and sewage sludge," *Cement and Concrete Composites*, vol. 29, no. 1, pp. 55–61, 2007.
- [12] E. H. Kim, J. K. Cho, and S. Yim, "Digested sewage sludge solidification by converter slag for landfill cover," *Chemosphere*, vol. 59, no. 3, pp. 387–395, 2005.
- [13] S. Capizzi-Banas, M. Deloge, M. Remy, and J. Schwartzbrod, "Liming as an advanced treatment for sludge sanitisation: helminth eggs elimination—ascaris eggs as model," *Water Research*, vol. 38, no. 14–15, pp. 3251–3258, 2004.
- [14] Z. Wang, D. Luo, and C. Ena, "Optimization of polysaccharides extraction from *Gynostemma pentaphyllum* Makino using Uniform Design," *Carbohydrate Polymers*, vol. 69, no. 2, pp. 311–317, 2007.
- [15] Q. Y. Tang and M. G. Feng, *Practical Statistics and DPS Data Processing System*, Agricultural Press, Beijing, China, 1997.

Research Article

Thin-Layer Drying Characteristics and Modeling of Chinese Jujubes

**Xiao-Kang Yi,^{1,2} Wen-Fu Wu,¹ Ya-Qiu Zhang,¹
Jun-Xing Li,³ and Hua-Ping Luo²**

¹ College of Biological and Agricultural Engineering, Jilin University, Changchun 130022, China

² College of Mechanical and Electronic Engineering, Tarim University, Alar 843300, China

³ Institute of Grain Machinery Research, Jilin Academy of Agricultural Machinery, Changchun 130022, China

Correspondence should be addressed to Wen-Fu Wu, wwfzlb@163.com

Received 8 December 2011; Accepted 31 January 2012

Academic Editor: Zhijun Zhang

Copyright © 2012 Xiao-Kang Yi et al. This is an open access article distributed under the Creative Commons Attribution License, which permits unrestricted use, distribution, and reproduction in any medium, provided the original work is properly cited.

A mathematical modeling of thin-layer drying of jujubes in a convective dryer was established under controlled conditions of temperature and velocity. The drying process took place both in the accelerating rate and falling rate period. We observed that higher temperature reduced the drying time, indicating higher drying rates of jujubes. The experimental drying data of jujubes were used to fit ten different thin-layer models, then drying rate constants and coefficients of models tested were determined by nonlinear regression analysis using the Statistical Computer Program. As for all the drying models, the Weibull distribution model was superior and best predicted the experimental values. Therefore, this model can be used to facilitate dryer design and promote efficient dryer operation by simulation and optimization of the drying processes. The volumetric shrinkable coefficient of jujubes decreased as the drying air temperature increased.

1. Introduction

Jujube (*Zizyphus jujuba* Mill.) is a characterized Chinese fruit, whose cultivation area has reached more than 1.5 million hectares in China. Moreover, a lot of products are processed from jujubes, such as candied and drunk jujubes, and jujube tea, juice, and sugar. The vast majority of jujubes are dried and sold at home and abroad, except that a small proportion are reserved for fresh eating [1]. Jujubes play an important role in human nutrition as sources of sugar, vitamins, protein, and minerals [2]. For thousands of years, besides been used as food, jujube has been commonly used in traditional Chinese medicine. Jujubes tend to spoil because of their high moisture contents, which result in the production losses of 25–30% after harvest

[3]. Drying is one of the widely used methods for postharvest preservation of agricultural products. It is used to decrease considerable moisture content, reduce microbiological activity, and enable storability of the product under ambient temperatures [4, 5]. Dried food has longer shelf life in packages and lower transportation, handling, and storage costs [6].

Drying is a complicated process relating to simultaneous heat and mass transfer where water is transferred by diffusion from inside the food material to the air-food interface and from the interface to the air stream by convection [7, 8]. The amount of energy required to dry a product depends on many factors, such as initial moisture, desired final moisture, and drying air temperature and velocity [9]. Thin layer drying means to dry as one layer of sample particles or slices. Thin layer drying equations have been used for drying time prediction for generalization of drying curves [10]. Various mathematical models describing the drying characteristics of different fruits and vegetables have been proposed to optimize the drying process and design efficient dryers [11, 12]. There are many studies on the drying of fruits and vegetables, such as apricot [13], banana [14], carrot [15], fig [16], golden apples, grape [17], green pepper, stuffed pepper, green bean [18], litchi [19], mushroom, pistachio [20], onion [21], and pumpkin [22]. Several researchers have investigated the drying kinetics of various agricultural products in order to evaluate the Weibull distribution model for describing the thin-layer drying characteristics [23, 24]. In addition, some researchers proposed the drying properties and processing technologies of jujubes [25–28]. The Henderson and Pabis model (see Table 2) has been applied in the drying of jujubes [29]; however, although this model may describe the drying curve for the specific experiments conditions, it cannot give a clear and accurate view of the important processes during drying.

The objectives of this study are (1) to determine the effect of air temperature and air velocity on the drying of jujube and to obtain drying curves; (2) to establish a mathematical model for predicting the thin layer drying characteristics of convection drying of jujubes at different drying air temperature and velocity conditions.

2. Materials and Methods

2.1. Materials

Bioer jujube is one of the main Chinese jujubes varieties, which mainly grow in Shanxi and Xinjiang Province. Bioer jujubes used in the experiments were produced in Alar city, Xinjiang province and were chosen as drying materials in September, 2010. The appearances of jujubes were presented in Figure 1. The samples in the same species with full maturity and uniform size were stored in a refrigerator at 4°C before starting the experiments. The initial moisture content was about 70.12% wet basis (w.b.).

2.2. The Laboratory Dryer

The drying experiments were carried out by a laboratory dryer (BG-II) manufactured at College of Biological and Agricultural Engineering, Jilin University, Changchun city, Jilin province. A schematic view of the experimental arrangement was shown in Figure 2.

The overall dimensions of the dryer are $2.2 \times 0.6 \times 1.8$ m and it mainly consisted of a fan, electrical heater, drying chamber, and temperature and humidity control unit. The favourable drying air velocity provided by the fan could be changed by the electrical motor without level. A 0–15 m/s range anemometer (LUTRON, AM-4201, Taiwan) measured the



Figure 1: The appearances of jujubes: (a) fresh jujubes; (b) dry jujubes.

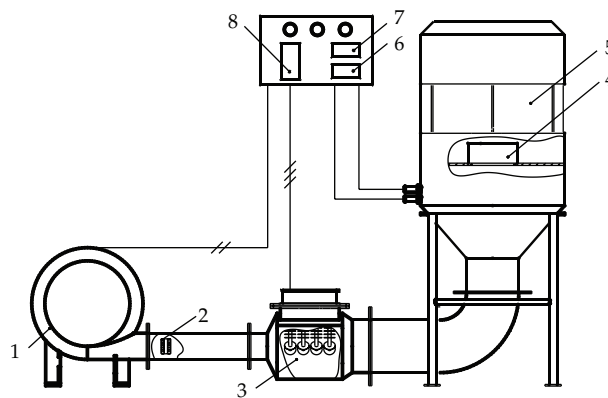


Figure 2: Schematic view of the experimental arrangements. 1: Fan; 2: Diffuser; 3: Heater; 4: Bucket; 5: Drying chamber; 6: Humidity control unit; 7: Temperature control unit; 8: Variator.

velocity of air passing through the system. The drying air temperature was automatically controlled by regulating the required voltage to the heaters inside the air channel. The heater consisted of four groups of resistance wires of 1,000 W, and each group could be used independently to control the temperature (30–110°C, dry bulb temperature) of air and in drying chamber. The dry bulb temperature inside the drying chamber was measured and controlled with an accuracy of $\pm 0.1^\circ\text{C}$ using a Pt 100, 1/10 DIN, thermometer inserted in the middle position of the inlet cross-section. Temperature-humidity sensor (GALLTEC, TFK80J, Germany) was used to measure the relative humidity with an accuracy of $\pm 3\% \text{Rh}$. Resistance wires were on and off by the control unit based on temperature change to maintain adjusted temperature at the same level during the experiments. A digital electronic balance (OHAUS, CP3102, USA) in the measurement range of 0–3100 g and an accuracy of 0.01 g was used for the moisture loss of samples.

2.3. Drying Procedures

Drying experiments were carried out at different drying temperatures of 45, 55, and 65°C and different velocities of 0.5, 1.0, and 2.0 m/s. The drying air temperature was automatically controlled at $\pm 1^\circ\text{C}$ by regulating an electrical heating device and the air velocity was measured by an anemometer at precision of 0.1%.

Table 1: Uncertainties of the parameters during drying of jujubes.

Parameter	Unit	Comment
Fan inlet temperature	°C	±0.5
Heater outlet temperature	°C	±0.5
Drying chamber inlet temperature	°C	±0.3
Drying chamber outlet temperature	°C	±0.3
Ambient air temperature	°C	±0.3
Inlet of fan with dry and wet thermometers	°C	±0.5
Mass loss values	min	±0.1
Temperature values	min	±0.1
Uncertainty in the mass loss measurement	g	±0.5
Uncertainty in the air velocity measurement	m/s	±0.14
Uncertainty of the measurement of relative humidity of air	RH	±0.1
Uncertainty in the measurement of moisture quantity	g	±0.001
Uncertainty in reading values of table (ρ , cp.)	%	±0.1-0.2

The dryer took some time to reach the desired value after starting up. Approximately 200 g of samples were put into a stainless-steel mesh bucket of 200 mm diameter, and then they were put into the dryer after weighting. In all the experiments, samples were kept the same thickness and tiled into the layers. The weighing interval of the drying samples was 1 h during the drying process. Since the weighing process only took a few seconds, no considerable disturbances were imposed. According to the standards set by General Administration of Quality Supervision, Inspection and Quarantine (AQSIQ) [30], the drying process was continued until the moisture content of the samples reached below 25% (w.b.). After the drying experiments, the samples were put into an electric constant temperature blower oven, maintaining at $105 \pm 2^\circ\text{C}$ until their weight remained unchanged. This weight was used to calculate the moisture content of the samples.

2.4. Experimental Uncertainty

Errors and uncertainties in experiments can arise from instrument selection, condition, calibration, environment, observation, reading, and test planning [31]. In the drying experiments of jujubes, the temperatures, velocity of drying air, and weight losses were measured with appropriate instruments. During the measurements of the parameters, the uncertainties occurred were presented in Table 1.

2.5. Theoretical Considerations and Mathematical Formulation

Moisture contents of jujubes during thin layer drying experiments were expressed in dimensionless form as moisture ratios MR with the following equation [32, 33]:

$$\text{MR} = \frac{(M - M_e)}{(M_0 - M_e)}, \quad (2.1)$$

Table 2: Mathematical models applied to the moisture ratio values.

Eq. no.	Model name	Model equation	References
(2.1)	Lewis	$MR = \exp(-kt)$	[47]
(2.2)	Page	$MR = \exp(-kt^n)$	[48]
(2.3)	Modified Page	$MR = \alpha \exp[-(kt^n)]$	[49]
(2.4)	Overhults	$MR = \exp[-(kt)^n]$	[50]
(2.5)	Henderson and Pabis	$MR = \alpha \exp(-kt)$	[51]
(3.1)	Logarithmic	$MR = \alpha \exp(-kt) + c$	[39]
(3.2)	Two term exponential	$MR = \alpha \exp(-kt) + b \exp(-k_1t)$	[52]
(3.3)	Wang and Singh	$MR = 1 + \alpha t + \beta t^2$	[49]
(3.4)	Thompson	$t = \alpha \ln(MR) + \beta \ln(MR)^2$	[53]
(3.5)	Weibull distribution	$MR = \alpha - b \exp[-(kt^n)]$	[54]

M is the mean jujubes moisture content, M_0 is the initial value, and M_e is the equilibrium moisture content. The drying rates of jujubes were calculated by using (2.2) [34, 35]

$$\text{Drying rate} = \frac{M_{t+\Delta t} - M_t}{\Delta t}. \quad (2.2)$$

M_t and $M_{t+\Delta t}$ are the moisture content at t and moisture content at $t + \Delta t$ (kg water/kg dry matter), respectively, t is the drying time (h).

Convection drying of fruits occurs in the falling rate drying period, thus the well-known semiempirical and empirical models could be applied to the drying data. To select a suitable model for describing the drying process of jujubes, drying curves were fitted with 10 thin-layer drying moisture ratio models (Table 2). During the analysis of mathematical drying models, it was assumed that materials contained the same initial moisture content; there was no heat loss with insulation of dryer walls; material internal temperature gradient, drying air humidity, and heat transfer between materials and volume contraction rate during drying were negligible.

The regression analysis was performed with the STATISTICA computer program developed by Statistical Package for Social Science (SPSS) 18. The coefficient of determination R^2 was one of the primary criteria when selecting the best equation to account for variation in the drying curves of dried samples [36–38]. In addition, the goodness of fit was determined by various statistical parameters such as reduced chi-square, χ^2 mean bias error and root mean square error (RMSE). For a qualified fit, R^2 should be high while χ^2 and RMSE are low [39, 40]. These statistical values are calculated as follows:

$$R^2 = 1 - \frac{\sum_{i=1}^n (MR_{i,\text{pre}} - MR_{i,\text{exp}})^2}{\sum_{i=1}^n (MR_{i,\text{exp}} - MR_{i,\text{pre,mean}})^2}, \quad (2.3)$$

$$\chi^2 = \frac{\sum_{i=1}^N (MR_{\text{exp},i} - MR_{\text{pre},i})^2}{N - z}, \quad (2.4)$$

$$\text{RMSE} = \sqrt{\frac{\sum_{i=1}^n (MR_{i,\text{pre}} - MR_{i,\text{exp}})^2}{N}}. \quad (2.5)$$

$MR_{exp,t}$ is the i th experimental moisture ratio, $MR_{pre,i}$ is the i th predicted moisture ratio, N is the number of observations, and z is the number of constants in the drying model.

3. Results and Discussion

3.1. Drying Characteristics of Jujubes

The changes in moisture ratios with time for different drying air temperatures are shown in Figure 3. The final moisture content of samples dried under different conditions ranged from 28% to 25% (w.b.). The drying rate is higher for higher air temperature. As a result, the time taken to reach the final moisture content is less, as shown in Figure 3. Therefore, the drying air temperature has an important effect on the drying of jujubes. The changes of the moisture ratios at different air velocities (0.5, 1.0 and 2.0 m/s) under each air temperature (45, 55, and 65°C) were shown in Figure 4. The data revealed that the drying air velocities had little effect on the drying process. Similar results have been reported for plum [41], rosehip [42].

3.2. Drying Rate of Jujubes

The changes in the drying rates with moisture content for different drying air temperatures and velocities are shown in Figures 5 and 6. It is apparent that the drying process involved two periods, accelerating period and falling period, without a constant-rate drying period. At the beginning of the drying process, the drying rate increases rapidly with decreasing moisture content and reaches the maximum. Then drying rate decreases continuously with decreasing moisture content, and the drying operations are seen to occur in the falling rate period. It was also noted the predominant direct effect of air temperature on the drying rate, as clearly shown in the figures for all temperatures. Due to the fact that the relative humidity of the drying air at a higher temperature was less compared to that at a lower temperature, the difference in the partial vapor pressure between the radishes and their surroundings was greater for the higher temperature drying environment [43]. The data revealed that the drying air velocities had little effect on the drying rate. These results are in agreement with the previous works [31, 44].

3.3. Mathematical Modelling of Thin-Layer Drying

The mathematical drying models were based on the experimental moisture contents and dry weights. Then continuous data were obtained at different drying air temperatures and velocities and they were converted into moisture ratios and fitted over drying time. According to the statistical results of the determination coefficient R^2 , chi-square (χ^2), and RMSE, ten thin-layer drying models were compared and shown in Table 3. The data showed that the highest coefficient (R^2), and the lowest chi-square (χ^2) and RMSE were obtained with the Weibull distribution model. Consequently, it could be concluded that the Weibull distribution model could sufficiently define the thin layer drying of jujubes. The model could be expressed in the following equation:

$$MR = a - b \exp[-(kt^n)]. \quad (3.1)$$

Table 3: Statistical results of 10 models at different drying conditions.

Model	Drying air velocity (m/s)	Drying air temperature (°C)								
		45		55		65				
		R^2	χ^2	RMSE	R^2	χ^2	RMSE	R^2	χ^2	RMSE
Lewis	0.5	0.999383	0.000036	0.005982	0.996556	0.000207	0.014172	0.995002	0.000303	0.016965
	1.0	0.996838	0.000192	0.013757	0.995763	0.000253	0.015644	0.982534	0.000854	0.028524
	2.0	0.993384	0.000431	0.020594	0.995183	0.000294	0.016885	0.999249	0.000042	0.006356
Page	0.5	0.999835	0.000010	0.003099	0.999336	0.000041	0.006223	0.998104	0.000121	0.010450
	1.0	0.997864	0.000132	0.011306	0.999782	0.000013	0.003547	0.992789	0.000371	0.018327
	2.0	0.998801	0.000079	0.008765	0.999893	0.000007	0.002516	0.999265	0.000043	0.006291
Modified Page	0.5	0.999835	0.000010	0.003091	0.999433	0.000036	0.005751	0.998495	0.000102	0.009311
	1.0	0.999847	0.000010	0.003024	0.999929	0.000005	0.002025	0.996819	0.000173	0.012172
	2.0	0.999355	0.000044	0.006429	0.999934	0.000004	0.001983	0.999305	0.000043	0.006116
Overhults	0.5	0.999835	0.000010	0.003099	0.999336	0.000041	0.006223	0.998104	0.000121	0.010450
	1.0	0.997864	0.000132	0.011306	0.999782	0.000013	0.003547	0.992789	0.000371	0.018327
	2.0	0.998801	0.000079	0.008756	0.999893	0.000007	0.002516	0.999265	0.000043	0.006291
Henderson and Pabis	0.5	0.999689	0.000019	0.004249	0.999068	0.000058	0.007371	0.998404	0.000102	0.009588
	1.0	0.996848	0.000195	0.013735	0.998067	0.000119	0.010567	0.986812	0.000679	0.024785
	2.0	0.995737	0.000283	0.016531	0.998223	0.000112	0.010256	0.999250	0.000044	0.006355
Logarithmic	0.5	0.999739	0.000016	0.003892	0.999441	0.000036	0.005707	0.998589	0.000096	0.009015
	1.0	0.999721	0.000018	0.004083	0.999823	0.000011	0.003196	0.993283	0.000365	0.017688
	2.0	0.999929	0.000005	0.002137	0.999703	0.000019	0.004193	0.999301	0.000043	0.006134
Two-term exponential	0.5	0.999689	0.000020	0.004249	0.999068	0.000062	0.007371	0.998404	0.000115	0.009588
	1.0	0.996848	0.000202	0.013735	0.998067	0.000128	0.010567	0.997733	0.000130	0.010276
	2.0	0.995737	0.000293	0.016531	0.998223	0.000120	0.010256	0.999304	0.000045	0.006122
Wang and Singh	0.5	0.998691	0.000079	0.008711	0.998516	0.000092	0.009304	0.996917	0.000197	0.013324
	1.0	0.995748	0.000263	0.015952	0.999753	0.000263	0.003775	0.970316	0.001528	0.037185
	2.0	0.998902	0.000073	0.008388	0.999889	0.000007	0.002565	0.995006	0.000030	0.016395
Thompson	0.5	0.999326	0.157846	0.389583	0.999528	0.045533	0.026818	0.998947	0.038918	0.187152
	1.0	0.999568	0.138582	0.366112	0.999774	0.019316	0.134424	0.994631	0.217603	0.443711
	2.0	0.999771	0.071202	0.262351	0.999367	0.057569	0.232317	0.999557	0.025016	0.151707
Weibull distribution	0.5	0.999926	0.000005	0.002076	0.999454	0.000032	0.005643	0.998643	0.000098	0.008839
	1.0	0.999939	0.000004	0.001916	0.999960	0.000003	0.001523	0.997498	0.000144	0.010796
	2.0	0.999943	0.000004	0.001911	0.999935	0.000004	0.001962	0.999306	0.000044	0.006113

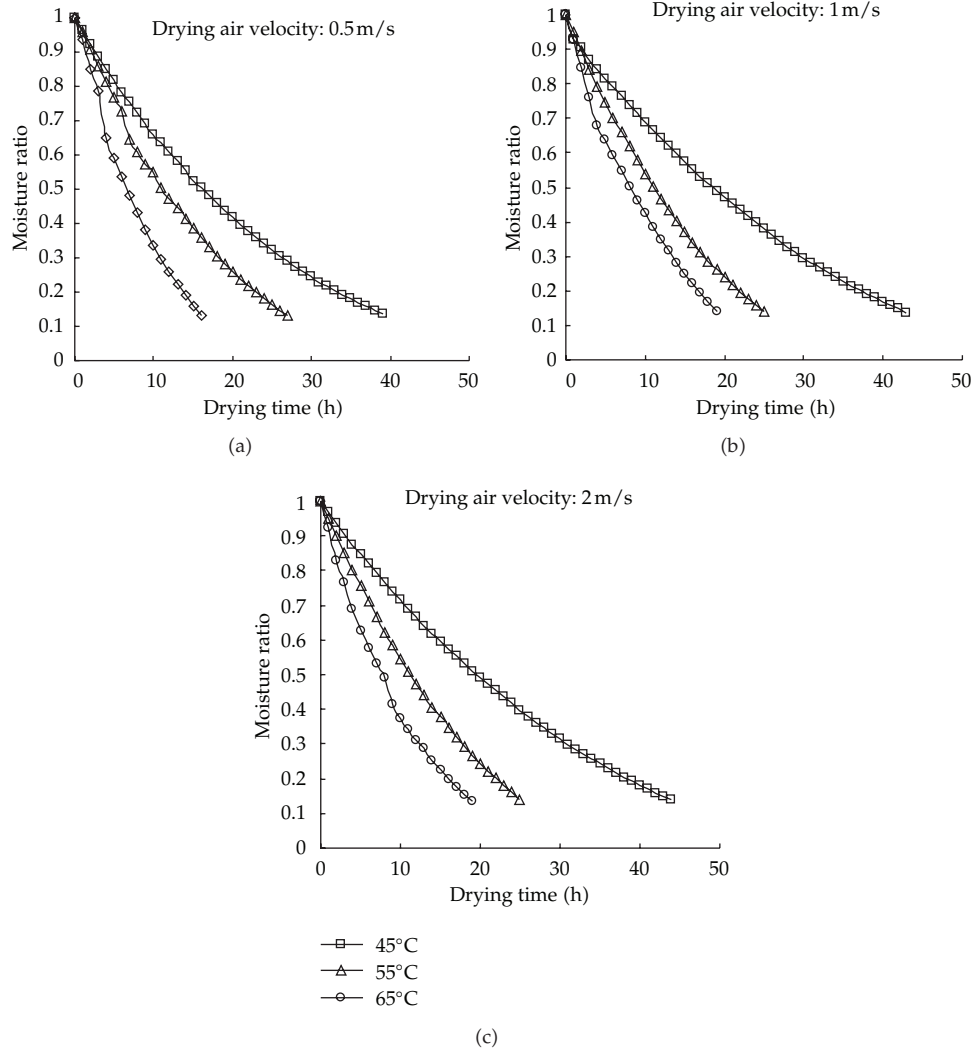


Figure 3: The experimental moisture ratios at different drying temperatures under each air velocity.

MR is the moisture ratio; k is drying rate constant (h^{-1}); t is time (h); a , n and b is experimental constants. R^2 , changed between 0.997498 and 0.999960; χ^2 , 0.000003–0.000144; RMSE, 0.001523–0.010796.

The Weibull distribution model was analyzed according to the different drying air temperatures and velocity conditions. The individual constants were obtained (Table 4). Furthermore, the multiple regression analysis was adopted to determine the relationship between drying air temperature, velocity, and the drying constants a , k , n , b based on the drying experiment data. All possible combinations of different drying variables were tested and included in the regression analysis [45]. The drying constants and coefficients of the model were as follows:

$$a = -0.408876 + 0.004101 \cdot T - 0.021508 \cdot v, \quad (3.2)$$

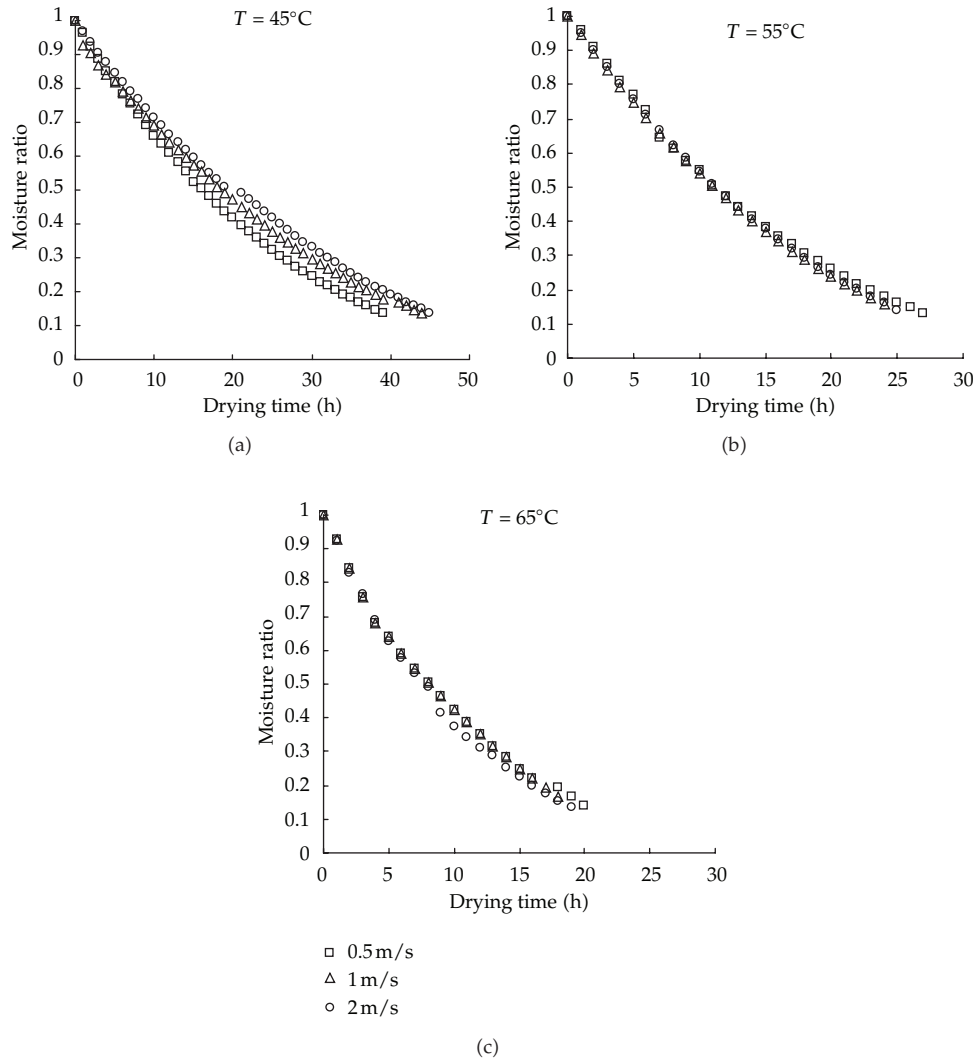


Figure 4: The experimental moisture ratios at different air velocities under each drying temperature.

$$b = -1.371752 + 0.003420 \cdot T - 0.021282 \cdot v, \tag{3.3}$$

$$k = -0.084196 + 0.002463 \cdot T - 0.001119 \cdot v, \tag{3.4}$$

$$n = 1.036553 + 0.000147 \cdot T - 0.008976 \cdot v. \tag{3.5}$$

These expressions could be used to accurately predict the moisture ratio at any time during a drying process. The consistency of the Weibull distribution model and relationships between the coefficients and drying variables were shown in Table 5. As shown, R^2 changed between

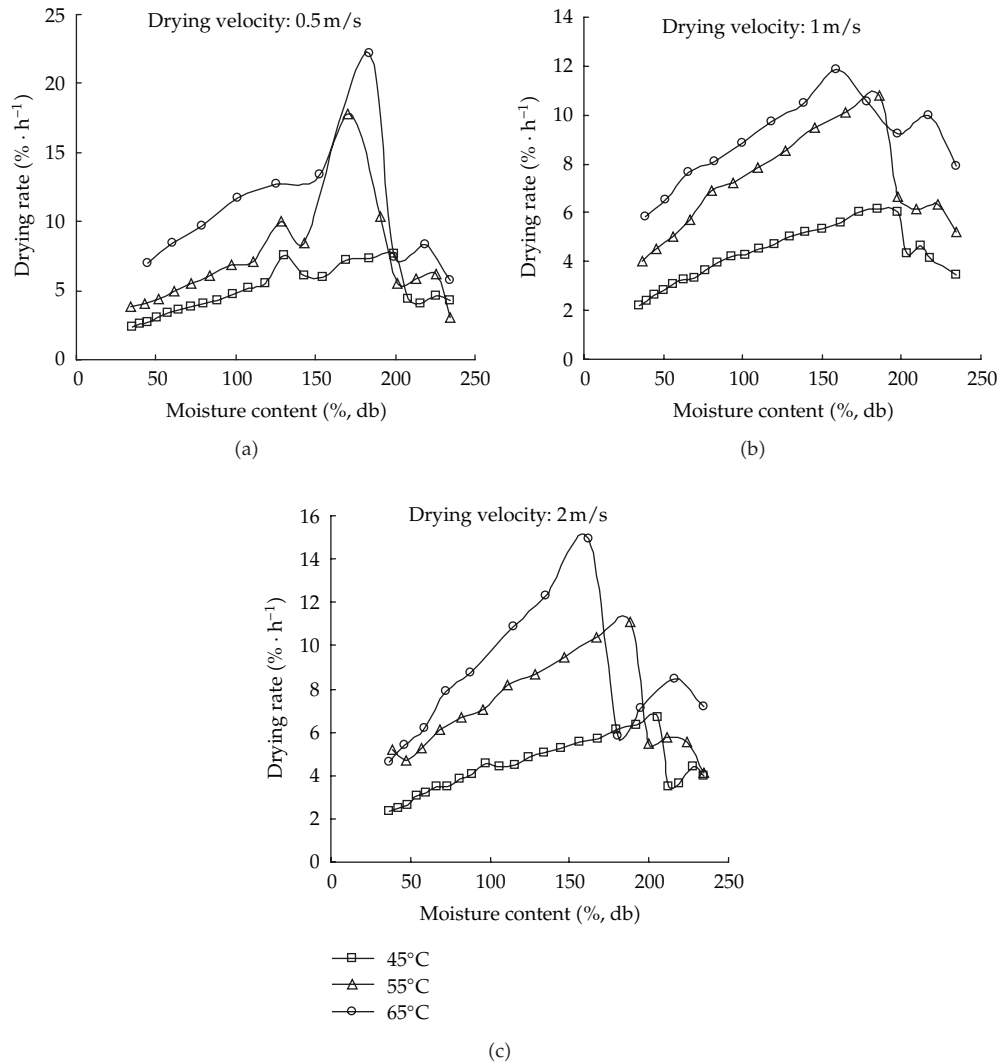


Figure 5: The experimental drying rate at different drying temperatures under each air velocity.

0.993345 and 0.999878, χ^2 was between 0.000008 and 0.000133, and RMSE was between 0.002704 and 0.018925.

In Figure 7, we compared the experimental and predicted moisture ratio at different air temperatures (45, 55 and 65°C) under each velocity (0.5, 1.0 and 2.0 m/s). It could be concluded that the established model was in good agreement with the experimental results at all drying conditions. In this picture figure, a higher drying air temperature produced a higher drying rate and the moisture ratio decreased faster.

To verify the established mathematical drying model, the experimental and predicted values of the moisture ratio at some particular drying conditions were compared. These values were located near a straight line of 45°, as shown in Figure 8, indicating that the drying data were well fitted with the model. Thus, the drying model could be used to well describe the thin-layer drying characteristics of jujubes.

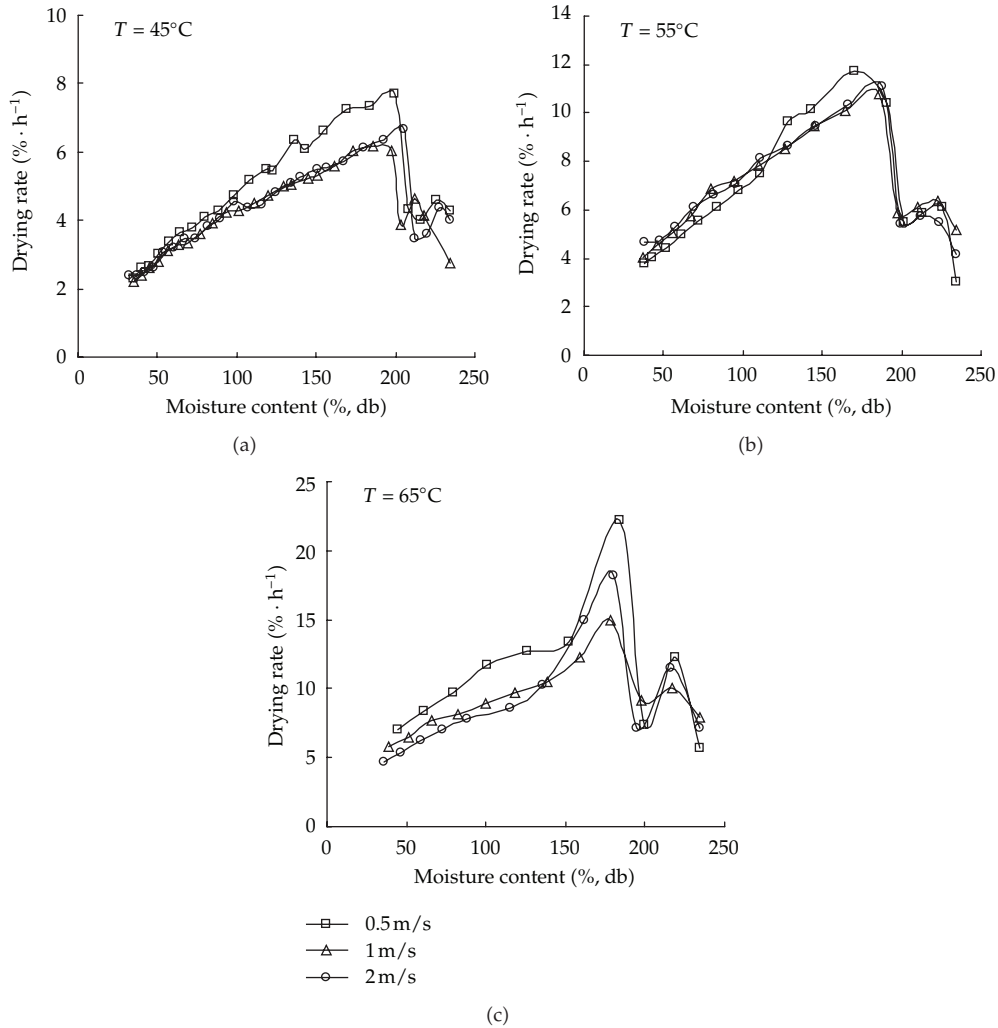


Figure 6: The experimental drying rate at different air velocities under each drying temperature.

3.4. Volume Shrinkage

Jujubes have a porous structure. There are volume shrinkage and deformation during drying process. If ignoring the thermal expansion of materials, the volume shrinkage coefficient equation is expressed as [46]

$$\beta_V = \frac{dV/V}{dM}, \tag{3.6}$$

where V is the volume of jujubes and M is the wet-based average moisture content. Assuming that β_V is constant during the drying process, the above equation can be transformed as follow:

$$V = V_0 e^{-\beta_V(M_0 - M)}. \tag{3.7}$$

Table 4: Statistical results of Weibull distribution model and its constants and coefficients at different drying conditions.

Drying air temperature (°C)	Drying air velocity (m/s)	A	k	n	b	R^2	χ^2	RMSE
$MR = a - b \exp[-(kt^n)]$								
45	0.5	-0.134726	0.032960	1.029610	-1.132454	0.999926	0.000005	0.002076
	1.0	-0.434287	0.027195	0.935657	-1.415498	0.999939	0.000004	0.001916
	2.0	-0.281029	0.024410	1.011860	-1.279307	0.999943	0.000004	0.001911
55	0.5	-0.077911	0.045093	1.087933	-1.083897	0.999454	0.000032	0.005643
	1.0	-0.197083	0.043597	1.047830	-1.195635	0.999960	0.000003	0.001523
	2.0	-0.189766	0.041694	1.063013	-1.190183	0.999935	0.000004	0.001962
65	0.5	-0.051858	0.080259	1.103842	-1.060497	0.998643	0.000098	0.008839
	1.0	-0.451906	0.071394	0.859843	-1.460438	0.997498	0.000144	0.010796
	2.0	-0.078706	0.081792	1.013627	-1.079853	0.999306	0.000044	0.006113

Table 5: Influences of drying air temperatures and velocities on Weibull distribution model coefficients.

Drying air temperature (°C)	Drying air velocity (m/s)	R^2	χ^2	RMSE
$MR = (-0.408876 + 0.004101 \cdot T - 0.021508 \cdot v) - (-1.371752 + 0.003420 \cdot T - 0.021282 \cdot v) \cdot \exp\{-[(-0.084196 + 0.002463 \cdot T - 0.001119 \cdot v) \cdot t^{(1.036553+0.000147 \cdot T-0.008976 \cdot v)}]\}$				
45	0.5	0.998378	0.000098	0.009698
	1.0	0.999878	0.000008	0.002704
	2.0	0.999001	0.000066	0.007970
55	0.5	0.999369	0.000039	0.006064
	1.0	0.999855	0.000009	0.002891
	2.0	0.999737	0.000017	0.003949
65	0.5	0.998525	0.000094	0.009217
	1.0	0.997425	0.000133	0.010952
	2.0	0.993345	0.000389	0.018925

The coefficients of volume shrinkage at different drying air temperatures are shown in Figure 9. We can see from the figure that the coefficients, which rang from 0.011 to 0.020, decline with the increase of air temperature under same air velocity, due to the larger changes of moisture content at higher temperature. The coefficients, measured by least-square method, are shown in Table 6.

Figure 10 shows that the volume changes with time at different drying air temperatures. The figure shows that the changing trend is basically identical with the change of moisture content. It means that with the increase of air temperature, the material shrinkage becomes more and more obvious during the drying process. Thus, when we choose air temperature, not only the drying rate but also the morphology and quality of the products should be taken into consideration.

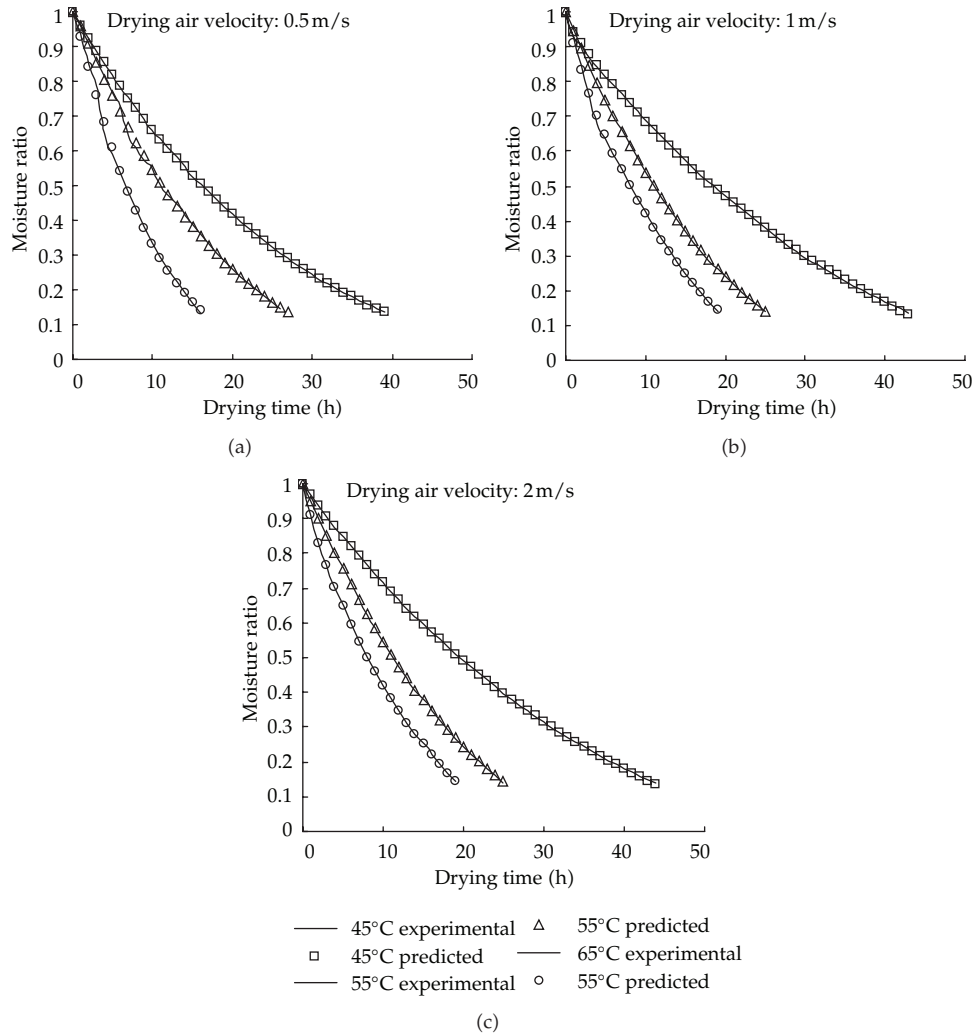


Figure 7: The experimental and predicted moisture ratios at different temperatures under each air velocity.

Table 6: Values of volumetric shrinkable coefficient obtained from different temperatures.

Drying air temperature (°C)	β_v	R^2
45	0.020	0.995
55	0.014	0.992
65	0.011	0.993

4. Conclusions

Thin-layer drying of jujubes were investigated in this study. Ten models selected from the literatures were referred to illustrate the characteristics of the drying process and establish mathematical drying models of jujubes. Drying process for jujubes involved two periods, accelerating rate and falling rate period, no constant-rate period of drying was observed.

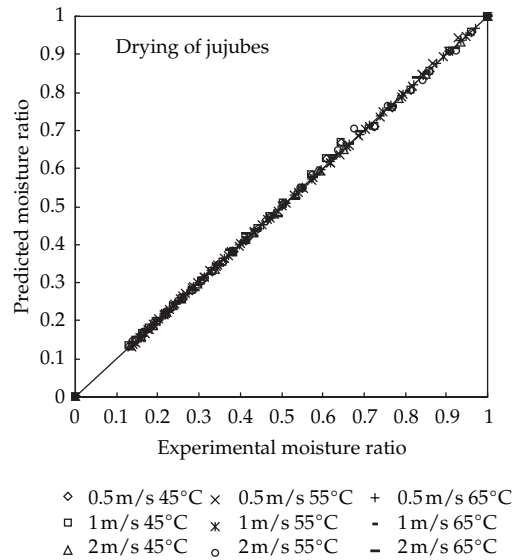


Figure 8: A comparison of experimental and predicted values by the Weibull distribution model at different drying conditions.

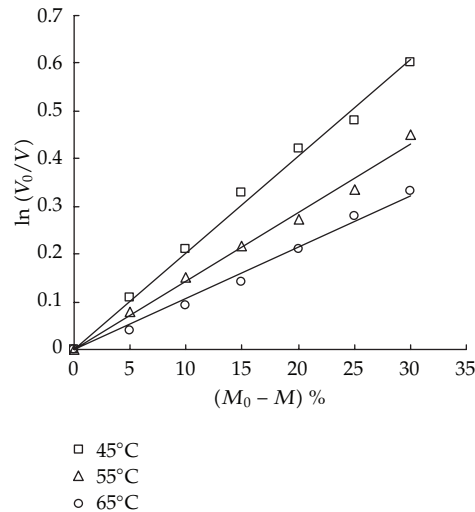


Figure 9: Coefficients of volume shrinkage at different temperature.

After comparing the calculated R^2 , χ^2 , and RMSE in each model, Weibull distribution model showed the best agreement with the experimental data. Furthermore, the effects of the drying air temperatures and velocities on the drying constants and coefficients of the Weibull distribution model were closely examined. We found that this model could be used to predict the moisture ratios of the jujubes during a drying process at any time, particularly at drying temperatures of 45–65°C and velocities of 0.5–2.0 m/s. Moreover, our results showed that the drying air temperature had a bigger effect on drying rate than the velocity. The

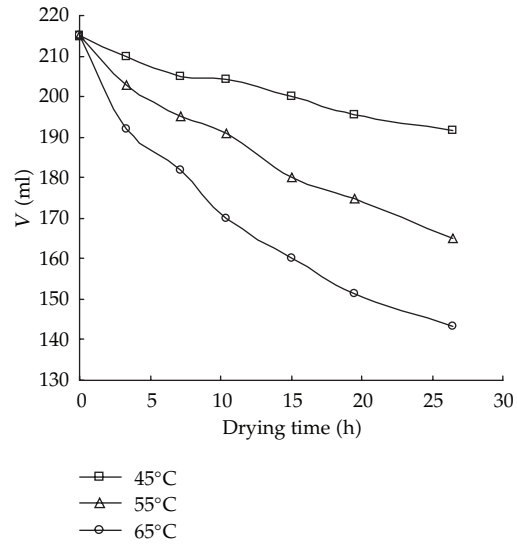


Figure 10: Volume changes with time at different temperatures.

volumetric shrinkable coefficient of jujubes was found to be in the range of 0.011–0.020 at drying temperatures of 45–65°C.

Nomenclature

α, b, c, g, p, n :	Drying coefficients
k, k_1 :	Drying constants
M :	Moisture content at any time, kg water/kg dry matter
M_e :	Equilibrium moisture content, kg water/kg dry matter
M_0 :	Initial moisture content, kg water/kg dry matter
M_t :	Moisture content at t , kg water/kg dry matter
$M_{t+\Delta t}$:	Moisture content at $t + \Delta t$, kg water/kg dry matter
MR:	Dimensionless moisture ratio
MR _{exp} :	Experimental dimensionless moisture ratio
MR _{pre} :	Predicted dimensionless moisture ratio
N :	Number of observations
χ^2 :	Chi-square
R^2 :	Coefficient of determination
RMSE:	Root mean square error
z :	Number of drying constants
t :	Drying time, h
T :	Temperature, °C
v :	Velocity, m/s
V :	Volume, mL
V_0 :	Initial volume, mL
β_v :	Volumetric shrinkable coefficient.

Acknowledgment

This work is supported by National Natural Science Foundation of China (no. 10964009).

References

- [1] Y. F. Cao, S. J. Li, F. M. Zhao, and D. A. Su, "Introduction on the development, problems and solutions in the jujube industry of China," *Packaging and Food Machinery*, vol. 27, no. 4, pp. 46–49, 2009.
- [2] C. G. Lei, J. P. Chen, and D. X. Lu, "The nutritive value and health function of zipiphi jujubes," *Progress in Modern Biomedicine*, vol. 6, no. 3, pp. 56–57, 2006.
- [3] Y. X. Zhang and D. H. Liu, "The processing status and developmental foreground of Chinese date in our country," *Storage & Process*, vol. 5, pp. 15–17, 2008.
- [4] R. K. Goyal, A. R. P. Kingsly, M. R. Manikantan, and S. M. Ilyas, "Mathematical modelling of thin layer drying kinetics of plum in a tunnel dryer," *Journal of Food Engineering*, vol. 79, no. 1, pp. 176–180, 2007.
- [5] A. Maskan, S. Kaya, and M. Maskan, "Hot air and sun drying of grape leather (pestil)," *Journal of Food Engineering*, vol. 54, no. 1, pp. 81–88, 2002.
- [6] I. Doymaz, "Drying kinetics of white mulberry," *Journal of Food Engineering*, vol. 61, no. 3, pp. 341–346, 2004.
- [7] H. O. Menges and C. Ertekin, "Mathematical modeling of thin layer drying of Golden apples," *Journal of Food Engineering*, vol. 77, no. 1, pp. 119–125, 2006.
- [8] V. R. Sagar and P. Suresh Kumar, "Recent advances in drying and dehydration of fruits and vegetables: a review," *Journal of Food Science and Technology*, vol. 47, no. 1, pp. 15–26, 2010.
- [9] M. A. Karim and M. N. A. Hawlader, "Drying characteristics of banana: theoretical modelling and experimental validation," *Journal of Food Engineering*, vol. 70, no. 1, pp. 35–45, 2005.
- [10] V. T. Karathanos and V. G. Belessiotis, "Application of a thin-layer equation to drying data of fresh and semi-dried fruits," *Journal of Agricultural Engineering Research*, vol. 74, no. 4, pp. 355–361, 1999.
- [11] J. A. Hernandez, G. Pavon, and M. A. Garcia, "Analytical solution of mass transfer equation considering shrinkage for modeling food drying kinetics," *Journal of Food Engineering*, vol. 45, pp. 1–10, 2000.
- [12] H. O. Menges and C. Ertekin, "Thin layer drying model for treated and untreated Stanley plums," *Energy Conversion and Management*, vol. 47, no. 15–16, pp. 2337–2348, 2006.
- [13] J. Bon, C. Rosselló, A. Femenia, V. Eim, and S. Simal, "Mathematical modeling of drying kinetics for apricots: influence of the external resistance to mass transfer," *Drying Technology*, vol. 25, no. 11, pp. 1829–1835, 2007.
- [14] R. Dandamrongrak, G. Young, and R. Mason, "Evaluation of various pre-treatments for the dehydration of banana and selection of suitable drying models," *Journal of Food Engineering*, vol. 55, no. 2, pp. 139–146, 2002.
- [15] T. K. Gachovska, A. A. Adedeji, M. Ngadi, and G. V. S. Raghavan, "Drying characteristics of pulsed electric field-treated carrot," *Drying Technology*, vol. 26, no. 10, pp. 1244–1250, 2008.
- [16] S. J. Babalis, E. Papanicolaou, N. Kyriakis, and V. G. Belessiotis, "Evaluation of thin-layer drying models for describing drying kinetics of figs (*Ficus carica*)," *Journal of Food Engineering*, vol. 75, no. 2, pp. 205–214, 2006.
- [17] O. Yaldiz, C. Ertekin, and H. I. Uzun, "Mathematical modeling of thin layer solar drying of sultana grapes," *Energy*, vol. 26, no. 5, pp. 457–465, 2001.
- [18] O. Yaldiz, C. Ertekin, and H. I. Uzun, "Mathematical modeling of thin layer solar drying of sultana grapes," *Energy*, vol. 26, no. 5, pp. 457–465, 2001.
- [19] S. Janjai, M. Precoppe, N. Lamler et al., "Thin-layer drying of litchi (*Litchi chinensis* Sonn.)," *Food and Bioproducts Processing*, 2010.
- [20] A. Midilli, H. Kucuk, and Z. Yapar, "A new model for single-layer drying," *Drying Technology*, vol. 20, no. 7, pp. 1503–1513, 2002.
- [21] R. L. Sawhney, P. N. Sarsavadia, D. R. Pangavhane, and S. P. Singh, "Determination of drying constants and their dependence on drying air parameters for thin layer onion drying," *Drying Technology*, vol. 17, no. 1–2, pp. 299–315, 1999.
- [22] K. Sacilik, "Effect of drying methods on thin-layer drying characteristics of hull-less seed pumpkin (*Cucurbita pepo* L.)," *Journal of Food Engineering*, vol. 79, no. 1, pp. 23–30, 2007.

- [23] O. Corzo, N. Bracho, A. Pereira, and A. Vásquez, "Weibull distribution for modeling air drying of coroba slices," *Food Science and Technology*, vol. 41, no. 10, pp. 2023–2028, 2008.
- [24] E. Uribe, A. Vega-Gálvez, K. Di Scala, R. Oyanadel, J. Saavedra Torrico, and M. Miranda, "Characteristics of convective drying of pepino fruit (*Solanum muricatum* Ait.): application of weibull distribution," *Food and Bioprocess Technology*, pp. 41349–81356, 2009.
- [25] J. P. Chen, Q. Y. Mu, and C. R. Tian, "Study on the effect of the different heating processes on the quality of the Chinese date," *Transactions of the Chinese Society of Agricultural Engineering*, vol. 15, no. 3, pp. 237–240, 1999.
- [26] M. H. Cui, "Solar convective drying properties of candied date," *Journal of Hebei University of Science and Technology*, vol. 20, no. 2, pp. 72–76, 1999.
- [27] M. H. Cui, "Study on the characteristics of candied dates' convective drying mass transfer," *Journal of Hebei Normal University*, vol. 30, no. 4, pp. 450–452, 2006.
- [28] X. Yang, Y. Xie, and G. Jin, "Improved scheme and test comparison of drying jujube date using heat pump," *Transactions of the Chinese Society of Agricultural Engineering*, vol. 25, no. 9, pp. 329–332, 2009.
- [29] Z. Y. Niu, H. Q. Tan, and L. Zong, "Experimental research on the drying characteristics of jujubes," *Food & Machinery*, vol. 5, pp. 18–20, 1998.
- [30] General Administration of Quality Supervision, Inspection and Quarantine, *Dried Chinese Jujubes*, Administration of Quality Supervision, Inspection and Quarantine (AQSIQ), Beijing, China, 2009.
- [31] E. Akpınar, A. Midilli, and Y. Bicer, "Single layer drying behaviour of potato slices in a convective cyclone dryer and mathematical modeling," *Energy Conversion and Management*, vol. 44, no. 10, pp. 1689–1705, 2003.
- [32] A. Midilli, H. Olgun, and T. Ayhan, "Experimental studies on mushroom and pollen drying," *International Journal of Energy Research*, vol. 23, no. 13, pp. 1143–1152, 1999.
- [33] A. Midilli, "Determination of pistachio drying behaviour and conditions in a solar drying system," *International Journal of Energy Research*, vol. 25, no. 8, pp. 715–725, 2001.
- [34] L. M. Diamente and P. A. Munro, "Mathematical modelling of hot air drying of sweet potato slices," *International Journal of Food Science and Technology*, vol. 26, no. 1, pp. 99–109, 1991.
- [35] A. Midilli and H. Kucuk, "Mathematical modeling of thin layer drying of pistachio by using solar energy," *Energy Conversion and Management*, vol. 44, no. 7, pp. 1111–1122, 2003.
- [36] C. Ertekin and O. Yaldiz, "Drying of eggplant and selection of a suitable thin layer drying model," *Journal of Food Engineering*, vol. 63, no. 3, pp. 349–359, 2004.
- [37] P. S. Madamba, R. H. Driscoll, and K. A. Buckle, "The thin-layer drying characteristics of garlic slices," *Journal of Food Engineering*, vol. 29, no. 1, pp. 75–97, 1996.
- [38] M. Ozdemir and Y. Onur Devres, "Thin layer drying characteristics of hazelnuts during roasting," *Journal of Food Engineering*, vol. 42, no. 4, pp. 225–233, 1999.
- [39] I. T. Togrul and D. Pehlivan, "Mathematical modelling of solar drying of apricots in thin layers," *Journal of Food Engineering*, vol. 55, no. 3, pp. 209–216, 2002.
- [40] D. R. Pangavhane, R. L. Sawhney, and P. N. Sarsavadia, "Effect of various dipping pretreatment on drying kinetics of Thompson seedless grapes," *Journal of Food Engineering*, vol. 39, no. 2, pp. 211–216, 1999.
- [41] I. Doymaz, "Effect of dipping treatment on air drying of plums," *Journal of Food Engineering*, vol. 64, no. 4, pp. 465–470, 2004.
- [42] S. Erenturk, M. S. Gulaboglu, and S. Gultekin, "The thin-layer drying characteristics of rosehip," *Bio-systems Engineering*, vol. 89, no. 2, pp. 159–166, 2004.
- [43] S. Kaleemullah and R. Kailappan, "Monolayer moisture, free energy change and fractionation of bound water of red chillies," *Journal of Stored Products Research*, vol. 43, no. 2, pp. 104–110, 2007.
- [44] S. J. Babalis and V. G. Belessiotis, "Influence of the drying conditions on the drying constants and moisture diffusivity during the thin-layer drying of figs," *Food Science and Technology*, vol. 42, pp. 180–186, 2009.
- [45] E. K. Akpınar, "Determination of suitable thin layer drying curve model for some vegetables and fruits," *Journal of Food Engineering*, vol. 73, no. 1, pp. 75–84, 2006.
- [46] S. E. Charm, *The Fundamentals of Food Engineering*, AVI Publishing Company Inc., Westport, Conn, USA, 3rd edition, 1978.
- [47] W. K. Lewis, "The rate of drying of solid materials," *Industrial Engineering Chemistry*, vol. 13, no. 5, pp. 427–432, 1921.
- [48] G. E. Page, *Factors influencing the maximum rates of air drying shelled corn in thin layers*, M.S. thesis, Purdue University, West Lafayette, Ind, U.S., 1949.

- [49] C. Y. Wang and R. P. Singh, "Use of variable equilibrium moisture content in modelling rice drying," ASAE Paper 78-6505, American Society of Agricultural and Biological Engineers, St. Joseph, Mich, USA, 1978.
- [50] D. G. Overhults, G. M. White, H. E. Hamilton, and I. J. Ross, "Drying soybean with heated air," *Transactions of the American Society of Agricultural Engineers*, vol. 16, no. 1, pp. 112–113, 1973.
- [51] S. M. Henderson and S. Pabis, "Grain drying theory. 1. Temperature effect on drying coefficient," *Journal of Agricultural Engineering Research*, vol. 6, pp. 169–174, 1961.
- [52] Y. I. Sharaf-Eldeen, J. L. Blaisdell, and M. Y. Hamdy, "A model for ear corn drying," *Transactions of the American Society of Agricultural Engineers*, vol. 23, no. 5, pp. 1261–1271, 1980.
- [53] T. L. Thompson, R. M. Peart, and G. H. Foster, "Mathematical simulation of corn drying: a new model," *Transactions of the American Society of Agricultural Engineers*, vol. 11, pp. 582–586, 1968.
- [54] W. Weibull, "A statistical distribution of wide applicability," *Journal of Applied Mechanics*, vol. 18, pp. 293–297, 1951.

Research Article

Simulation for Sludge Flocculation I: Brownian Dynamic Simulation for Perikinetic Flocculation of Charged Particle

Linshuang Liu,^{1,2} Guolu Yang,^{1,2} and Minghui Yu²

¹ Sewage Sludge & Silt Research Center, Wuhan University, Wuhan 430072, China

² State Key Laboratory of Water Resource and Hydropower Engineering Sciences, Wuhan University, Wuhan 430072, China

Correspondence should be addressed to Linshuang Liu, liu1965888@163.com

Received 27 October 2011; Revised 21 December 2011; Accepted 21 December 2011

Academic Editor: Zhijun Zhang

Copyright © 2012 Linshuang Liu et al. This is an open access article distributed under the Creative Commons Attribution License, which permits unrestricted use, distribution, and reproduction in any medium, provided the original work is properly cited.

To investigate sludge drying process, a numerical simulation based on Brownian dynamic for the floc with uncharged and charged particles was conducted. The Langevin equation is used as dynamical equation for tracking each particle in a floc. An initial condition and periodic boundary condition which well conformed to reality is used for calculating the floc growth process. Each cell consists of 1000 primary particles with diameter $0.1 \sim 4 \mu\text{m}$. Floc growth is related to the thermal force and the electrostatic force. The electrostatic force on a particle in the simulation cell is considered as the sum of electrostatic forces from other particles in the original cell and its replicate cells. It is assumed that flocs are charged with precharged primary particles in dispersion system by ionization. By the analysis of the simulation figures, on one hand, the effects of initial particle size and sludge density on floc smashing time, floc radius of gyration, and fractal dimension were discussed. On the other hand, the effects of ionization on floc smashing time and floc structure were presented. This study has important practical value in the high-turbidity water treatment, especially for sludge drying.

1. Introduction

There are numerous sediment-laden rivers in china. There are 42 rivers whose average annual sediment discharge is larger than 10 million. The sediment discharge of the Yellow River and the Yangtze River is 29.3% of the total top thirteen great rivers in the world. There are also many seasonal high-turbidity rivers on other regions of china. Therefore, the research of the high-turbidity water treatment has become a important research topic in china [1, 2].

The effect of moisture content on the sludge volume is enormous. Moisture of sludge which taken out from the lakes and rivers was very high. This led a lot of work needed to be

done before sludge can be used as resources. The moisture associated with flocs of sludge is: 70–75% free water, 20–25% floc water, and 1% each capillary and bound water. The free water can be removed by thickening. The floc water is trapped in the interstices of floc particles and is separable only by mechanical drying [3]. However, as the sludge flocculation mechanism is complex, it is still difficult to dry vast amount of sludge rapidly. As a method of dehydration, flocculation has been often used in drying engineering. Therefore, flocculation mechanism and its dynamcis simulation are very important to improve the sludge drying speed in the future studies [4].

Sludge has many properties those differ from the coarse sediment and solution molecular. The floc of fine sediment particles occurs mostly in the flocculation process. In the sludge drying process, the particles grow to floc with electrochemical force [5] and adsorption [6]. These processes are very common in many hydrosol processes, especially for fine sediment flocculation. In the case of thermally stable particles, the Brownian motion should be considered as the dominant action. The aggregation characteristics are mainly affected by the morphology of aggregates [7]. As a fractal dimension can quantify the morphology of flocculation, it becomes a key variable for analyzing the flocculation dynamics. Ermak [8] simulated the flocculation process of charged particles in solution using Brownian dynamics. With more new applications for solid particles in solution recently, it is important to control the flocs size and its morphology in flocculation process. Xiong et al. [9] simulated the growth of game colloidal particle in the sectional colloid model. However, their results were obtained using the assumption of spherical particles. More work is necessary to better explain the realistic case. In this paper, we tried to simulate the motion of particles and analyse the effect of electrostatic force on the morphology in the sludge drying process. Therefore, we introduced a model that could describe the electrostatic force among charged sludge particles. This electrostatic simulation model was coupled with the Brownian dynamic simulation to deal with the flocculation of charged sludge particles. A comparison of floc growth process with different sludge density and particle diameters of charged and uncharged particles is present.

2. Theory

2.1. Langevin Equation

Brownian dynamics describe the dynamic behavior of a sediment particle whose mass and size are larger than those of the water molecules they are immersed in. These particles are subject to stochastic collisions with the water molecules, which leads to the random motion of the particles. It is assumed that a particle is in thermal equilibrium and surrounded by water molecules at a specific temperature T . The particles in this system are subject to an external force R_n . In this case, the translational motion is described by the Langevin equation. The strict Langevin equation for the motion of a particle on the x, y, z coordinates is given by (2.1) together with several supplementary conditions [10, 11]:

$$\frac{d(mu_n)}{dt} = F_n - m\beta u_n + X_n \quad (n = x, y, z), \quad (2.1)$$

$$\langle X_n \rangle = 0, \quad \langle X_n^2 \rangle = 2\beta mk_b T, \quad \langle u_n(t) \cdot u_n(0) \rangle = 0 \quad (n = x, y, z). \quad (2.2)$$

In (2.1), the left term of equation represents the Brownian particle's momentum, and the R_n is systematic external force acting on the particle. In perikinetic flocculation, this term

includes van der Waals force, electrostatic force, magnetic force, image force, and so forth. The other forces except for the electrostatic force can be negligible in the flocculation of charged sediment particles because the other forces are much smaller than the electrostatic force [5]. The specific calculation of the electrostatic force will be executed in Section 3. The second right term of equation is the frictional resistance of the fluid around the particle. β is the friction constant, and it's the inverse of particle relaxation time. The last term X_n is an external force caused by the random collisions between the particle and the surrounding water molecule. The random force X_n is represented by the Gaussian random-distribution function. The mean and square mean of it are represented as (2.2).

2.2. Solution of the Langevin Equation

Several methods have been used to integrate the Langevin equation [12]. In this study, we use the Monte Carlo method. Integration of (2.1) (2.2) from t to t' yields the equation:

$$\begin{aligned} u_n - u_{0n}e^{-\beta t} - \frac{F_{n0}}{m\beta} \cdot (t - e^{-\beta t}) &= \frac{1}{m} \int_0^t e^{-\beta(t-t')} X_n(t_0 + t') dt' \quad (n = x, y, z), \\ r_n - r_{n0} \frac{u_{n0}}{\beta} \cdot (1 - e^{-\beta t}) - \frac{F_{n0}}{m\beta} \left[t - \frac{1}{\beta} (1 - e^{-\beta t}) \right] &= \frac{1}{m\beta} \int_0^t [1 - e^{-\beta(t-t')}] X_n(t_0 + t') dt'. \end{aligned} \quad (2.3)$$

Equation (2.3) cannot be used directly to calculate the velocity and position changes due to the random nature of $X(t)$. We calculate the statistical properties of the two integrals involving $X(t)$ with one method derived by Luo et al. [11]

$$\begin{aligned} u_n &= u_{0n}e^{-\beta t} + \frac{F_{0n}}{m\beta} \cdot (t - e^{-\beta t}) + B_{1n}, \\ r_n &= r_{n0} + \frac{u_{n0}}{\beta} \cdot (1 - e^{-\beta t}) + \frac{F_{n0}}{m\beta} \left[t - \frac{1}{\beta} (1 - e^{-\beta t}) \right] + B_{2n} \quad (n = x, y, z), \end{aligned} \quad (2.4)$$

where B_{1n}, B_{2n} are random function of time chosen from the bivariate Gaussian distribution with properties

$$\begin{aligned} \langle B_{1n} \rangle &= \langle B_{2n} \rangle = 0, \\ \langle B_{1n}^2 \rangle &= \frac{3kT}{m} (1 - e^{-2\beta t}), \\ \langle B_{2n}^2 \rangle &= \frac{kT}{m\beta^2} (2\beta t - 3 + 4e^{-\beta t} - e^{-2\beta t}), \\ \langle B_{1n} \cdot B_{2n} \rangle &= 0 \quad (i = 1, 2, \quad n = x, y, z). \end{aligned} \quad (2.5)$$

2.2.1. Floc Structure

The morphological state of the flocs is defined as the fractal number by Forrest and Witten [13]. They confirmed that there was a power law relation between the characteristic length

and the number of primary particles in each floc. Fractal structure of floc has been researched by many researches [14, 15]. Generally, the radius of gyration of the flocculation is used as the characteristic length for the floc. The power law relation is expressed as

$$R_f = \sqrt{\frac{1}{n} \sum_1^n \left(r_j - \frac{1}{n} \sum_1^n r_j \right)^2}, \quad (2.6)$$

where n is the number of primary particles in an floc, R_f is the radius of gyration.

3. Numerical Simulation

3.1. Particle Charging

When fine sediment dispersed in water, they were charged due to ionization and sorption [16, 17]. In this simulation, we assumed that primary particles were charged with some additive ions to simulate the flocculation with different potential flocculent. The equilibrium and diffusive properties of charged spherical particles in solution have been studied by Xiangyan et al. [8], who simulated the motion of particles in solution obeying classical statistical mechanics. In this case, the charge quantity of a floc is the sum of elementary charges on the primary particles. The quantity of electricity on each particle is calculated by ionization intensity formula. In (3.1), C_i is particle molarity, I is ionization intensity, and Z_i is quantivalence of particle. In our research, C_i was relate to sludge density and the span of I was 0.001 ~ 0.1.

$$I = \frac{1}{2} \cdot \sum_1^n C_i \cdot Z_i^2. \quad (3.1)$$

3.2. Initial Condition

To simulate the flocculation process, initial conditions for the position and the velocity of the primary particles have to be given in Figure 1 and Figure 2, respectively. The positions of these particles are obtained with a homogeneous distribution in 3 dimensions. It can be assumed that the primary particles experience only thermal force in the initial state. Therefore, we set the initial velocities with a normal random number generator that is characterized by the Gaussian distribution of zero mean and $k_b T / m_0$ variance.

The primary particles diameters were chosen from 0.1 ~ 4 μm [18, 19], and space between two particles L_0 were calculated with sludge density to coincided to real liquid dispersion. The space is decreased with the increase of sludge density ρ_s as well as particle diameters ρ_p as shown in Figure 3.

We calculated the trajectories of 1000 primary particles in a simulation cell. The cell size was determined by the sludge density ρ_s . Ten simulations for each initial condition were performed to obtain statistically meaningful average values. The particle diameter d_p was value to 0.1, 0.5, 1.0, 2.0, and 4.0 μm separately and ρ_s was value to 1100, 1075, 1050, 1025, and 1010 kg m^{-3} . In this work, we have fixed the values of T , particles density (ρ_p) and Δt to be 293 K, 2650 kg m^{-3} , and 1/50 s, respectively. These conditions were obtained from the experimental conditions in a flocculation process.

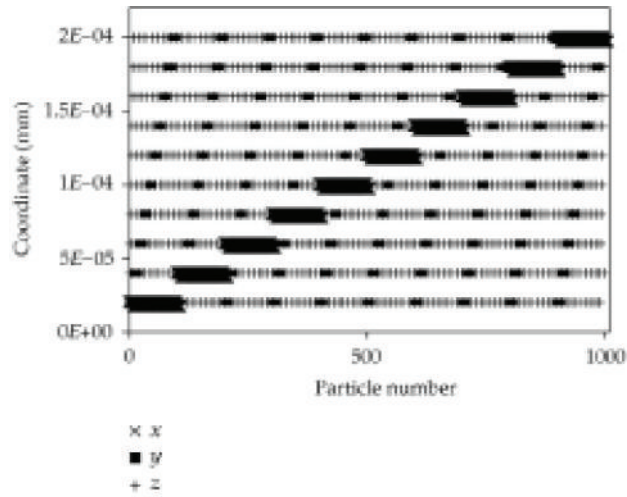


Figure 1: Particle initial position along x, y, z axis.

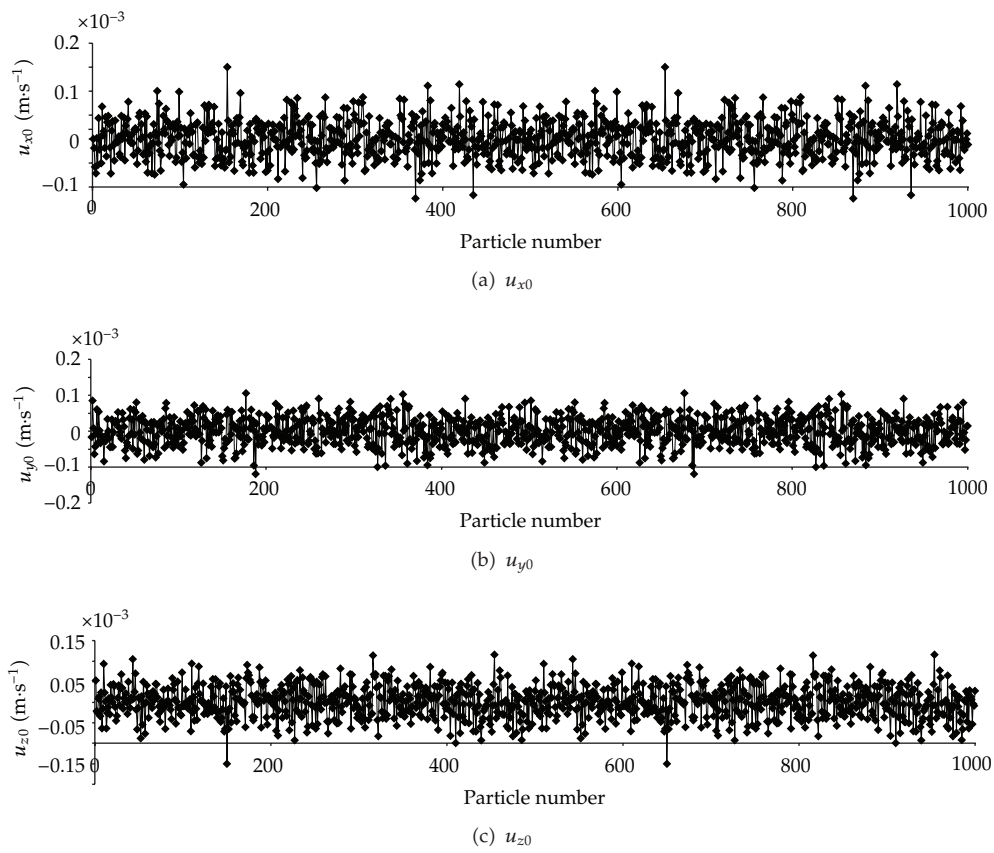


Figure 2: Particle initial velocity along x, y, z axis.

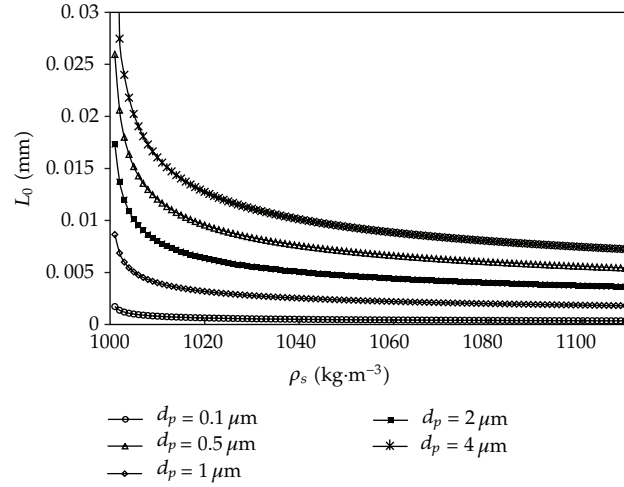


Figure 3: Space between Space between particles with different sludge density.

3.2.1. Boundary Condition

In this simulation, 300 particles were taken as boundary smash condition to signify the termination of floc growing. The periodic boundary condition was used not only for maintaining the internal bond strength but also for calculating the electrostatic force. The electrostatic force of the i th particle is an infinite summation of each force from the other charged particles in the cell. Therefore, this force includes the electrostatic dispersion effect mentioned in the paper of Ermak [8]. The total electrostatic force on particle i is given by

$$F_{0i} = \sum_{j=1, j \neq i}^{\infty} K_e \frac{q_i q_j}{r_{ij}^2} \vec{r}_{ij}. \quad (3.2)$$

In this paper, the electrostatic force can be calculated directly from the gradient of the pair potential. Ermak [8] introduced a new technique for treating an infinite number of pair potential. This potential includes the interaction with the images of the original cell in the replicated cells.

Though an infinite number of particles affect the electrostatic force of a given particle, the force has a finite value because it is symmetrical in a macroscopic sense. In our simulation, electric charges locate in the center of mass of the floc and the dielectric constant of the water is uniform. By applying this method to the present system, the modified electrostatic force by the infinite number of particles can be represented as:

$$F_{0i} = - \sum_{j=1, j \neq i}^N K_e q^2 \left[\nabla \psi_1(r_{ij}) + \nabla \psi_2(\vec{r}_{ij}) \right], \quad (3.3)$$

where N is the total number of flocs in the original, cell; q is quantity of charges on the particles. ψ_1 and ψ_2 are expressed as

$$\psi_1(r) = \operatorname{erfc} \left(\frac{\sqrt{\pi} r / L}{r} \right) - \frac{1}{L} - \frac{\operatorname{Em}}{L}, \quad (3.4)$$

where m_1, m_2, m_3, m_4 are described as

$$\begin{aligned}
m_1 &= -\frac{2k_3k_{11}k_4}{k_5^2}, \\
m_2 &= 2\pi k_3k_9 - k_3k_6 + \frac{2\pi k_3k_8k_1 - k_3k_7k_1}{k_5^2} + \frac{4\pi k_3k_8k_1 + 2\pi k_3k_{11}k_4 - k_3k_{10}k_4}{k_5^3} \\
&\quad + \frac{6k_3k_{11}k_4 + 2\pi k_3k_{13}k_2 - k_3k_2k_{12}}{k_5^4} \\
&\quad + \frac{k_2k_3k_{13}k_2}{k_5^5}, \\
m_3 &= -\frac{4k_3k_8}{k_5^2}, \\
m_4 &= -\frac{8k_3k_{13}}{k_5^4}.
\end{aligned} \tag{3.10}$$

3.3. Calculation Procedure

We define that a particle collides with the floc if the distance between two is located within the radius of gyration of floc. The momentum and the charge quantity are conserved before and after the collision, and immediately the new-formed floc is in thermal equilibrium state. We assumed that the sticking probability was 1 after each collision. The flocs grow with the repetition of the above sequence. The program was written with Fortran 95 and the procedure is shown in Figure 4.

4. Results

4.1. Floc Growth Process

4.1.1. Number of Particles in Floc

A series of comparison of d_p from 0.1 to 4.0 μm were performed to interpret floc growth process. We chose $\rho_s = 1010, 1025, 1050, 1075, \text{ and } 1100 \text{ kg m}^{-3}$ for simulation in order to intergrate with practice. As shown in Figure 5, in the early stage of flocculation the primary particle was sustaining to the a initial flocculent time. The particle number begun to increase after the first stage till reaching the smashing condition. In the final stage of flocculation, the sequence of smashing time with different sludge density is similar to that of initial flocculent time. The initial flocculent time and smashing time are both increased as the floc diameter increased.

4.1.2. The Smashing Time

The floc size can not grow up unlimited in the practice. It could be affect by particle diameter and particle-bonding mode. In this paper, the time that 300 particles conglutinated in one floc

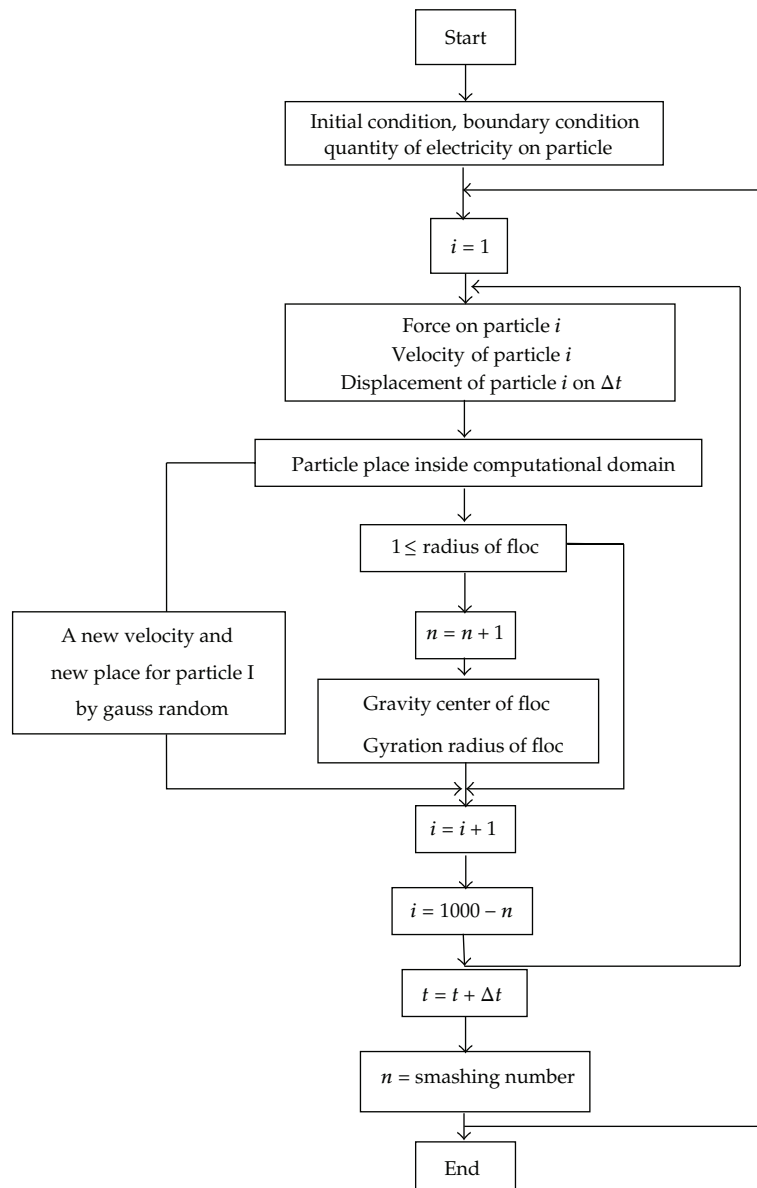
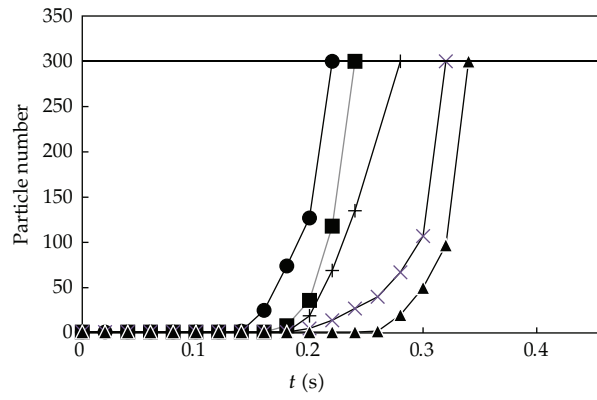
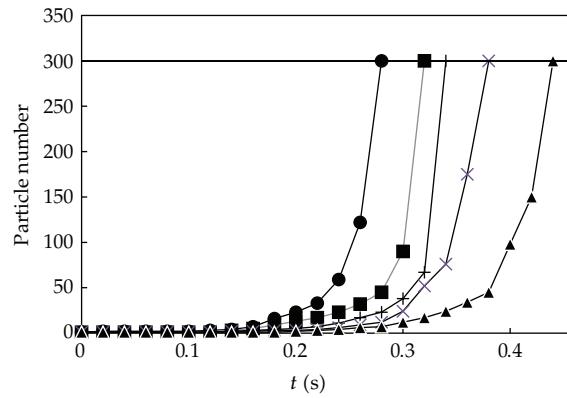


Figure 4: Flow chart for Brownian dynamic simulation.

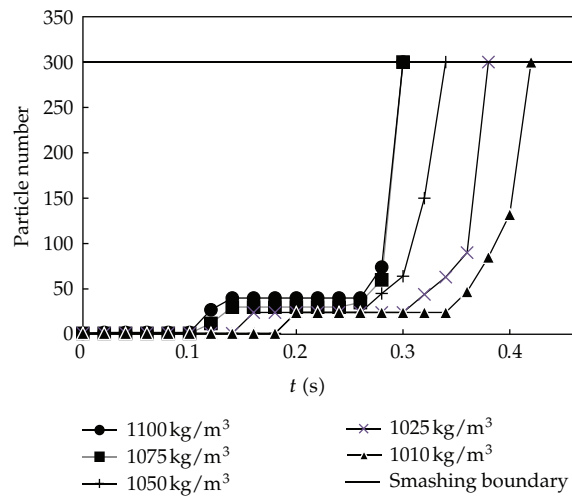
is smashing time. Though smashing time was related to random velocity and displacement, it increased with the decrease of sludge density. Whereas it increased with the increase of particle diameter as shown in Figures 6 and 7. This tendency may be understood, on one hand as particle diameter presents a linear increase, the particle number decreased in a cube way, which leads particle impact probability to decrease. On the other hand, the decrease of sludge density causes particle impact probability to decrease likewise.



(a) $dp = 0.1$



(b) $dp = 1 \text{ um}$



(c) $dp = 4 \text{ um}$

Figure 5: Variety of particle number as floc growing.

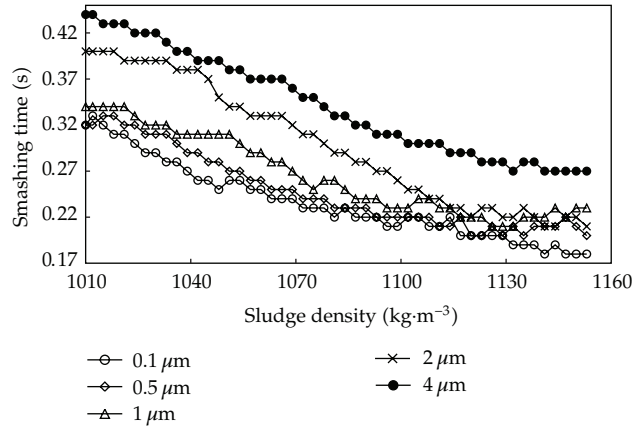


Figure 6: Effects of sludge density on smashing time.

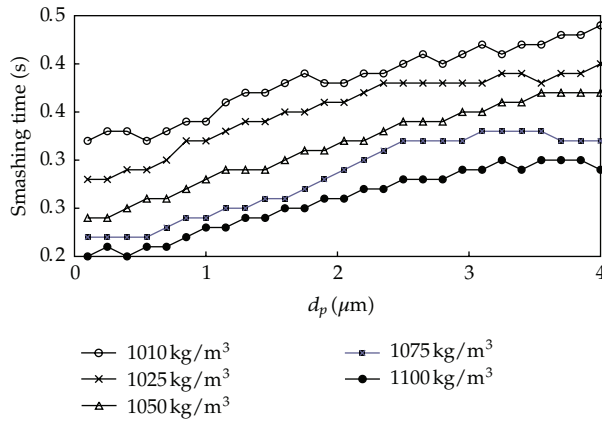


Figure 7: Effects of particle diameter on smashing time.

4.1.3. Radius of Gyration

The relation between the radius of gyration and particle number was not linear positive correlation. The main factors influencing it were particle number and fractal dimension. In this simulation, the radius of gyration is calculated by four variables, they were particle number and x -, y -, z -axis coordinate values. The radius of gyration values in Figure 8 was calculated by three duplicate computations with the initial particle size being equal to 2 μm . It was shown in the Figure 8 that the gyration radius decreased with the increase of sludge density. The relation formulas of sludge density to gyration radius is $R_f = -1441(\rho_s)^3 + 4616(\rho_s)^2 - 4927(\rho_s) + 1752$, and correlation coefficient is 0.992.

4.1.4. Fractal Dimension

The fractal dimension was calculated with gyration radius method. the mean values of fractal dimension of the three series were shown in Figure 9. The relation formulas of sludge density to gyration radius is $D_f = 1.3338 \pm 0.0451 + (0.6049 \pm 0.1424) \times (\rho_s - 1000)^{0.4107 \pm 0.4181}$, and

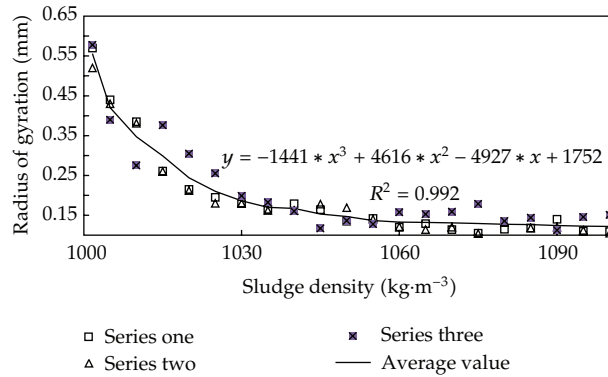


Figure 8: Effects of sludge density on floc diameter.

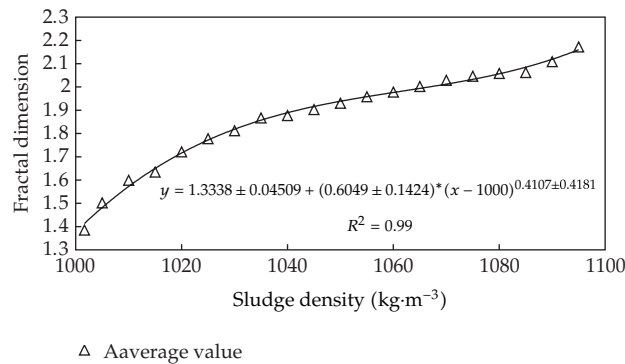


Figure 9: Effects of sludge density on fractal dimension.

correlation coefficient is 0.991. The gyration radius is increased with the increase of sludge density. The reason is that with the increase of sediment density, the collision probability of sediment particles and floc increased, while the opportunities for floc to accept new particles increased, which finally made the floc more compact. Several authors [21, 22] have researched the effects of sludge density on floc fractal dimension with numerical simulation method. The results show that relation formula of sludge density to gyration radius with Diffusion Limited Cluster Aggregation model is $D_f = D_{f0} + a\Phi^c$, which is similar to our conclusion. Xiangyan et al. [15] has studied the effect of sludge density on gyration radius in two-dimensional space and the results presented in their paper are also similar to our conclusion.

4.2. Morphology of Floc

The morphology of the floc is a very important factor to determine the dynamic behavior of flocs. The morphology of a floc is visualized for the case of uncharged particles in Figure 10(a). This floc, consisting of 300 primary particles, is obtained from a simulation based on 1000 primary particles with edge length decided by sludge density. Its structure is quite open to the outer space and it is very similar to the structures of aggregates observed by other researchers [21–23].

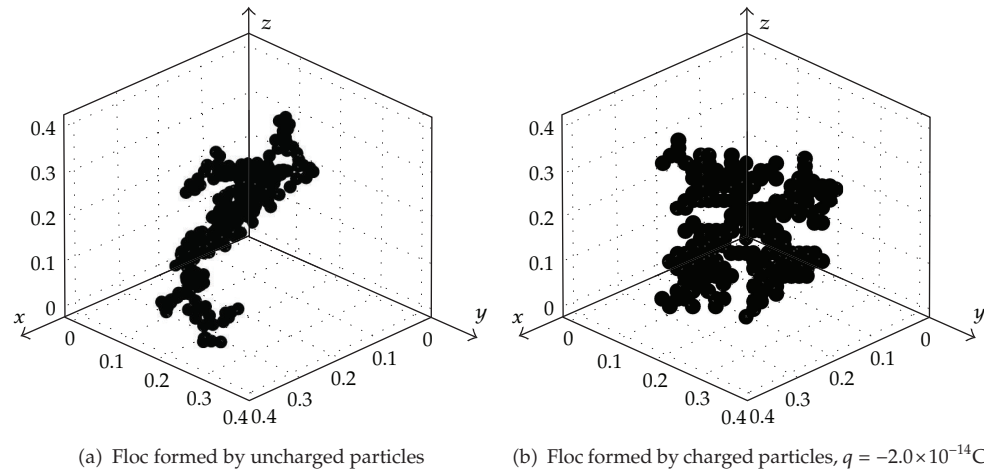


Figure 10: Morphology of floc.

4.3. Effects of Electrostatic Force on Flocs

Figure 11 shows a comparison of the simple Coulomb force and the modified electrostatic force. The Coulomb force was calculated just within only one cell. There is no difference if two particles are close together, there is a relatively large difference as the distance becomes larger. Because of the periodic boundary condition, the electrostatic force must be zero if two particles are located at center and the edge of the simulation cell. The modified electrostatic force satisfies this condition well. Therefore, our model for the electrostatic force can be regarded as a good model coinciding with the real system. The morphology is quantified with a fractal dimension. It is affected by the number of primary particles and the radius of gyration, as shown in Figure 10(b). In this condition, the primary particles have $-2.0 \times 10^{-14} \text{C}$ quantity of electricity according to (3.1).

Four series of growth process are simulated to present the effects of charges on smashing time. As shown in Figure 12, the effect of electric quantity on floc is obvious. However, the effects of unipolar and polar electrical charges on floc are still needed to be researched in the further work. Figures 13(a)–13(c) showed the effect of charges on smashing time. The smashing time is increased with sludge density as well as electrical charges.

5. Conclusions

To investigate sludge drying process, a numerical simulation for the floc of uncharged and charged particles was presented with a Brownian dynamic. The initial conditions for the particle position were contained by sludge density and velocity was given with Gaussian distribution. To treat the electrostatic force, a modified electrostatic force has been introduced.

In a fixed volume of water, the particle number increases gradually as the time and sludge density increase. In the meantime its increasing rate increases with time. However, it decreases as the increase of particle diameter. Though the smashing time was related to random velocity and displacement, it increased as the decrease of sludge density, yet it increased as the increase of initial particle diameter.

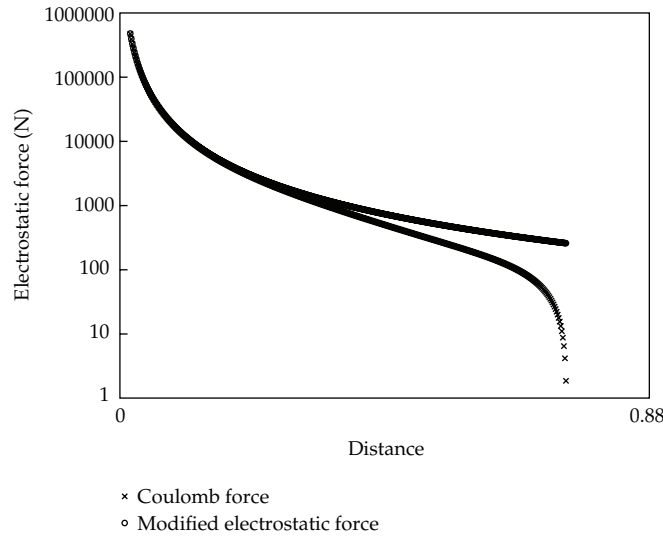


Figure 11: Comparison between modified electrostatic force versus simple Coulomb force.

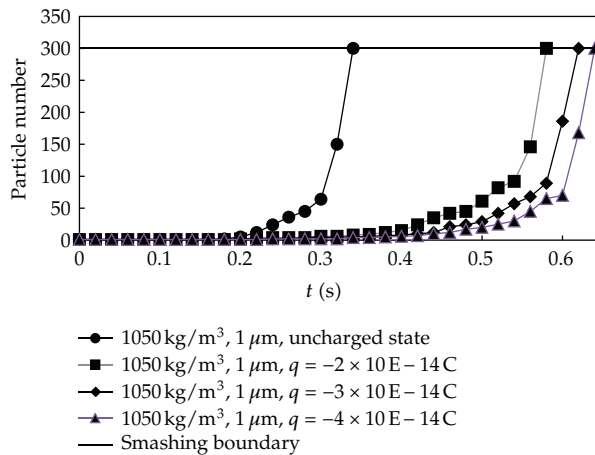
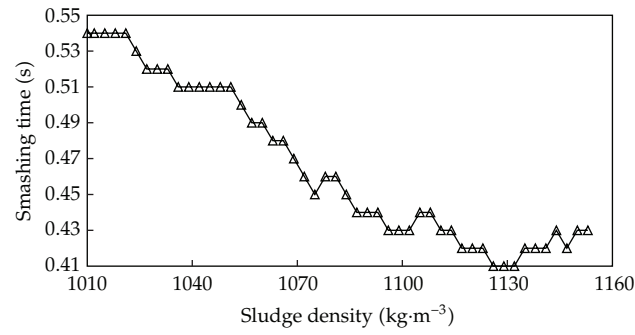


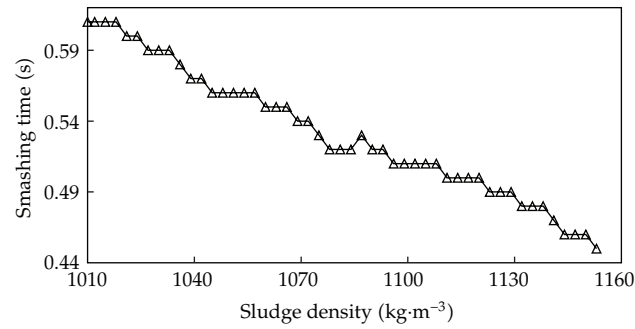
Figure 12: Variety of particle number as floc growing.

The gyration radius is increased with the increase of sludge density. The relation formula of sludge density to fractal dimension is $R_f = -1441(\rho_s)^3 + 4616(\rho_s)^2 - 4927(\rho_s) + 1752$, and correlation coefficient (R_2) is 0.991. The fractal dimension was calculated with gyration radius method. The relation formulas of sludge density to gyration radius is $D_f = 1.3338 \pm 0.0451 + (0.6049 \pm 0.1424) \times (\rho_s - 1000)^{0.4107 \pm 0.4181}$, and correlation coefficient is 0.990. The conclusion is similar to the results of previous studies.

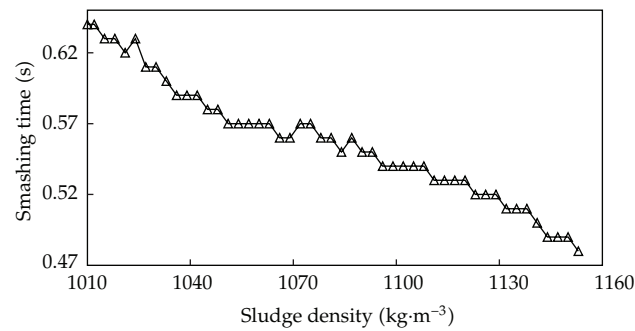
Effects of electric quantity on floc were obvious. The smashing time was increased with the increase of electric quantity. Besides, the polar electrical charges on primal particles make the morphology of floc more open. However, this simulation was carried out under the assumption of the high-moisture content. Therefore, our conclusions cannot be applied directly to other cases, where the moisture content is extremely low. To find out the particles motion



(a) $q = -2 \times 10^{-14}C$



(b) $q = -3 \times 10^{-14}C$



(c) $q = -4 \times 10^{-14}C$

Figure 13: Effects of sludge density on smashing time.

law in the low moisture content, it needs some additional models, and we will perform additional simulations and experiments to confirm it as future works.

Notation

- T : Disperse system temperature, k
- t, t' : Time, s
- Δt : Time step, s
- m : Mass of aggregate, kg

- R_n : External force, N
 u_n : Particle velocity, m/s
 X_n : External force caused by the random collisions, N
 F : Electrostatic force, N
 q : Charge quantities on particle, C
 r : Displacement of aggregate, m
 L : Length of side of simulation cell, m
 L_0 : Initial space between particles, m
 d_p : Particle diameter, m
 R_f : Radius of gyration for aggregate, m
 D_f : Fractal dimension
 n : Total number of particle in one floc, dimensionless
 β : Friction constant, dimensionless. S^{-1}
 Φ : Electrostatic potential energy, $kg \cdot m^2$
 ρ_s : Sludge density, $kg \cdot m^{-3}$
 ρ_p : Particle density, $kg \cdot m^{-3}$
 I : Charge density, dimensionless
 C_i : Particle molar density, $mol \cdot m^{-3}$
 Z_i : The total valence of particle surface, dimensionless
 E_p : Madelung constant, dimensionless
 k_b : Boltzmann constant, dimensionless
 k_e : Coulomb constant, dimensionless.

Acknowledgments

The authors would like to thank Associate Professor Wu Weimin and Associate Professor Yu Liangying for helpful discussions. This study was supported by the National Key Basic Research Development (973) program of China (Grant no. 2011CB403300).

References

- [1] J. Yajun, *A Study on Characteristic and Mechanism of Spontaneous Sedimentation of Yellow River's Loess Particles*, Xi'an University of Architecture and Technology, 2004.
- [2] L. Ligang, *The Study of the Rule of Sediment Movement and Deposit and Operation of Reducing Sediment for Xiaolangdi Reservoir of Yellow River*, Hohai University, 2005.
- [3] T. J. McGhee, *Water Supply and Sewerage*, New York, NY, USA, 1991.
- [4] J. Werther and T. Ogada, "Sewage sludge combustion," *Progress in Energy and Combustion Science*, vol. 25, no. 1, pp. 55–116, 1999.
- [5] H. Helmholtz, "Ueber galvanische Ströme, verursacht durch Concentration sunters chiede, Folgerungen aus der mechanischen Wärmetheorie," *Viedemann' Annalen*, no. 7, p. 337, 1879.
- [6] S. Mishra, A. Mukul, G. Sen, and U. Jha, "Microwave assisted synthesis of polyacrylamide grafted starch (St-g-PAM) and its applicability as flocculant for water treatment," *International Journal of Biological Macromolecules*, vol. 48, no. 1, pp. 106–111, 2011.
- [7] T. Matsoukas and S. K. Friedlander, "Dynamics of aerosol agglomerate formation," *Journal of Colloid And Interface Science*, vol. 146, no. 2, pp. 495–506, 1991.

- [8] D. L. Ermak, "A computer simulation of charged particles in solution. I. Technique and equilibrium properties," *The Journal of Chemical Physics*, vol. 62, no. 10, pp. 4189–4196, 1975.
- [9] Y. Xiong, S. E. Pratsinis, and S. V. R. Mastrangelo, "The effect of ionic additives on aerosol coagulation," *Journal of Colloid And Interface Science*, vol. 153, no. 1, pp. 106–117, 1992.
- [10] B. H. McNaughton, P. Kinnunen, M. Shlomi et al., "Experimental system for one-dimensional rotational Brownian motion," *Journal of Physical Chemistry B*, vol. 115, no. 18, pp. 5212–5218, 2011.
- [11] J. P. Luo, Z. M. Lu, and Y. L. Liu, "Simulation of Lagrangian dispersion using a Lagrangian stochastic model and DNS in a turbulent channel flow," *Journal of Hydrodynamics*, vol. 21, no. 6, pp. 767–773, 2009.
- [12] P. Turq, F. Lantelme, and H. L. Friedman, "Brownian dynamics: its application to ionic solutions," *The Journal of Chemical Physics*, vol. 66, no. 7, pp. 3039–3044, 1976.
- [13] S. R. Forrest and T. A. Witten, "Long-range correlations in smoke-particle aggregates," *Journal of Physics A*, vol. 12, no. 5, pp. L109–L117, 1979.
- [14] J. H. Jeon and R. Metzler, "Fractional Brownian motion and motion governed by the fractional Langevin equation in confined geometries," *Physical Review E*, vol. 81, no. 2, Article ID 021103, 2010.
- [15] K. Xiangyan, L. I. Daolun, and X. U. Xianzhi, "Study on the mathematical models of coupled thermal-hydrological–mechanical (THM) processes," *Journal of Hydrodynamics*, vol. 4, pp. 34–41, 2005.
- [16] S. G. Brush, H. L. Sahlin, and E. Teller, "Monte carlo study of a one-component plasma. I," *The Journal of Chemical Physics*, vol. 45, no. 6, pp. 2102–2118, 1966.
- [17] D. L. Ermak, "A computer simulation of charged particles in solution. I. Technique and equilibrium properties," *The Journal of Chemical Physics*, vol. 62, no. 10, pp. 4189–4196, 1975.
- [18] P. N. Pusey, "Brownian motion goes ballistic," *Science*, vol. 332, no. 6031, pp. 802–803, 2011.
- [19] A. Einstein, *Investigations on the Theory of Brownian Movement*, Edited by R. Furth, Dover, New York, NY, USA, 1956.
- [20] R. Cherian, C. Gerard, P. Mahadevan, N. T. Cuong, and R. Maezono, "Size dependence of the bulk modulus of semiconductor nanocrystals from first-principles calculations," *Physical Review B*, vol. 82, no. 23, Article ID 235321, 7 pages, 2010.
- [21] J. Pengkang, W. Xiaochang, and G. Kun, "Dla simulation of fractal flocs and calculation of fractal dimension," *Environmental Chemistry*, vol. 1, no. 26, pp. 5–9, 2007.
- [22] F. A. Campo, J. S.R. Murillo, and E. J. Barbero, "Aggregation model for the gelation of a sol starting from the processing conditions," *Journal of Non-Crystalline Solids*, vol. 357, no. 10, pp. 2046–2053, 2011.
- [23] Q. Fu and K. Q. Xia, "Wavelet analysis of multifractal and its application to processing temperature data in Rayleigh-Benard convection," *Journal of Hydrodynamics*, vol. 13, no. 4, pp. 34–41, 2001.

Research Article

Experimental Study on Forecasting Mathematical Model of Drying Shrinkage of Recycled Aggregate Concrete

Yuanchen Guo and Xue Wang

College of Civil Engineering, Chongqing Three Gorges University, 780 ShaLong Road, Wanzhou District, Chongqing 414000, China

Correspondence should be addressed to Yuanchen Guo, gyc1982@yahoo.com.cn

Received 19 November 2011; Accepted 16 January 2012

Academic Editor: Ireneusz Zbicinski

Copyright © 2012 Y. Guo and X. Wang. This is an open access article distributed under the Creative Commons Attribution License, which permits unrestricted use, distribution, and reproduction in any medium, provided the original work is properly cited.

On the basis of basic law in AASHTO2007 model, the forecasting mathematical model of drying shrinkage of recycled aggregate concrete (RAC) is established by regression analysis and experimental study. The research results show that (1) with the replacement rate of RCA increases, the drying shrinkage value of RAC increases; this trend is even more obvious in the early drying time. (2) The addition of fly ash can inhibit the drying shrinkage of RAC, but the effect is not very obvious. Specifically, the addition of fly ash will increase the shrinkage to some extent when the mixing amount is 20%. (3) The addition of expansive agent can obviously inhibit the shrinkage of RAC; the inhibition affection is better than that of fly ash. (4) The forecasting mathematical models of drying shrinkage of RAC established in this paper have high accuracy and rationality according to experiment validation and error analysis.

1. Introduction

Forecasting mathematical models of concrete drying shrinkage is a mathematical equation which represents the relationship of concrete shrinkage and its curing age of [1]. The models are generally fitted by regression analysis of experimental data. The common functional expressions are hyperbolic function, exponential function, and logarithmic function, and so on.

In recent years, many domestic and foreign researchers are committed to the study of forecasting mathematical models and had found a lot of computational model. However, it is very difficult to estimate the shrinkage value and its development in different age because of experimental value of concrete shrinkage having great dispersion [2]. Researchers have introduced a variety of concrete prediction computational model, but these models have some

limitations and application scope. Currently, more typical forecasting mathematical models of drying shrinkage of natural aggregate concrete are shown below.

The main factors considered in forecasting mathematical model proposed by CEB/FIP [3] are relative humidity, water-cement ratio, cement content, dry age, and size of components, the proposed expression is shown in the following:

$$\varepsilon_{sh}(t) = \varepsilon_c \cdot K_b \cdot K_t \cdot K_e, \quad (1.1)$$

where $\varepsilon_{sh}(t)$ is concrete shrinkage strain at any age t , (10^{-6}); ε_c is shrinkage strain relative to humidity (10^{-6}); K_b is correction coefficient of concrete mix proportion affection; K_t is of concrete drying time; K_e is correction coefficient of affection of concrete members.

Main factors what ACI proposed [4] also considered the influence of curing time before drying, curing way, aggregates content, and concrete's air-containing except ones considered by CEB/FIP forecasting mathematical model. ACI's recommended formula is shown in (1.1) and (1.2).

Under wet curing conditions,

$$\varepsilon_{sh}(t) = \left(\frac{t}{35 + t} \right) \varepsilon_u. \quad (1.2)$$

Under steam curing conditions,

$$\varepsilon_{sh}(t) = \left(\frac{t}{55 + t} \right) \varepsilon_u, \quad (1.3)$$

$$\varepsilon_u = 780 \times 10^{-6} \gamma_{sh},$$

where $\varepsilon_{sh}(t)$ is shrinkage strain drying time age t ; ε_u is limit shrinkage strain with the relative humidity 40% which is recommended by ACI; γ_{sh} is product of correction factors of a series of consideration factors, such as wet curing cycle, exposed time, and relative humidity.

This model accords with engineering practice well, for example, last days of before drying, t is considered, but the parameter t is very difficult to estimate.

The forecasting mathematical model proposed by Gardner and Lockman [5] is shown in the following:

$$\varepsilon_{sh}(t, t_c) = \varepsilon_{sh}(t, t_c)_0 f_{sh}(RH) f_{sh}(f_{cu,k}) f_{sh}(M_{cure}) f_{sh}(T_{cement}), \quad (1.4)$$

$$f_{sh}(RH) = 1 - 1.18 RH^4,$$

where $\varepsilon_{sh}(t, t_c)$ is concrete shrinkage from beginning observational age t_c to age t ; $\varepsilon_{sh}(t, t_c)_0$ is shrinkage of concrete under standard conditions; V/S is volume to surface area of concrete component; RH is relative humidity; $f_{sh}(RH)$ is the impact of relative humidity; $f_{sh}(f_{cu,k})$ is the impact of strength grade of concrete; $f_{sh}(M_{cure})$ is the impact coefficient of curing method, taking 1.0 under the standard curing of 1.0; $f_{sh}(T_{cement})$ is influence coefficient of cement type.

In addition to the factors of humidity, component size of concrete, the model also considers the influence of concrete strength grade and cement type on concrete shrinkage.

Based on more recent experimental data, AASHTO [6] puts forward a forecasting mathematical model of concrete shrinkage by means of modifying ACI209 model and CEB/FIP model, the formula as can be seen from the following:

$$\varepsilon_{sh} = k_s k_{hs} k_f k_{td} 0.48 \times 10^{-3}, \quad (1.5)$$

where ε_{sh} is shrinkage strain; k_s is effect coefficient of component size between them:

$$k_s = \left[\frac{t / (26 \exp(0.0142(V/S)) + t)}{t / (t + 45)} \right] \left[\frac{1064 - 3.70(V/S)}{923} \right]. \quad (1.6)$$

V/S is volume to surface area of concrete component; $k_{hs} = (2.00 - 0.014 H)$, is humidity correlation coefficient; H is humidity; $k_f = 35 / (7 + f'_{ci})$ is correlation coefficient of concrete strength; $k_{td} = (t / (61 - 0.58 f'_{ci} + t))$ is correlation coefficient with the development of time t ; f'_{ci} is compressive strength of concrete.

This model accords well with engineering practice, and the parameter selection is simple and convenient. Therefore, the model is used widely since being proposed.

In summary, the considered factors of the existing mathematical models of concrete shrinkage are emphasized particularly, but all of these models have not considered the influence of superplasticizer, fly ash, expansive agent, and other commonly used admixtures in projects on shrinkage and also does not reflect their positive and negative effects on drying shrinkage of concrete. So they cannot accurately predict the shrinkage of concrete mixed with additives. In addition, there is no consideration of influence of aggregate properties on concrete shrinkage.

2. Parameters Considered in the Model and Its Basic Formula

2.1. Parameters Considered in the Model

Besides the environmental humidity, specimen geometry, strength, and other factors, the model mainly considered the influence of replacement rate of recycled concrete aggregate (Hereinafter referred to as RCA) and the mixing amount of fly ash (FA), expansive agent on drying shrinkage of recycled aggregate concrete (hereinafter referred to as RAC) in this paper.

2.2. Determination of the Basic Formula

On the basis of some basic law in AASHTO2007 model, the influence of replacement rate of RCA and the mixing amount of fly ash, expansive agent on drying shrinkage were considered simultaneously in the model of this paper. The forecasting mathematical model of drying shrinkage of RAC is obtained by fitting analysis of test results. The basic formula of the model is shown in the following:

$$\varepsilon'_{sh} = k_s k_{hs} k'_f k_{td} k_r k_k 0.48 \times 10^{-3}, \quad (2.1)$$

Table 1: Mix design of RAC (kg/m³).

Project	Group number	Cement	NCA	RCA	NFA	Water	FDN	Sand ratio	W/C	FA	UEA
RCA test	RC0	426	1000	0	560	200	0	0.36	0.47	0	0
	RC70	426	300	700	560	200	0	0.36	0.47	0	0
	RC100	426	0	1000	560	200	0	0.36	0.47	0	0
FA test	FA0	426	0	1000	560	200	0	0.36	0.47	0	0
	FA10	426	0	1000	560	200	0	0.36	0.47	43	0
	FA20	426	0	1000	560	200	0	0.36	0.47	85	0
	FA30	426	0	1000	560	200	0	0.36	0.47	128	0
UEA test	UEA0	426	0	1000	560	200	0	0.36	0.47	0	0
	UEA8	426	0	1000	560	200	0	0.36	0.47	0	34.1
	UEA12	426	0	1000	560	200	0	0.36	0.47	0	51.1
	UEA15	426	0	1000	560	200	0	0.36	0.47	0	63.9

Table 2: Influence coefficient of strength grade.

Variety of concrete	Strength grade (MPa)	k'_f
RAC	20	0.78
	30	1
	50	1.44

where k_r is impact coefficient of RCA; k_k is impact coefficient of additive; $k_k = k_{fa} \cdot k_e$, k_{fa} is impact coefficient of fly ash; k_e is impact coefficient of expansive agent; the rest of parameters meaning is same to (1.5).

3. Experimental Designs

3.1. Experimental Materials

Cement: P·S 32.5. Construction waste (hereinafter referred to as CW): generating from building demolition in Kunming city, china. UEA-Expansive agent (hereinafter referred to as UEA): the recommended dosage is 8–12%. I grade product fly ash (hereinafter referred to as FA): the fineness is 7.3%.

3.2. Experimental Methods and Mix Proportion

Drying shrinkage test of RAC is made according to GBJ 82–85 “ordinary concrete test method of long-term performance and durability.” In the test, mix design of C30 NAC is used as reference. Specimen size is 100 mm × 100 mm × 515 mm mix proportion is shown in Table 1.

4. Experimental Results and Analysis

4.1. RAC Strength Grade and Its Impact on Drying Shrinkage of RAC

The influence coefficient k'_f [7] (the influence of strength grade on drying shrinkage) is shown in Table 2.

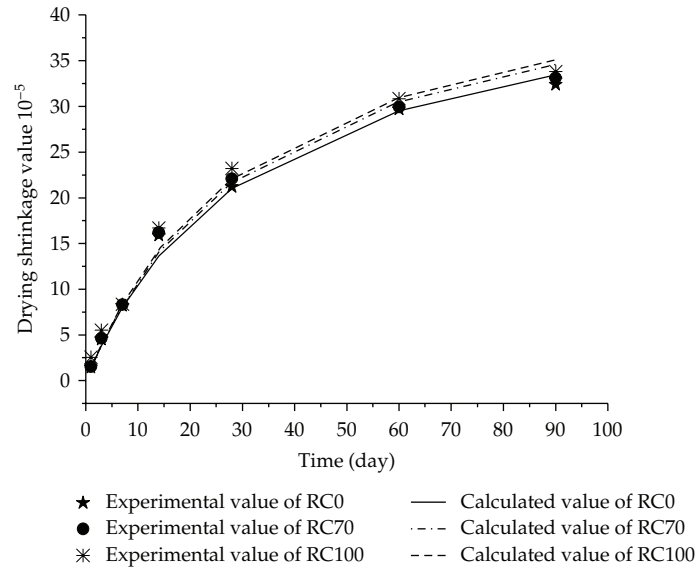


Figure 1: The influence of different RCA replacement rate on RAC drying shrinkage.

4.2. Replacement Rate of RCA and Its Impact on the Drying Shrinkage of RAC

The result of the effects of replacement rate of RCA on drying shrinkage of RAC is shown in Figure 1.

The formula of forecasting mathematical model of concrete drying shrinkage considering the influence of RCA replacement rate is shown in the following:

$$\varepsilon_{shr}(t) = k_r \cdot \varepsilon'_{sh}. \quad (4.1)$$

As can be seen from Figure 1, the concrete shrinkage curve of RAC with different RCA replacement rate is in good agreement with the power function. The influence coefficient of RCA according to power function is shown in (4.2), and the corresponding shrinkage model is shown in (4.3):

$$k_r = \exp(a \cdot v_r + b), \quad (4.2)$$

$$\varepsilon_{shr} = \exp(a \cdot v_r + b) \cdot \varepsilon'_{sh}, \quad (4.3)$$

where v_r is replacement rate of RCA; a , b are constant which are derived from experimental data fitting.

Table 3: Table of fitting parameters of mathematical model.

Mathematical model	Regression coefficients		Fitting equation	Correlation coefficients	Mean square deviation	F statistics
	<i>a</i>	<i>b</i>				
Equation (4.3)	0.046	-0.003	Equation (4.5)	0.99459	1.56085	2565
Equation (4.8)	-3.88	1.18	Equation (4.10)	0.99324	3.15600	1390
Equation (4.13)	-1.85	-0.026	Equation (4.15)	0.99253	1.45512	1720

The function expression derived from regression fitting using Levenberg-Marquardt method + general global optimization method is shown in (4.4), (4.5), and the fitting parameters are shown in Table 3:

$$k_r = \exp(0.046v_r - 0.003), \quad (4.4)$$

$$\varepsilon_{shr} = \exp(0.046v_r - 0.003) \cdot \varepsilon'_{sh}. \quad (4.5)$$

When replacement rates of RCA are 0%, 70%, 100%, the concrete shrinkage values measured in the experimental at 3d age are 4.51×10^{-5} , 4.6×10^{-5} , 5.51×10^{-5} , which is that the shrinkage strain of RAC with 70% RCA is 1.02 times of the natural coarse aggregate concretes (NACs) at 3 d age; the shrinkage strain of RAC with 100% recycled coarse aggregate is 1.2217 times of NACs at 3 d age. The concrete shrinkage values measured in the experimental at 28 d age are 21.2×10^{-5} , 22.1×10^{-5} , 23.2×10^{-5} , which is that the shrinkage strain of RAC with 70% recycled coarse aggregate is 1.02 times of the natural coarse aggregate concretes (NACs) at 3 d age; the shrinkage strain of RAC with 70% recycled coarse aggregate is 1.02 times of NACs at 28 d age, the shrinkage strain of RAC with 100% recycled coarse aggregate is 1.094 times of NACs at 28 d age; the concrete shrinkage values measured in the experimental at 60 d age are 29.7×10^{-5} , 29.9×10^{-5} , 30.85×10^{-5} , which is that the shrinkage strain of RAC with 70% recycled coarse aggregate is 1.007 times of the natural coarse aggregate concretes (NACs) at 60 d age; the shrinkage strain of RAC with 100% recycled coarse aggregate is 1.009 times of NACs at 60 d age; the concrete shrinkage values measured in the experimental at 90 d age are 32.4×10^{-5} , 33.1×10^{-5} , 33.8×10^{-5} , which is that the shrinkage strain of RAC with 70% recycled coarse aggregate is 1.02 times of the natural coarse aggregate concretes (NACs) at 90 d age, the shrinkage strain of RAC with 100% recycled coarse aggregate is 1.043 times of NACs at 90 d age. It can clearly be seen that with the dosage of RCA increases, the shrinkage values of RAC were gradually increasing, which is similar to the research results of Gómez-Soberón [8], Poon and Kou [9], Khatib [10]. This paper also found that the shrinkage values' increasing trend of RAC with 100% RCA is more obvious; the increasing trend of RAC shrinkage values in early age larger than late stages, but with the drying time increase, this trend gradually becomes flat.

We can see that the increase effect of drying shrinkage caused by RCA is larger in the early time than late stage's; the shrinkage strain of RAC with 100% RCA is larger significantly than NAC's, This may be because RCA itself has larger shrinkage deformation and lower elastic modulus [11].

In regression (4.4), when v_r is from 0 to 0.7, 1, k_r is from 0.9974 to 1.031, 1.045, it is 1.033 and 1.048 times of the original, which tallies with the experimental results. As can be seen from Table 3, the model correlation coefficients are over 0.99, which explains that the forecasting mathematical model (4.5) in this paper is with high accuracy.

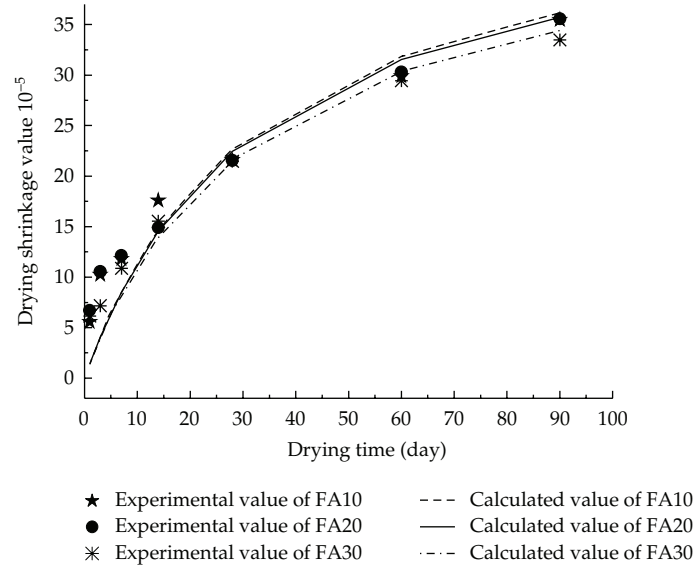


Figure 2: Drying shrinkage value of different content of fly ash RAC at various drying time.

4.3. Mixing Amount of Fly Ash and Its Impact on the Drying Shrinkage of RAC

The result of the effects of the mixing amount of fly ash on drying shrinkage of RAC is shown in Figure 2.

The formula of forecasting mathematical model of concrete drying shrinkage considering the influence of the mixing amount of fly ash is shown in the following:

$$\varepsilon_{sh\,fa}(t) = 1.044 \cdot k_{fa} \cdot \varepsilon'_{sh} \quad (4.6)$$

where “1.044” is the impact coefficient of RCA when the replacement rate of RCA is 100%.

As can be seen from Figure 2, the concrete shrinkage curve of RAC with different mixing amount of fly ash is in good agreement with the composite exponential function. The influence coefficient of fly ash according to composite exponential function is shown in (4.7), and the corresponding shrinkage model is shown in the following:

$$k_{fa} = 1 - \exp\left(a \cdot (1 - v_{fa})^b\right), \quad (4.7)$$

$$\varepsilon_{sh\,fa}(t) = 1.044 \cdot k_{fa} \cdot \varepsilon'_{sh} \quad (4.8)$$

where v_{fa} is the mixing amount of fly ash; a , b are constant which derived from experimental data fitting.

The function expression derived from regression fitting using Levenberg-Marquardt method + general global optimization method is shown in (4.9), (4.10), and the fitting parameters are shown in Table 3:

$$k_{fa} = 1 - \exp\left(-3.38(1 - v_{fa})^{1.18}\right), \quad (4.9)$$

$$\varepsilon_{sh\,fa}(t) = 1.044 \cdot \left(1 - \exp\left(-3.38 \cdot (1 - v_{fa})^{1.18}\right)\right) \cdot \varepsilon'_{sh}. \quad (4.10)$$

As can be seen from Figure 2, when the mixing amount of fly ash is 10%, 20%, 30%, the concrete shrinkage values measured in the experimental at 3 d age are 10.26×10^{-5} , 10.55×10^{-5} , 7.17×10^{-5} , which is that the shrinkage strain of RAC with 20% fly ash is 1.208 times of the RACs with 10% fly ash at 3d age; the shrinkage strain of RAC with 30% fly ash is 0.6988 times of RACs with 10% fly ash at 3d age. The concrete shrinkage values measured in the experimental at 28 d age are 21.6×10^{-5} , 21.55×10^{-5} , 21.46×10^{-5} , which is that the shrinkage strain of RAC with 20% fly ash is 0.9977 times of the RACs with 10% fly ash at 28 d age; the shrinkage strain of RAC with 30% fly ash is 0.9935 times of the RACs with 10% fly ash at 28 d age. the concrete shrinkage values measured in the experimental at 60 d age are 29.91×10^{-5} , 30.31×10^{-5} , 29.44×10^{-5} , which is that the shrinkage strain of RAC with 20% fly ash is 1.013 times of the RACs with 10% fly ash at 60 d age; the shrinkage strain of RAC with 30% fly ash is 0.9843 times of RACs with 10% fly ash at 60 d age. The concrete shrinkage values measured in the experimental at 90 d age are 35.46×10^{-5} , 35.45×10^{-5} , 33.47×10^{-5} , which is that the shrinkage strain of RAC with 20% fly ash is 0.9997 times of the RACs with 10% fly ash at 90 d age; the shrinkage strain of RAC with 30% fly ash is 0.9439 times of the RACs with 10% fly ash at 90 d age.

The results show that the addition of fly ash will slightly increase the shrinkage of RAC in early drying time, but, generally, the addition of fly ash can inhibit the drying shrinkage of RAC; however, this effect is not very obvious. The study found that the addition of fly ash will increase the shrinkage to some extent when the mixing amount is 20%, the phenomenon is more apparent in the early time, whose conclusion is slightly different from the research result of Mandal and Gupta [12]. This maybe because the total porosity of RAC with 20% fly ash slightly higher than that with 10%, 30% fly ashes.

In regression (4.9), when v_{fa} is from 0.1 to 0.2, 0.3, k_{fa} is from 0.9675 to 0.9493, 0.9217, it is 0.9812 and 0.9527 times of the original, which tallies with the experimental results. As can be seen from Table 3, the model correlation coefficients are over 0.99, which explains that the forecasting mathematical model (4.10) in this paper is with high accuracy.

4.4. Mixing Amount of Expansive Agent and Its Impact on the Drying Shrinkage of RAC

The result of the effects of the mixing amount of expansive agent on drying shrinkage of RAC is shown in Figure 3.

The formula of forecasting mathematical model of concrete drying shrinkage considering the influence of the mixing amount of expansive agent is shown in the following:

$$\varepsilon_{sh\,e}(t) = 1.044 \cdot k_e \cdot \varepsilon'_{sh}. \quad (4.11)$$

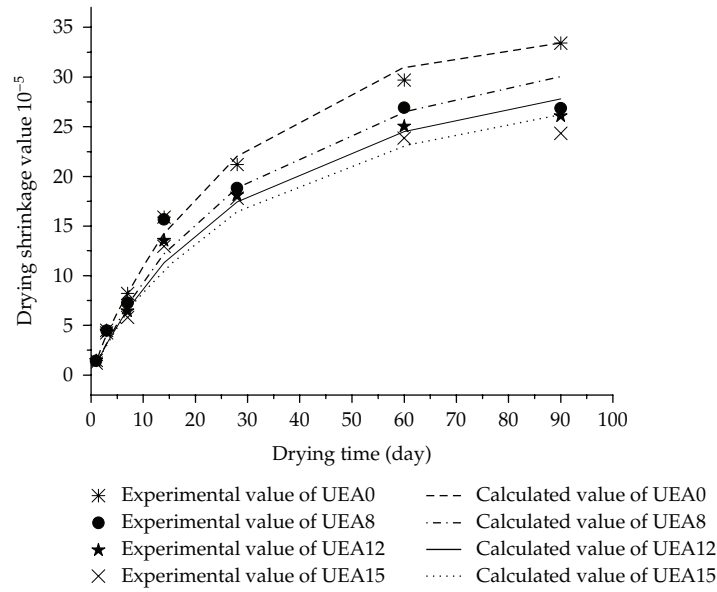


Figure 3: Drying shrinkage value of different content of expansion agent RC at various drying time.

As can be seen from Figure 3, the concrete shrinkage curve of RAC with different mixing amount of expansive agent is in good agreement with the power function. The influence coefficient of fly ash according to power function is shown in (4.12), and the corresponding shrinkage model is shown in (4.13):

$$k_e = \exp(a \cdot v_e + b), \quad (4.12)$$

$$\varepsilon_{sh_e}(t) = 1.044 \cdot k_e \cdot \varepsilon'_{sh}. \quad (4.13)$$

The function expression derived from regression fitting using Levenberg-Marquardt method + general global optimization method is shown in (4.14), (4.15), and the fitting parameters are shown in Table 3:

$$k_e = \exp(-1.85v_e - 0.026), \quad (4.14)$$

$$\varepsilon_{sh_e}(t) = 1.044 \cdot \exp(-1.85v_e - 0.026) \cdot \varepsilon'_{sh}. \quad (4.15)$$

As can be seen from Figure 3, when the mixing amount of expansive agent are 0%, 8%, 12%, and 15%, the concrete shrinkage values measured in the experimental at 3 d age are 4.51×10^{-5} , 4.47×10^{-5} , 4.42×10^{-5} , 4.24×10^{-5} , which is that the shrinkage strain of RAC with 8% expansive agent is 0.9911 times of the RACs with 0% expansive agent at 3 d age; the shrinkage strain of RAC with 12% expansive agent is 0.9800 times of the RACs with 0% expansive agent at 3 d age; the shrinkage strain of RAC with 15% expansive agent is 0.9401 times of the RACs with 0% expansive agent at 3 d age. The concrete shrinkage values measured in the experimental at 28 d age are 21.2×10^{-5} , 18.81×10^{-5} , 18.12×10^{-5} , 17.81×10^{-5} , which is that the shrinkage strain of RAC with 8% expansive agent is 0.8873 times of the RACs with 0%

expansive agent at 28 d age; the shrinkage strain of RAC with 12% expansive agent is 0.8547 times of the RACs with 0% expansive agent at 28 d age; the shrinkage strain of RAC with 15% expansive agent is 0.8401 times of the RACs with 0% expansive agent at 28 d age. The concrete shrinkage values measured in the experimental at 60 d age are 29.7×10^{-5} , 26.92×10^{-5} , 25.03×10^{-5} , 23.84×10^{-5} , which is that the shrinkage strain of RAC with 8% expansive agent is 0.9064 times of the RACs with 0% expansive agent at 60 d age; the shrinkage strain of RAC with 12% expansive agent is 0.8519 times of the RACs with 0% expansive agent at 60 d age; the shrinkage strain of RAC with 15% expansive agent is 0.8027 times of the RACs with 0% expansive agent at 60 d age. The concrete shrinkage values measured in the experimental at 90 d age are 32.4×10^{-5} , 26.85×10^{-5} , 26.08×10^{-5} , 24.32×10^{-5} , which is that the shrinkage strain of RAC with 8% expansive agent is 0.8287 times of the RACs with 0% expansive agent at 90 d age; The shrinkage strain of RAC with 12% expansive agent is 0.8049 times of the RACs with 0% expansive agent at 90 d age; the shrinkage strain of RAC with 15% expansive agent is 0.7506 times of the RACs with 0% expansive agent at 90 d age.

It can clearly be seen that the addition of expansive agent can obviously inhibit the shrinkage of RAC and the inhibition affection is better than that of fly ash, which is similar to the research result of Bissonnette et al. [13].

In regression (4.14), when v_e is from 0 to 0.08, 0.12, 0.15, k_e is from 0.9743 to 0.7804, 0.7382, it is 0.8624, 0.8009, and 0.7577 times of the original, which tallies with the experimental results. As can be seen from Table 3, the model correlation coefficients are over 0.99, which explains that the forecasting mathematical model (4.15) in this paper is with high accuracy.

4.5. Ambient Humidity, Specimen Size, and Its Impact on the Drying Shrinkage of RAC

According to AASHTO2007 model (1.5), $k_{hs} = (2.00 - 0.014 H)$, when relative humidity is from 60% to 100%, k_{hs} value changes from 1.16 to 0.6, which decreases by 48.3%. The result show that the change of humidity having have a great impact on drying shrinkage of concrete materials.

In general, the effect of specimen size on concrete shrinkage is mainly embodied in the spread speed of internal moisture to the outside and the impact mechanism on shrinkage has the similar law to that of relative humidity [13]. The size of shrinkage test mode in this paper is $100 \text{ mm} \times 100 \text{ mm} \times 515 \text{ mm}$, then $V/S = 22.79$. The effect coefficient of specimen size is directly calculated from AASHTO2007 model (1.6).

4.6. Forecasting Mathematical Models of Concrete Drying Shrinkage of RAC

With (2.1) as basic formula, in the comprehensive study in Sections 4.1, 4.2, 4.3, 4.4, and 4.5 in this paper, the forecasting mathematical models of drying shrinkage of RAC are shown in the following:

$$\begin{aligned} \varepsilon'_{sh} = & 0.00048 k_s \cdot k_{hs} \cdot k_{td} \cdot k'_f \exp(0.046v_r - 0.003) \cdot \left(1 - \exp\left(-3.38(1 - v_{fa})^{1.18}\right)\right) \\ & \cdot \exp(-1.85v_e - 0.026), \end{aligned} \quad (4.16)$$

where ε'_{sh} is shrinkage strain, 10^{-5} ; k_s is effect coefficient of component size (as can be seen from (1.6)); $k_{hs} = (2.00 - 0.014 H)$ is humidity correlation coefficient; H is humidity; k'_f is

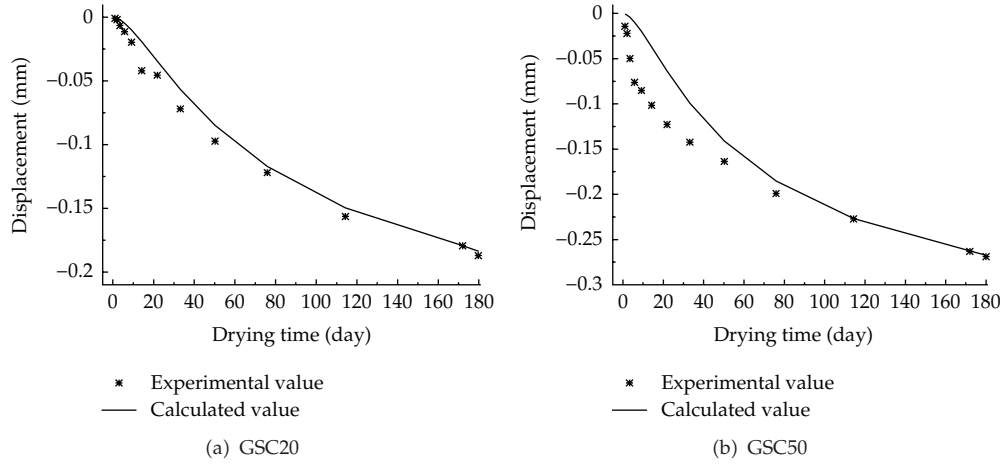


Figure 4: Calculated value of displacement of RAC contrasted with experimental value.

Table 4: Table of mix design in verification test.

Project	Strength grade	Cement (kg/m ³)	RCA (kg/m ³)	Sand (kg/m ³)	Water (kg/m ³)	Sand ratio (kg/m ³)	W/C	FDN (kg/m ³)	UEA (kg/m ³)	FA (kg/m ³)
GSC20	C20	299	970	700	200	0.42	0.67	1.50	/	/
GSC50	C50	476	950	510	200	0.35	0.36	2.38	27.8	80

correlation coefficient of concrete strength grade (as can be seen from Table 2); $k_{td} = (t / (61 - 0.58f'_{ci} + t))$ is correlation coefficient with the development of time t ; f'_{ci} is compressive strength of concrete at 28 d age; v_r is replacement rate of RCA; v_{fa} is the mixing amount of fly ash; v_e is the mixing amount of expansive agent. The rest of parameters' meaning is same to those in (1.5).

5. Error Analysis and Model Validation

In order to verify the accuracy of the model, GSC20 and GSC50 (the strength grade is, resp., C20, and C50), two different groups shrinkage specimen are devised and prepared in this paper. The mix design of verification experiment is shown in Table 4.

One point located on the top surface of the specimen selected as object, transforming the shrinkage values of the point into displacement, the comparison chart of calculated and experimental values of GSC20, GSC50, is shown in Figures 4(a) and 4(b)

Absolute error and relative error are selected as indexes to do error analysis of displacement calculated values of RAC; the formula is shown in the following:

$$e_a = x_c - x_e, \quad (5.1)$$

$$e_r = \frac{e_a}{x_e} \times 100\%, \quad (5.2)$$

where e_a is absolute error value; x_e is experimental value of displacement, mm; x_c is calculated value of displacement, mm; e_r is relative error value, 100%.

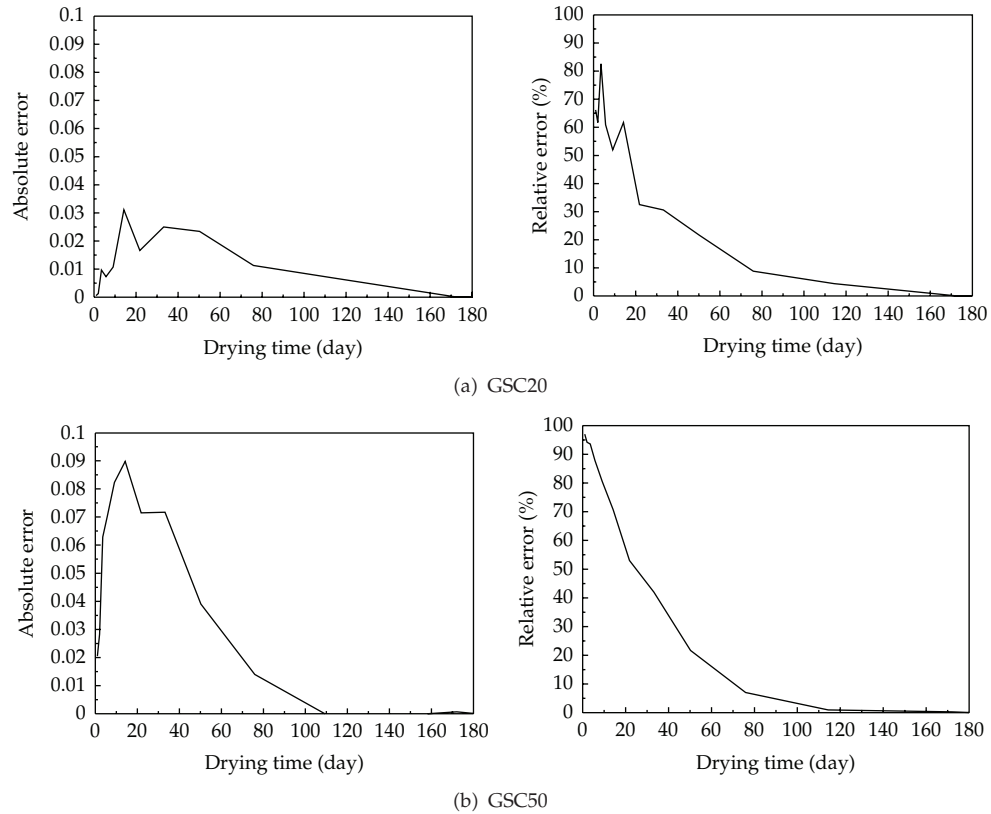


Figure 5: Error analysis chart of displacement calculated value and experimental value of RAC.

The absolute error values and relative error values are calculated according to (5.1) and (5.2). The error distribution curve drew by Matlab is shown in Figure 5.

Figures 5(a) and 5(b) is error chart (including absolute error and relative error) of concrete of GSC20 and GSC50. As can be seen from Figures 5(a) and 5(b), the absolute error values between calculated shrinkage value (calculated by the model built in this paper) and experimental value have small fluctuation in 180-day drying time. Especially after 60 d drying time, the absolute error values gradually approach zero, which indicates that the model built in this paper has high accuracy after 60 d drying time. The absolute error values have large fluctuation in the drying time of 0 ~ 28 d, the maximum absolute error value arises in the drying time of 14 d, absolute error value is about 0.035. The relative error values between calculated shrinkage value and experimental value have the similar law to the absolute error ones in 180-day drying time. The relative error values have large fluctuation in the early drying time, the relative maximum error value is even up to 95%, but, with the drying time increase, the relative error values are becoming smaller and smaller. Especially after 60 d drying time, the error values gradually approach zero.

So, as can be seen from Figures 4 and 5, the drying shrinkage values calculated in the use of the model of this paper are slightly smaller than those of experimental values, but, with the drying time increase, the calculated values have higher coincide degree with the experimental results. Calculated values and experimental values of RAC shrinkage are almost

the same in 60 d age especially, which also shows that the forecasting mathematical models of drying shrinkage of RAC builded in this paper have high accuracy and rationality.

6. Conclusion

(1) Under the same experimental condition, the drying shrinkage values of RAC are higher than those of NAC because of the reduce of RAC inhibition effect and old cement mortar's further shrinkage after water absorption, and this trend is even more obvious in the early drying time. With the replacement rate of RCA increases, the drying shrinkage value of RAC increases too.

(2) The addition of fly ash can inhibit the drying shrinkage of RAC, but the effect is not very obvious. Specifically, the addition of fly ash will increase the shrinkage to some extent when the mixing amount is 20%, the phenomenon is more apparent in the early time. This is because the total porosity of RAC with 20% fly ash is slightly higher than that with 10%, 30% fly ashes.

(3) The addition of expansive agent can obviously inhibit the shrinkage of RAC, the inhibition affection is better than that of fly ash.

(4) Through regression analysis of large number of experimental data, the forecasting mathematical models of drying shrinkage of RAC shown as follow:

$$\begin{aligned} \varepsilon'_{sh} = & 0.048 \times 10^{-3} \times k_s \cdot k_{hs} \cdot k_{td} \cdot k'_f \exp(0.046v_r - 0.003) \cdot \left(1 - \exp\left(-3.38(1 - v_{fa})^{1.18}\right)\right) \\ & \cdot \exp(-1.85v_e - 0.026). \end{aligned} \quad (6.1)$$

(5) The forecasting mathematical models of drying shrinkage of RAC built in this paper have high accuracy and rationality according to experiment validation and error analysis.

Acknowledgments

This project was supported by the Project of Science and Technology Committee of Wanzhou District of China (WZ011R003), Key Projects of Chongqing Three Gorges University (11ZD-14), Talents Project of Chongqing Three Gorges University (11RC-16), and Ph.D. Funded Projects of Chongqing Three Gorges University (11ZZ-62).

References

- [1] Z. Lv and Z. Yingchen, *Shrinkage and Creep*, China Railway Publishing House China Railway Publishing House, Beijing, China, 1994.
- [2] D. W. Mokarem, R. E. Weyers, and D. S. Lane, "Development of a shrinkage performance specifications and prediction model analysis for supplemental cementitious material concrete mixtures," *Cement and Concrete Research*, vol. 35, no. 5, pp. 918–925, 2005.
- [3] O. Chaalla, B. Benmokrane, and G. Ballivy, "Drying shrinkage strains: experimental versus codes," *ACI Materials Journal*, vol. 89, no. 3, pp. 263–266, 1992.
- [4] ACI209 R-82, "Prediction of creep, shrinkage and temperature effects in Concrete Structures".
- [5] N. J. Gardner and M. J. Lockman, "Design provisions for drying shrinkage and creep of normal-strength concrete," *ACI Materials Journal*, vol. 98, no. 2, pp. 159–167, 2001.

- [6] "AASHTO LRFD bridge design specifications section 5: concrete structures," in *Proceedings of the American Association of State Highway and Transportation Officials (AASHTO '07)*, Washington, DC, USA, 2007.
- [7] G. Yuanchen, *Drying Shrinkage Properties of Recycled Aggregate/Cement Composite*, Kunming University of Science and Technology, Kunming, China, 2010.
- [8] J. M. V. Gómez-Soberón, "Porosity of recycled concrete with substitution of recycled concrete aggregate: an experimental study," *Cement and Concrete Research*, vol. 32, no. 8, pp. 1301–1311, 2002.
- [9] C. S. Poon and S. C. Kou, "Properties of steam cured recycled aggregate concrete," in *Proceedings of the International Conference on Sustainable Waste Management and Recycling*, pp. 1–12, September 2004.
- [10] J. M. Khatib, "Properties of concrete incorporating fine recycled aggregate," *Cement and Concrete Research*, vol. 35, no. 4, pp. 763–769, 2005.
- [11] K. Eguchi, K. Teranishi, and M. Narikawa, "Study on mechanism of drying shrinkage and water loss of recycled aggregate concrete," *Journal of Structure and Construction Engineering*, vol. 3, pp. 1–7, 2003.
- [12] S. Mandal and A. Gupta, "Strength and durability of recycled aggregate concrete," in *Towards a Better Built Environment Innovation, Sustainability, Information Technology*, E. Zurich, Ed., Zurich, Switzerland, 2002.
- [13] B. Bissonnette, P. Pierre, and M. Pigeon, "Influence of key parameters on drying shrinkage of cementitious materials," *Cement and Concrete Research*, vol. 29, no. 10, pp. 1655–1662, 1999.